Supervisors: Ward van der Stam
and Dr. Celso de Mello Donegá

# Size, shape, composition and assembly control over colloidal copper chalcogenide nanocrystals

Masterthesis;
Quinten Akkerman
April 8, 2014

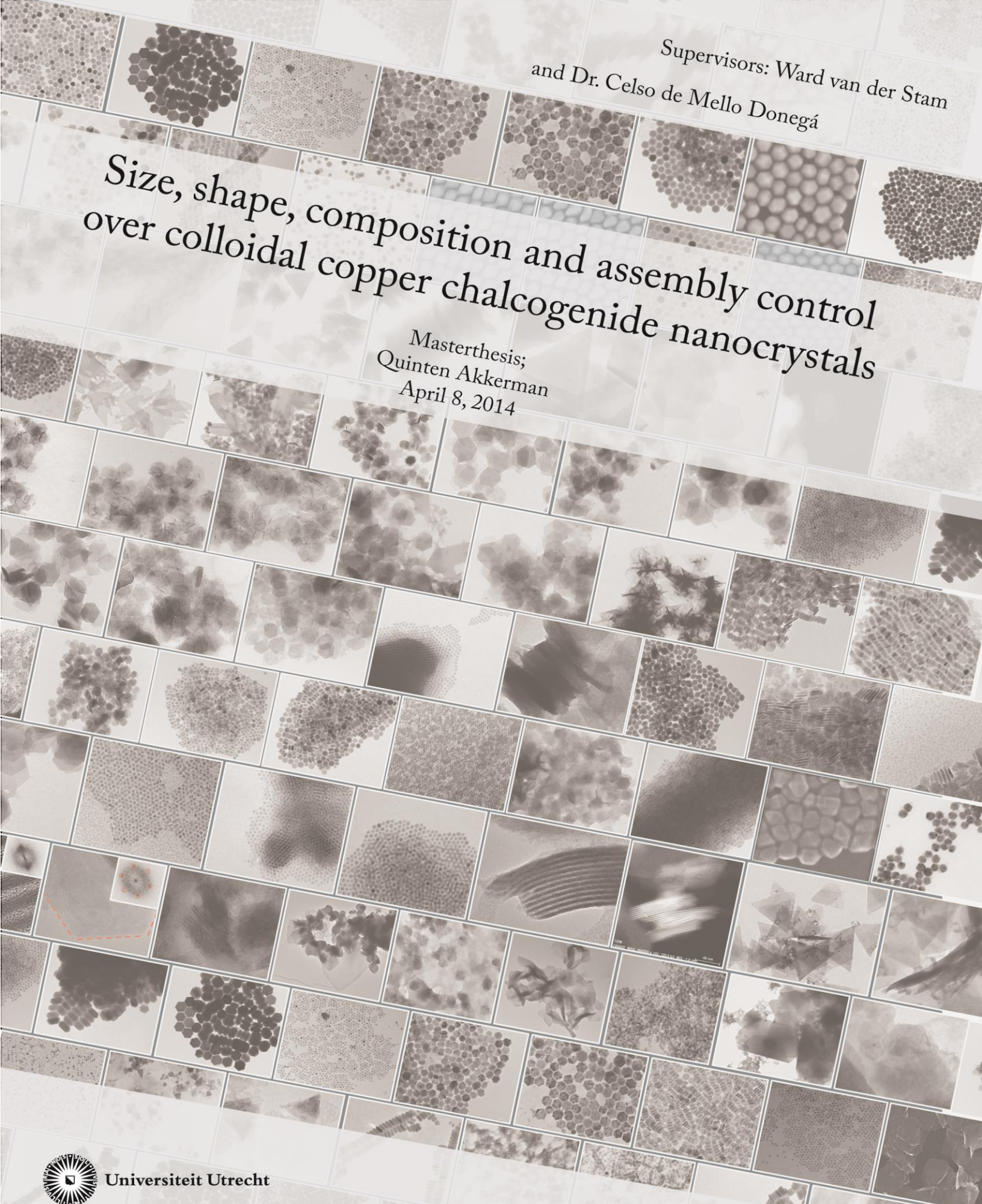

Universiteit Utrecht

Condensed Matter And Interfaces, Debye Institute for Nanomaterials Science, Utrecht

# Abstract

In this masterthesis, a multidisciplinary research on the size, shape and composition of copper chalcogenide nanocrystals (NCs) is presented. This has resulted in several different synthesis strategies including ultrathin $Cu_{1.8}S$ nanosheets, large quasi-spherical $Cu_{1.8}S$ NCs, $Cu_{2-x}Se$ nanoplatelets and self-assembled superlattices of ZnS NCs, which were obtained after cation exchange (CE) reactions on hexagonal bifrustum and bipyramidal $Cu_{1.96}S$ NCs.

It was shown that ultrathin digenite $Cu_{1.8}S$ nanosheets could be synthesized with a well-defined thickness of 2.0 nm and a high control over the size and shape in the lateral dimensions ranging from 110 nm up to several µm and both hexagonal and triangular shaped. The formation mechanism behind this synthesis was further investigation and it has been shown that these nanosheets were synthesized via halide stabilized lamellar copper-thiolate complexes. Further size and shape control over $Cu_{2-x}S$ NCs was shown with the synthesis hexagonal bifrustum and bipyramidal djurleite $Cu_{1.96}S$ NCs and large quasi-spherical $Cu_{2-x}S$ NCs. Size and shape control over $Cu_{2-x}Se$ was obtained with a novel selenium precursor (1-dodecaneselenol, DDSe), which was synthesized with a Grignard reaction. The DDSe precursor was used to synthesis $Cu_{2-x}Se$ platelets, were the precursors were comparable with the halide stabilized lamellar copper-thiolate complexes for the $Cu_{1.8}S$ nanosheets. Finally, the composition control of the $Cu_{2-x}S$ and $Cu_{2-x}Se$ NCs was obtained with the use of CE. This yielded CdS, PbS, ZnS nanosheets, CdSe nanoplatelets and hexagonal bifrustum and bipyramidal ZnS NCs as is shown in the overview below.

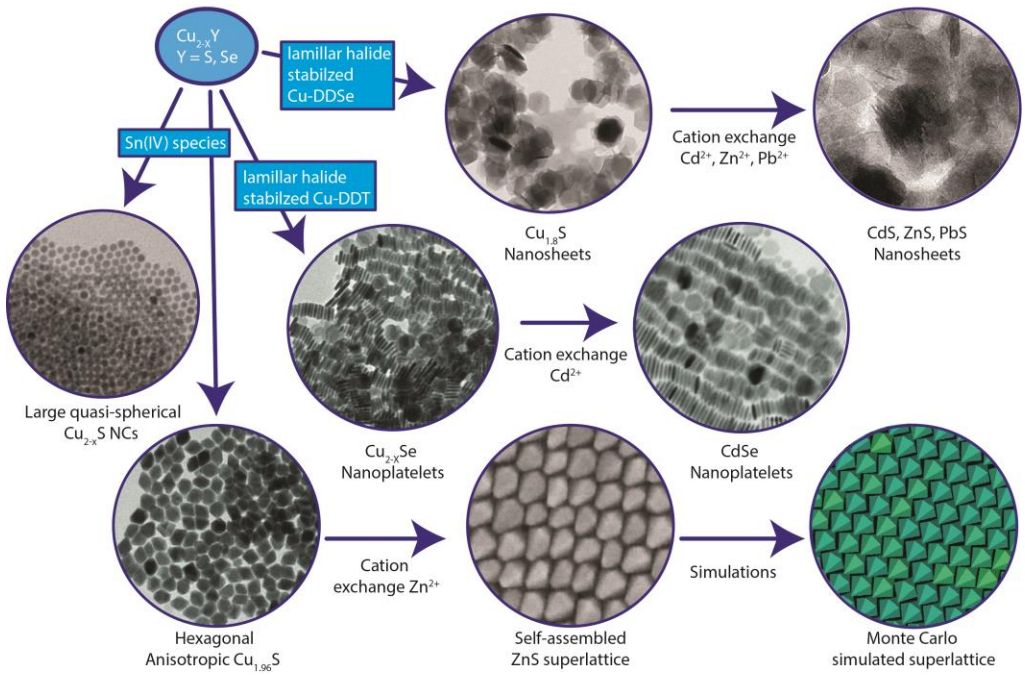


**Overview of the work this thesis will describe.**

# Table of Contents

# 1. General introduction

The use of colloidal semiconductor nanocrystals (NCs) for applications like light emitting diodes (LEDs) and solar cells has been very well studied over the past few decades.[1–4] Sony, for instance, recently announced the use of quantum dots (QDs), spherical nanometer sized semiconducting NCs, in flat-screen televisions.[5] This rapid increase in interest for semiconductor NCs comes from the properties of the NCs being size and shape dependent.[6] In other words, the properties of the nanocrystals can be tuned by merely changing the size and shape, and thus without changing the composition.

The work-horses in the field of NCs are CdX and PbX (X= S, Se, Te) semiconductor NCs and have been thoroughly investigated in the past decades due to their interesting optical properties.[6–8] These Cd, Pb and also Te containing NCs are toxic and moreover expensive due to the use of heavy elements. Therefore, extensive research is being conducted with the aim of finding nontoxic and cheaper alternatives like $CuInY_2$ and $Cu_2ZnSnY_4$ (Y = S, Se).[3,9–11] These novel colloidal NCs have shown interesting optoelectronic properties but their synthesis methods do no yet offer the same level of control over the size and shape of the NCs as has been archived on CdX and PbX NCs. Although copper(I) sulfide and copper(I) selenide ($Cu_{2-x}Y$, Y=S, Se) are less interesting in terms of optical properties compared to $CuInY_2$ and $Cu_2ZnSnY_4$ (Y = S, Se), they can be synthesized with a high control over the size and shape.[12–14] Moreover, $Cu_{2-x}Y$ can be converted into a wide range of other metal sulfides by exchanging the $Cu^+$ ions for other metal ions.[15–18] This makes $Cu_{2-x}Y$, in combination with the high control over the size and shape, an interesting and low-cost material for metal chalcogenide NCs, and thus a suitable candidate for the synthesis of cheap and nontoxic nanomaterials.

In this work, different shaped $Cu_{2-x}Y$ NCs, including ultrathin nanosheets, anisotropic hexagonal based NCs and CdSe platelets have been synthesized and investigated to obtain control over the size, shape, composition and self-assembly behavior. This work is organized as follows. The second chapter will cover the necessary theoretical background to understand this thesis. Chapters 3 will focus on the synthesis of ultrathin $Cu_{1.8}S$ nanosheets. The following chapter, chapter 4, will present different methods for synthesizing large (~10-40 nm) $Cu_{2-x}S$ NCs. The synthesis of a novel Se precursor, 1-dodecaneselenol, together with its use in the synthesis of $Cu_{2-x}Se$ platelets, will be presented in chapter 5. Chapter 6 will cover the self-assembly of anisotropic ZnS NCs, which were synthesized by CE on the $Cu_{1.96}S$ NCs.

## References


1. Q. Guo; H. W. Hillhouse; R. Agrawal. Synthesis of Cu2ZnSnS4 Nanocrystal Ink and Its Use for Solar Cells. *J. Am. Chem. Soc.* **2009**, *131*, 11672–11673.

2. M. V. Kovalenko; M. I. Bodnarchuk; J. Zaumseil; J.-S. Lee; D. V. Talapin. Expanding the Chemical Versatility of Colloidal Nanocrystals Capped with Molecular Metal Chalcogenide Ligands. *J. Am. Chem. Soc.* **2010**, *132*, 10085–10092.

3. C. Steinhagen; M. G. Panthani; V. Akhavan; B. Goodfellow; B. Koo; B. a Korgel. Synthesis of Cu2ZnSnS4 Nanocrystals for Use in Low-Cost Photovoltaics. *J. Am. Chem. Soc.* **2009**, *131*, 12554–12555.

4. J. M. Pietryga; D. J. Werder; D. J. Williams; J. L. Casson; R. D. Schaller; V. I. Klimov; J. A. Hollingsworth. Utilizing the Lability of Lead Selenide to Produce Heterostructured Nanocrystals with Bright, Stable Infrared Emission. *J. Am. Chem. Soc.* **2008**, *130*, 4879–4885.

5. K. Bourzac. Quantum Dots Go on Display. *Nature* **2013**, *493*, 283.

6. C. B. Murray: D. J. Norris. Synthesis and Characterization of Nearly Monodisperse CdE (E = S, Se, Te) Semiconductor Nanocrystallites. *J. Am. Chem. Soc.* **1993**, *115*, 8706–8715.

7. Y. Wang; A. Tang; K. Li; C. Yang; M. Wang; H. Ye; Y. Hou; F. Teng. Shape-Controlled Synthesis of PbS Nanocrystals via a Simple One-Step Process. *Langmuir* **2012**, *28*, 16436–16443.

8. A. Efros; M. Rosen; M. Kuno; M. Nirmal; D. Norris; M. Bawendi. Band-Edge Exciton in Quantum Dots of Semiconductors with a Degenerate Valence Band: Dark and Bright Exciton States. *Phys. Rev. B. Condens. Matter* **1996**, *54*, 4843–4856.

9. W. Han; L. Yi; N. Zhao; A. Tang; M. Gao; Z. Tang. Synthesis and Shape-Tailoring of Copper Sulfide/indium Sulfide-Based Nanocrystals. *J. Am. Chem. Soc.* **2008**, *130*, 13152–13161.

10. Y. Zhao; Y. Zhang; H. Zhu; G. C. Hadjipanayis; J. Q. Xiao. Low-Temperature Synthesis of Hexagonal (Wurtzite) ZnS Nanocrystals. *J. Am. Chem. Soc.* **2004**, *126*, 6874–6875.

11. S. W. Shin; J. H. Han; C. Y. Park; S.-R. Kim; Y. C. Park; G. L. Agawane; a. V. Moholkar; J. H. Yun; C. H. Jeong; J. Y. Lee; J. H. Kim. A Facile and Low Cost Synthesis of Earth Abundant Element Cu2ZnSnS4 (CZTS) Nanocrystals: Effect of Cu Concentrations. *J. Alloys Compd.* **2012**, *541*, 192–197.

12. Y.-B. Chen; L. Chen; L.-M. Wu. The Structure-Controlling Solventless Synthesis and Optical Properties of Uniform Cu2S Nanodisks. *Chemistry* **2008**, *14*, 11069–11075.

13. Y. Wang; Y. Hu; Q. Zhang; J. Ge; Z. Lu; Y. Hou; Y. Yin. One-Pot Synthesis and Optical Property of copper(I) Sulfide Nanodisks. *Inorg. Chem.* **2010**, *49*, 6601–6608.

14. W. Li; A. Shavel; R. Guzman; J. Rubio-Garcia; C. Flox; J. Fan; D. Cadavid; M. Ibáñez; J. Arbiol; J. R. Morante; A. Cabot. Morphology Evolution of Cu(2-x)S Nanoparticles: From Spheres to Dodecahedrons. *Chem. Commun. (Camb).* **2011**, *47*, 10332–10334.

15. J. B. Rivest; P. K. Jain. Cation Exchange on the Nanoscale: An Emerging Technique for New Material Synthesis, Device Fabrication, and Chemical Sensing. *Chem. Soc. Rev.* **2013**, *42*, 89–96.

16. H. Li; M. Zanella; A. Genovese; M. Povia; A. Falqui; C. Giannini; L. Manna. Sequential Cation Exchange in Nanocrystals: Preservation of Crystal Phase and Formation of Metastable Phases. *Nano Lett.* **2011**, *11*, 4964–4970.

17. J. M. Luther; H. Zheng; B. Sadtler; a P. Alivisatos. Synthesis of PbS Nanorods and Other Ionic Nanocrystals of Complex Morphology by Sequential Cation Exchange Reactions. *J. Am. Chem. Soc.* **2009**, *131*, 16851–16857.

18. B. Sadtler; D. O. Demchenko; H. Zheng; S. M. Hughes; M. G. Merkle; U. Dahmen; L.-W. Wang; a P. Alivisatos. Selective Facet Reactivity during Cation Exchange in Cadmium Sulfide Nanorods. *J. Am. Chem. Soc.* **2009**, *131*, 5285–5293.

# 2. Theoretical background

This chapter is devoted to the basic theory behind semiconducting nanocrystals (NCs), their synthesis and their properties. This chapter is organized as follows. The first section, section 2.1, gives a brief introduction into bulk semiconductors, nanocrystals and quantum confinement. Section 2.2 describes the properties these materials in general possess, which explains the interest of chemists and physicists in NCs. Section 2.3 presents the theory behind the main synthesis method in the work, the "hot injection" method. The final section, section 2.4, will present the theory behind cation exchange reactions, a versatile post-synthesis tool for metal chalcogenide NCs.

## 2.1. Bulk semiconductors and quantum confinement

A bulk semiconductor, containing around $10^{20}$ atoms/cm$^3$, forms two energy bands rather than discrete energy levels as within a single atom. The formation of these bands can be described by the Tight binding/LCAO method.[1] Here, the individual atomic orbitals within the solid are coupled to form molecular orbitals. The summation of the molecular orbitals gives rise to a band, with the most bonding combination being the lowest in energy and the most antibonding combination the highest in energy (Figure 2.1). Within a band, the difference between the energy levels are so small compared to thermal energy kT, that full motion of the electrons is allowed. Therefore, the energy bands can be considered as quasi-continuum. The band formed by the coupling of the Highest Occupied Molecular Orbitals (HOMO) is called the valence band and the band formed the coupling of the Lowest Unoccupied Molecular Orbitals (LUMO) is called the conduction band. The gap between the valence and conduction band is called the bandgap ($E_g$). The bandgap of a bulk semiconductor is in generally between 0.1 and 4 eV.

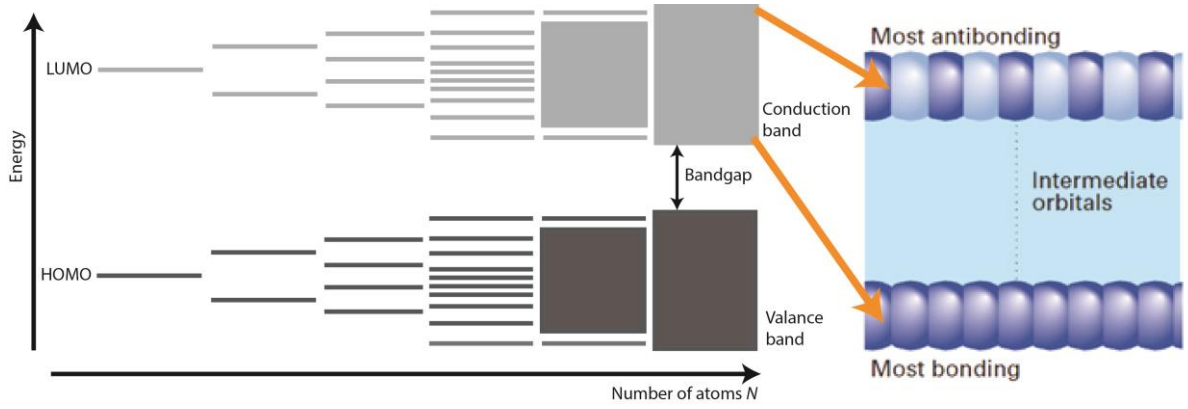


**Figure 2.1: Schematic representation of the band formation in a semiconductor. Adapted from ref.** [1]

The electronic structure of a semiconductor, as described above, can be altered when at least one of the dimensions of a semiconductor crystal falls within the nanometer range (<100 nm). In this size regime, quantum confinement effect starts to play an important role. The quantum confinement effect originates from the

decoupling of molecular orbitals due to the decreasing amount of atoms within the nanocrystals. This can be seen as the reverse of the formation of the electronic bands as shown in Figure 2.1. Therefore, with decreasing crystal size comes an increase of the bandgap as shown in Figure 2.2. Furthermore, with decreasing crystal size, less atomic orbitals contribute to the overall band structure and thus more discrete energy levels arise at the edges of the valence and conduction band. One of the major influences of this changing bandgap is represented in the optical properties of quantum dots, which will be further described in section 2.2.

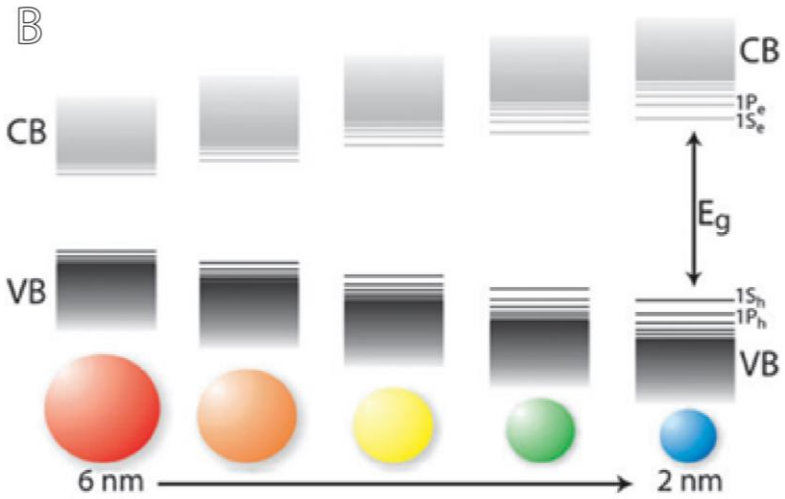


**Figure 2.2: Quantum confinement for a nanocrystal. When decreasing the size of the particle, the bandgap ($E_g$) increases and more discrete levels at the band edges are formed. Reproduced from ref.[2]**

A more quantitative way to look at quantum confinement can by derive from the special extension of the exciton wavefunction, the exciton Bohr radius. The exciton Bohr radius as can be described as shown in equation 2.1, with ħ (Planck constant divided by 2π), the permittivity ε, the elemental charge *e* and the effective masses of the electron and hole $m_e$ and $m_h$.[3]

$$a_0 = \frac{\hbar\varepsilon}{e^2}\left(\frac{1}{m_e} + \frac{1}{m_h}\right) \qquad (2.1)$$

When the size of a NC falls below $4a_0$, quantum confinement effects start to influence the electronic properties of the NC. In general, a smaller bulk $E_g$ means that the bonds are more covalent and thus the exciton is more delocalized. This leads to $m_e$ and $m_h$ becoming lighter and thus an increase in $a_0$. In other words, a larger bandgap leads to a smaller $a_0$ and therefore smaller sized quantum dots are needed to observe the quantum confinement effect. For instance, for CdS ($E_g$ = ~2.6 eV) the exciton Bohr radius is 2.7 nm where for CdTe ($E_g$ = ~1.6 eV) the exciton Bohr radius is 6.7 nm.[4] CdS thus requires smaller sizes of nanocrystals to exhibit quantum confinement effects compared to CdTe.

As mentioned above, the quantum confinement effects are strongly depended on the dimensionality of the NCs. Therefore, NCs can be divided in four different types; bulk, quantum wells (QWs), quantum wires (or rods, QRs) and quantum dots (QDs). With a QD, quantum confinement occurs in all directions since all three dimensions are smaller than $4a_0$. QRs, which are NCs were one dimension is larger than $4a_0$, experience only quantum confinement effects in the transverse direction of the wire. When changing the dimensionality of the NCs to only one dimension within the range of quantum confinement effects, the confinement is only experienced in one direction, which is perpendicular to the plane. These are also known as quantum wells. Carriers within a quantum well are thus freely moving in two dimensions but confined in one dimension. This leads to some interesting effects for quantum wells.[5–7]

The difference between bulk, quantum wells, quantum wires and quantum dots can be further explained by looking at the density of states. With decreasing dimensionality, the carrier energy distribution is narrowed to specific energies as described earlier. For a quantum well, this means that the density of states distribution changes from a square root dependence to step like a dependence, as shown in Figure 2.3. Also, with decreasing dimensionality comes an increase in the ground state which is comparable to increasing the dimensionality of a particle in a box.[1] This means that the first available state of bulk (Eg) lies lower in energy compared to the first available state of a quantum well ($E_1$). Overall, the quantum confinement effects, and thus the properties, differ for quantum dots, wires and wells with the same thickness (or diameter for QDs). Therefore the study of quantum wells, from here on called nanosheets (NSs), opens up routes to a novel class of materials with for instance exciting optical properties.[8]

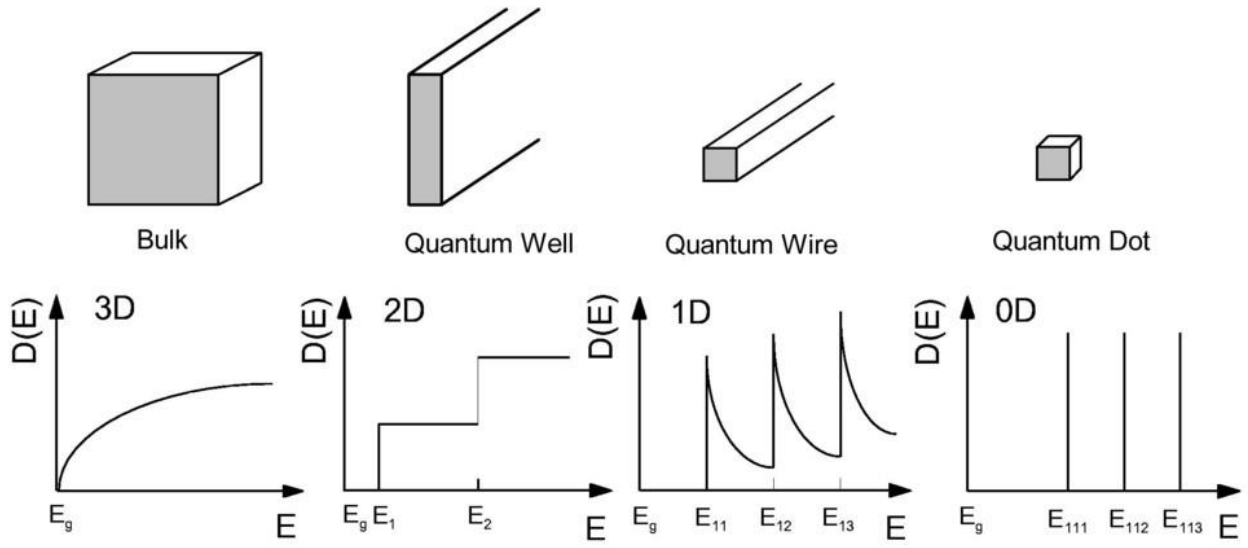


**Figure 2.3: Schematic illustration of the density of states (DOS) as a function of energy for; (A) a bulk material (three-dimensional), (B) a quantum well (two-dimensional), (C) a nanowire (one-dimensional), and (D) a quantum dot (zero-dimensional). Reproduced from ref.[9]**

## 2.2. Surface effect and optical properties of nanocrystals

As mentioned above, NCs are interesting due to their novel properties compared to their bulk equivalents. One of these properties comes from the drastic change in the surface to volume ratio. Surface atoms have unshared atomic orbitals (so-called dangling bonds) and therefore are higher in free energy and more reactive compared to bulk atoms. In bulk materials, the contribution of these surface atoms is negligible due the low percentage of surface atoms. When decreasing a semiconductor crystal to the order of several nanometers (1-5 nm), the surface to volume ratio start to rapidly increase, as shown in Figure 2.4A. Within this nanosized regime, evaporation and melting points generally decrease, as shown in Figure 2.4B. Furthermore, the reactivity, plasticity, solubility and the ability to form stable colloidal dispersions of these nanocrystals increase within the nanometer regime.

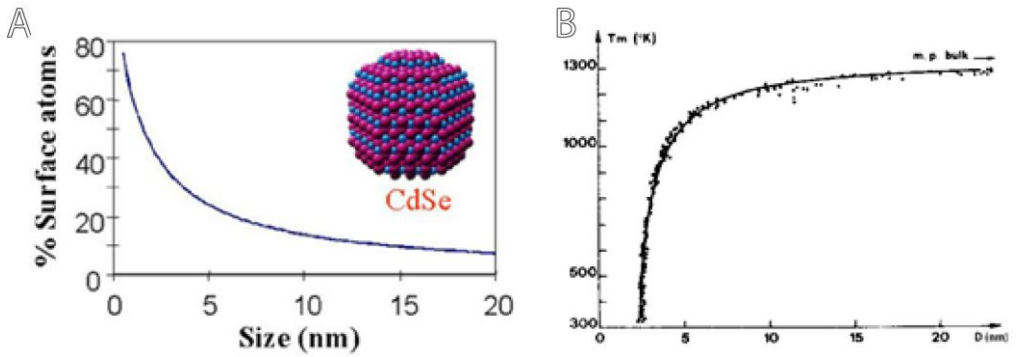


**Figure 2.4: (A) Percentage of surface atoms depending on the size of a CdSe quantum dot. Reproduced from ref.[3] (B) Melting point of colloidal gold nanocrystals plotted versus the radius. Below ~5 nm the melting point drastically drops due to the strong influence of surface atoms. Reproduced from ref.[10]**

To excite an electron across the bandgap in semiconductor (for instance 1.74 eV for bulk CdSe), thermal energy alone is not sufficient, since kT is only 0.038 eV.[4] The electron can be excited from the valence band to the conduction band by absorbing a photon with an energy equal to, or higher than $E_g$. When the electron is excited to the conduction band, it will non-radiative relax to the conduction band edge by losing its excess of energy to the crystal lattice in the form of heat. From the band edge, the electron can further relax to the valence band by emitting a photon with the energy difference between the two band edges. This process is called photoluminescence and is shown in Figure 2.5A. The bandgap, and thus the optical properties of semiconducting nanocrystals, are size dependent due to quantum confinement effects. This means that NCs can cover a wide range of different band gaps and thus a wide range of absorption and emission bands solely by changing the crystals size as shown in Figure 2.5B and C. The property to either absorb photons or emit photons with a specific energy can be used for various applications like LEDs or solar cells.

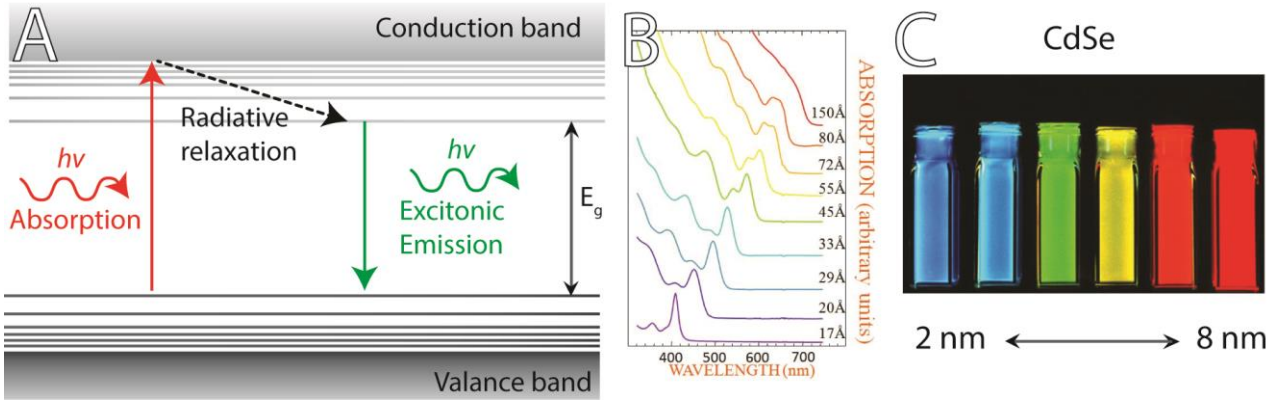


**Figure 2.5: Optical properties of quantum dots. (A) Schematic representation of absorption and photoluminescence in a quantum dot. (B) A series of CdSe QDs ranging from 1.2-11.5 nm showing a red shift of the absorption with increasing the QDs size. (C) The same CdSe quantum dots emitting at different wavelengths under a UV lamp. Reproduced from ref.[11]**

### 2.3. Synthesis of nanocrystals: "Hot injection" method

One of the most commonly used bottom-up approaches for the synthesis of colloidal NCs has been developed by Murray *et al.* and is the "hot injection" method.[4] Here, a cold (room temperature) solution, usually containing the chalcogenide precursor, is rapidly injected into a hot solution containing the metal precursor. At first, the high injection temperature creates a burst of nuclei, but due to the rapid drop in temperature after the injection, the further formation of nuclei is stopped. The sudden burst of nuclei is followed by a drop of the precursor concentration below the super saturation level. The lower temperature allows the nuclei to grow without the formation of new nuclei, so nucleation and growth are separated, resulting in controlled growth of nuclei. If the growth and nucleation are not well separated, new nuclei will be formed during the growth of the other nuclei, leading to a high size distribution of the final NCs.

The hot injection method can described with the classical nucleation theory.[2] In the classical nucleation theory, the change in the Gibbs free energy $\Delta G_{tot}$, as given in equation 2.2, is used to determine the growth of the nuclei. Here, the Gibbs free energy is determent by the volume free energy $\Delta G_v$, the surface free energy $\gamma$ and the radius of the nuclei $r$.

$$\Delta G_{tot} = \frac{4}{3}\pi r^3 \Delta G_v + 4\pi r^2 \gamma \qquad (2.2)$$

In Figure 2.6 the Gibbs free energy is plotted versus the radius of the nuclei. When the radius of the nuclei is small, the free energy will be dominated by the surface free energy since its $r^2$ dependency. This is due to the large surface to volume ratio of small nuclei. With increasing $r$, the volume free energy starts to dominate the surface free energy due to its $r^3$ dependency. This leads to an energy barrier $\Delta G^c$ at the critical radius $r_c$.

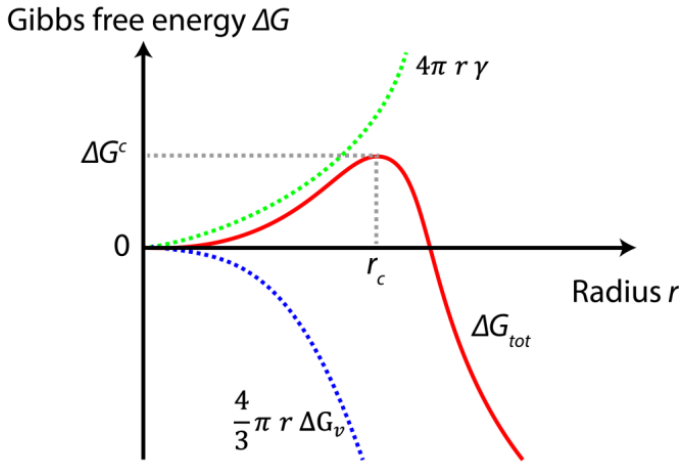


**Figure 2.6: Gibbs free energy for the formation and growth of nuclei. When a nuclei reaches the energy barrier $\Delta G^c$ at the critical radius $r_c$, it can either gain energy by dissolving or by growing into a larger NC.**

The critical radius can be derived by dΔG(n)/dr=0, which is given in equation 2.3. At the critical radius, the nuclei can decrease their free energy when either $r < r_c$, or when $r < r_c$. When $r < r_c$, the nuclei can lower their free energy by decreasing their size and thus by dissolving. When the nuclei have an $r > r_c$, the nuclei will lower their free energy by increasing $r$ and thus by growing. Further growth will eventually lead to a negative $\Delta G_{tot}$ and thus to the irreversibly growth of the nuclei into larger NCs.

$$r_c = {}^{2\gamma}/_{|\Delta G_v|} \qquad (2.3)$$

## 2.4. Cation exchange

A recently developed tool in the synthesis of semiconductor NCs is the use of cation exchange (CE). Here, the cations in the NCs can be replaced by new cations with the preservation of the size and shape of the NCs. CE reactions have been carried out over a wide range of NCs including CdSe to $Cu_{2-x}Se$ and to ZnSe, and $Cu_2S$ to either CdS or PbS (Figure 2.7A and B).[12,13] This has led to a whole new range of NCs which cannot be synthesized in a direct fashion. For instance, metastable rocksalt CdSe NCs have been synthesized from rocksalt PbSe NCs, whereas the most stable form of CdSe is wurtzite.[14] With the fine-tuning of the concentrations, the added precursors, temperature and the surfactants used it is even possible to make ternary or even quaternary like $Zn_xCd_{1-x}Se$ or CuInZnS NCs by using partial CE.[15,16]

CE reactions are thermodynamically driven by choosing the proper solvents and surfactants. For instance, when exchanging soft $Cu^+$ for a harder metal ($Pb^{2+}$, $Cd^{2+}$ or $Zn^{2+}$), the cation exchange reaction is carried out with the addition of a soft base like trioctylphosphine (TOP) or tributylphosphine.[12,13] Predicted by the Hard-Soft-Acid-Base theory (HSAB), TOP will bind strong to the soft monovalent $Cu^+$ and weak to the hard divalent $Pb^{2+}$, $Cd^{2+}$ or $Zn^{2+}$. Therefore, TOP will extract $Cu^+$ out of the NCs sublattice.[17] The vacancies left behind from the $Cu^+$ can

be filled by the new metal cation. This equilibrium can thus led to either a partial or full cation exchange towards the new NCs. Overall CE can be considered as a versatile tool which can be used to make complex structures which are not attainable in a direct synthesis.

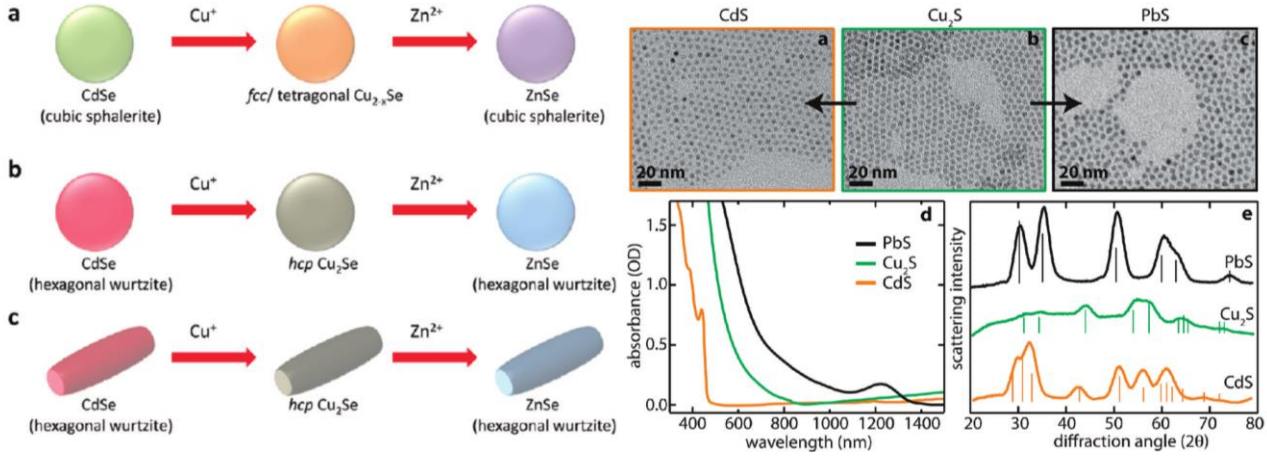


Figure 2.7: Examples of possible routes for CE. (A) CE starting from CdSe to $Cu_{2-x}Se$ to ZnSe for different kind of shapes and initial crystal structures. Reproduced from ref.[12,13] (Bl) CE from $Cu_2S$ to CdS and PbS with size and shape preservation as sown with TEM. Furthermore XRD and optical measurements confirmed the exchange towards CdS and PbS. Reproduced from ref. [13]

## References


1. Shriver & Atkins – Inorganic Chemistry, 5th Ed., 2010, Oxford Pub.

2. C. de Mello Donegá. Synthesis and Properties of Colloidal Heteronanocrystals. *Chem. Soc. Rev.* **2011**, *40*, 1512–1546.

3. C. de Mello Donegá, Utrecht University, Lectureslides "Electronic Structure of Nanomaterials, Nanomaterials 2011.

4. C. B. Murray; D. J. Norris. Synthesis and Characterization of Nearly Monodisperse CdE (E = S, Se, Te) Semiconductor Nanocrystallites. *J. Am. Chem. Soc.* **1993**, *115*, 8706–8715.

5. L.-S. Oriol; L. Dominik; K. Metin; R. Aleksandra; K. Andras. Ultrasensitive Photodetectors Based on Monolayer MoS2. *Nat. Nanotechnol.* **2013**, *8*, 497–501.

6. B. Radisavljevic; a Radenovic; J. Brivio; V. Giacometti; a Kis. Single-Layer MoS2 Transistors. *Nat. Nanotechnol.* **2011**, *6*, 147–50.

7. Q. H. Wang; K. Kalantar-Zadeh; A. Kis; J. N. Coleman; M. S. Strano. Electronics and Optoelectronics of Two-Dimensional Transition Metal Dichalcogenides. *Nat. Nanotechnol.* **2012**, *7*, 699–712.

8. S. Ithurria; M. D. Tessier; B. Mahler; R. P. S. M. Lobo; B. Dubertret; A. L. Efros. Colloidal Nanoplatelets with Two-Dimensional Electronic Structure. *Nat. Mater.* **2011**, *10*, 936–941.

9. Ulm University, Http://www-Opto.e-Technik.uni-Ulm.de/lehre/cs/, 30-11-2013.

10. B. Buffat. Size Effect on the Melting Temperature of Gold Partlclese. *Phys. Rev. A* **1976**, *13*, 2287–2298.

11. C. B. Murray. Synthesis and Characterization of Nearly Monodisperse CdE (E = S, Se, Te) Semiconductor Nanocrystallites. *J. Am. Chem. Soc.* **1993**, *115*, 8706–8715.

12. H. Li; M. Zanella; A. Genovese; M. Povia; A. Falqui; C. Giannini; L. Manna. Sequential Cation Exchange in Nanocrystals: Preservation of Crystal Phase and Formation of Metastable Phases. *Nano Lett.* **2011**, *11*, 4964–4970.

13. J. M. Luther; H. Zheng; B. Sadtler; a P. Alivisatos. Synthesis of PbS Nanorods and Other Ionic Nanocrystals of Complex Morphology by Sequential Cation Exchange Reactions. *J. Am. Chem. Soc.* **2009**, *131*, 16851–16857.

14. J. M. Pietryga; D. J. Werder; D. J. Williams; J. L. Casson; R. D. Schaller; V. I. Klimov; J. A. Hollingsworth. Utilizing the Lability of Lead Selenide to Produce Heterostructured Nanocrystals with Bright, Stable Infrared Emission. *J. Am. Chem. Soc.* **2008**, *130*, 4879–4885.

15. S. Lou; C. Zhou; W. Xu; H. Wang; S. Zhou; H. Shen; L. S. Li. Facile Synthesis of Water-Soluble ZnxCd1−xSe Nanocrystals via a Two-Phase Cation Exchange Method. *Chem. Eng. J.* **2012**, *211-212*, 104–111.

16. L. De Trizio; M. Prato; A. Genovese; A. Casu; M. Povia; R. Simonutti; M. J. P. Alcocer; C. D. Andrea; F. Tassone; L. Manna. Strongly Fluorescent Quaternary Cu − In − Zn − S Nanocrystals Prepared from Cu 1 - X InS 2 Nanocrystals by Partial Cation Exchange. **2012**,

17. A. E. Martell. Hard and Soft Acid-Base Behavior in Aqueous Solution: Steric Effects Make Some Metal Ions Hard: A Quantitative Scale of Hardness-Softness for Acids and Bases. *J. Chem. Educ.* **1996**, *73*, 654–661.

# 3. Ultrathin $Cu_{1.8}S$ nanosheets

## 3.1. Introduction

The main focus of this work is the size, shape and composition control over copper-chalcogenides, and Copper(I) sulfide ($Cu_{2-x}S$) in particular. The interest in $Cu_{2-x}S$ comes from its intrinsic bandgap around 1.2-1.5 eV, which makes $Cu_{2-x}S$ ideal for photovoltaic applications and solar cells.[1–6] $Cu_{2-x}S$ nanocrystals (NCs) can be synthesized in a large variety of morphologies.[1,3,6] Furthermore, the $Cu^+$ ions can be replaced for a large range of other metal cations such as $Cd^{2+}$, $Pb^{2+}$, $Ag^+$ and $Zn^{2+}$ by the use of the post-synthesis cation exchange method.[7–10] Therefore, copper chalcogenides are highly suitable for opening up new routes towards control over size, shape and composition over metal chalcogenide NCs, as will be described in this chapter.

Ultrathin 2-dimensional (2D) materials (thickness l<2.5 nm thick) are currently attracting great scientific interest due to their unique electronic and structural properties, which emerge from the confinement of charge-carriers in a plane that is just a few atomic layers thick. For instance, monolayered $MoS_2$ nanosheets (NSs), the most studied 2D material, has been successfully used for the fabrication of transistors, photo-detectors and electroluminescent devices due to its high carrier mobility, direct bandgap and transparency.[11–13] Furthermore, colloidal CdE (E = S, Se, Te) NSs have shown ultra-fast emission, which may be useful for quantum cascade lasers.[14,15] Finally, semiconductor NSs have been proposed as efficient host materials for Li-ion batteries, as the thin NSs can effectively accommodate large volume changes induced during the charge/discharge process.[16]

The currently most used methods for the preparation of nanosheets are exfoliation of bulk material or by chemical vapor deposition.[11–13] Both methods result in thin layers, but offer limited control over the final thickness and lack control over the shape and lateral dimensions of the NSs. Furthermore, these techniques are not suitable for large scale production of free-standing NSs. Synthesis of colloidal 2D NSs have only recently been reported and are limited to a few compositions: SnSe (l= 1 nm), PbS (l= 2.8 nm), $In_2S_3$ (l= 0.76 nm) and CdA (A=S, Se ,Te, l= 1.2-2.1 nm) NSs.[14,15,17–20] The Cd-based NSs are the only currently synthesized colloidal NSs for which the thickness can be controlled. Nevertheless, shape and size control in the lateral dimensions has not yet been achieved for any colloidal NSs. Additionally, these NSs are often entangled and curled and therefore have limited applicability for self-assembled thin films.[14]

In this chapter, a new method to synthesize colloidal ultrathin hexagonal digenite $Cu_{1.8}S$ NSs will be described. This chapter is organized as follows. The experimental section, section 3.2, will describe the details of the $Cu_{1.8}S$ NSs synthesis. This synthesis was thoroughly investigated by varying growth conditions, concentrations and different precursors (sections 3.3.1-3.3.5) leading to both control over the size and shape of the nanosheets, as

well as a mechanism explaining the formation of these nanosheets (section 3.3.6). The synthesis of CdS, PbS and ZnS NSs by cation exchange reactions on the $Cu_{1.8}S$ NS is described in sections 3.3.7. The conclusions drawn from the $Cu_{1.8}S$ NSs will be described in the section 3.4 and an outlook will be given in section 3.5.

## 3.2. Experimental

The following sections will contain the experimental part for the syntheses of the ultrathin hexagonal NSs. After the used materials, the general synthesis of the $Cu_{1.8}S$ NSs will be described in section 3.2.2. Section 3.2.3 will contain the cation exchange method used to synthesize CdS, PbS and ZnS NSs. Sections 3.2.4-3.2.8 will cover the used equipment, including more details on the syntheses (3.2.4), electron microscopy (3.2.5), X-ray diffractometry (3.2.6), absorption and photoluminescence spectroscopy (3.2.7) and the excited state lifetime measurements (3.2.8).

### 3.2.1. Materials

Copper(I) acetate (CuOAc, 97%) and tin(IV) tetrabromide ($SnBr_4$, 99%) were purchased from Sigma Aldrich and used without any further purification. Other metal salts used for the experiments were also bought from Sigma Aldrich, such as tin(II) dibromide ($SnBr_2$), tin(IV) tetrachloride pentahydrate ($SnCl_4.5H_2O$, 98%), tin(IV) acetate ($SnOAc_4$), copper(I) chloride (CuCl, 97%), copper(I) bromide (CuBr, 98%), sodium bromide (NaBr, ≥99%), sodium chloride (NaCl, trace metal, 99.999%), lead(II) acetate trihydrate (PbOAc2·3H2O, 99.999% trace metals basis), cadmium(II) nitrate tetrahydrate (Cd(NO3)2·4H2O, 98%) and zinc(II) dichloride (ZnCl2, 98+%) and were used without further purification. Sulfur powder was obtained from Strem chemicals. Ligands and solvents were purchased from Sigma Aldrich, like trioctylphosphine (TOP, 90%), tributylphosphine (TBP, 99%), 1-Dodecanethiol (DDT, ≥98%), 1-octadecene (ODE, tech., 90 %), trioctylphosphine oxide (TOPO, 99%), oleylamine (OLAM, tech., 70%), 1,9-nonanedithiol (95%), 1-octadecanethiol (98%), 2-phenylethanethiol (98%), anhydrous toluene, methanol and butanol. ODE, TOPO and OLAM were degassed prior to synthesis.

### 3.2.2. $Cu_{1.8}S$ ultrathin hexagonal nanosheets

The synthesis of the $Cu_{1.8}S$ NSs is an adaptation of a method described by Wang *et al.* but with the addition of $SnBr_4$.[6] Typically, 27.3 mg (0.22 mmol) of CuOAc and 32.85 mg (0.075 mmol) of $SnBr_4$ were dispersed in 12.5 mL ODE together with 0.55 g of TOPO. The mixture was degassed for 30 minutes at a temperature of 100 °C. After the degassing, the dark brown solution was gradually heated to 160 °C and at this temperature, 0.5 mL DDT was swiftly injected under a vacuum. Directly after the injection, the reaction solution turned clear yellow and was purged with a $N_2$ gas flow. The temperature was further increased to 220 °C and turned turbid brown at ~200 $^0$C. The solution was maintained at 220 °C for 40 minutes. The $Cu_{2-x}S$ nanosheets were precipitated by

adding a methanol/butanol solution and centrifuging at 3000 rpm for 15 minutes. Afterwards, the NSs were redispersed in toluene. The washing steps were repeated three times.

### 3.2.3. PbS, CdS, and ZnS NSs via cation exchange

The cation exchange (CE) reaction are performed as described by Luther *et al.*[9] Here, an excess (0.143 mmol) of either $PbOAc_2$, $Cd(NO_3)_2$ or $ZnCl_2$ was dissolved into 1 ml methanol and 100 µl TBP within a glovebox at room temperature. The precursor solution was rapidly injected into a heavily stirring 3 ml NSs dispersion (in toluene). The CE reaction was allowed to proceed overnight at room temperature. During the exchange of $Cu^+$ for $Cd^{2+}$, the solution slowly turned from brown to yellow in the first hours of the reaction, indicating the formation of CdS. The solutions for the exchange of $Cu^+$ for $Zn^{2+}$ and $Pb^{2+}$, exhibited the same behavior, where the reactions respectively turned colorless/white and black, indicating the formation of the ZnS and PbS NSs. As described by Luther *et al.*, one droplet of $Pb(OA)_2$ stock solution was added to aid the stability of the PbS NSs.[9] The $Pb(OA)_2$ stock solution was prepared by dissolving 0.1 mmol $PbOAc_2$ in 3.7 ml ODE and 1.7 ml OA. The cation exchanged NSs were precipitated by adding a methanol/butanol solution and centrifuged at 3000 rpm for 15 minutes. Afterwards, the NSs were redispersed in toluene.

### 3.2.4. Synthesis set-ups

For the hot-injection syntheses, the following set-up was used; a 50 ml 3-neck-roundbottomflask containing a magnetic stirring bean was fitted with two septa (one for the thermocouple and the other for the hot injection) and a Vigreux condenser. The Vigreux condenser was connected to a Schlenkline with a 2.5 torr vacuum and a 40 $L_n$/h nitrogen pressure. The heating source was a Horst HTMC1/69 thermocouple set at step 2 and was changed to step 1 20 $^0$C below the final growth temperature to prevent the temperature from rising too high. A VWR hotplate/stirrer was used for stirring and was set at 600 rpm. Samples were taken with a 20 mL glass syringe with an iron needle and stored in glass vials with a septum. These vials were prepared within a glove box to keep the samples oxygen free. The cation exchange reactions were performed in 20 ml glass vials placed on an A VWR hotplate/stirrer within a glovebox.

### 3.2.5. Electron microscopy

For the Transmission electron microscopy (TEM) measurements, a standard FEI Tecnai-10 or FEI Tecnai-12 was used. The energy dispersive x-ray spectroscopy (EDS) measurements were conducted with a FEI Tecnai-20F equipped with a Field Emission Gun, a Gatan 694 CCD camera and an EDA spectrometer. The microscope was operated at 200 kV. Acquisition time for the EDS measurements was 30 s. For the high resolution images, a FEI Titan Cs-corrected operated at 120 kV was used at Electron Microscopy for Materials Science (EMAT)

Antwerp. Samples were prepared on carbon coated polymer film copper grids (300 mesh) in a glove box by dropcasting 10-50 µl (depending on the dilution) of sample on the grids.

### 3.2.6. X-ray diffractometry

For the X-ray diffractometry, a Philips PW1729 x-ray generator and PW 3710 MBP controller were used at 40 kV and 20 mA and with a Cu $K_\alpha$ source ($\lambda$=1.5418 Å). Samples were prepared by dropcasting a concentrated NC solution on a Si wafer. The concentrated NC solution was prepared as follows. 1 mL of sample was sedimented with a methanol/butanol solution at 3000 rpm for 15 minutes and redispersed in a few drops of chloroform. The chloroform dispersion was dropcasted on a small piece of Si wafer and the chloroform was evaporated. The small piece of wafer was taped on an aluminum holder. The low angle measurements ranged from 5.3-25 degree. The crystal structure determination measurements ranged from 20-75 degree. In both cases multiple measurements (5-15 measurements, depending on the quality) were conducted to increase the signal to noise ratio.

### 3.2.7. Absorption and photoluminescence spectroscopy

Absorption spectra were measured on a Perkin-Elmer Lamdba 950 UV/VIS spectrophotometer. In general, samples were diluted in toluene and absorbance was measured from 280-800 nm with a step size of 1 nm. Samples measured from 280 to 2000 nm were redispersed in tetrachloroethylene (TCE) due to the strong absorbance of toluene at lower energies (<1100 nm). Photoluminescence (PL) and PL excitation spectra were measured on an Edinburgh Instruments Spectrofluorometer equipped with a detector sensitive in the visible region (either a Hamamatsu H7422-02 or Hamamatsu R928) and a 900W Xe lamp as source. Each spectrum consisted of three measurements to increase the signal to noise ratio. In general, a stepsize of 2 nm and a dwell time of 0.5 s were used. Samples were prepared in a glove box and transferred to quartz cuvettes (1 cm pathlenght), which were closed with a screwcap to keep the samples from oxidation.

### 3.2.8. Excited state lifetime measurements

Excited state lifetime measurements were performed on an Edinburgh Instruments set-up as described in the previous section. An Edinburgh Instruments EPL-375 Picosecond pulsed diode laser was used and set to a pulse rate of 50 µs. The samples were excited at 375 nm and the lifetime was measured at 630 nm. Samples were prepared as described in section 3.2.7.

## 3.3. Results and discussion

This section is organized as follows. The first section, section 3.3.1 will describe the general synthesis and properties of the $Cu_{2-x}S$ NSs. Section 3.3.2 discusses the influence of the growth time, concentration and growth temperature on the size and shape of the NSs. The third section discusses the influence of the solvent and the ligands used during the synthesis (3.3.3). The influence of the halide source will be discussed in section 3.3.4. Section 4.3.5 describes the influence of different used copper and sulfur precursors. A formation mechanism for the $Cu_{1.8}S$ NSs, based on the first five sections, will be described in section 3.5.6. The final section discusses the CdS, ZnS and PbS NSs obtained via CE reaction performed on the $Cu_{2-x}S$ NSs (section 3.5.7).

### 3.3.1. $Cu_{1.8}S$ ultrathin hexagonal nanosheets

When DDT is injected into degassed CuOAc, ODE and TOPO, (quasi-)spherical nanoparticles of approximately 9 nm (Figure 3.1A) are obtained, as has been reported by Wang *et al.*[6] When the synthesis is performed with the addition of a small amount of $SnBr_4$, as described in section 3.2.2, the size and shape of the nanoparticles is drastically changed from quasi-spherical to ultrathin hexagonal NSs, as shown in Figure 3.1B. These NSs tend to stack after dropcasting on a TEM-grid, indicating shape uniformity as shown in Figure 3.1C. From the TEM measurements, the size of the NSs was determined, being ~110 nm in diameter and ~2 nm in thickness (an aspect ratio of 55).

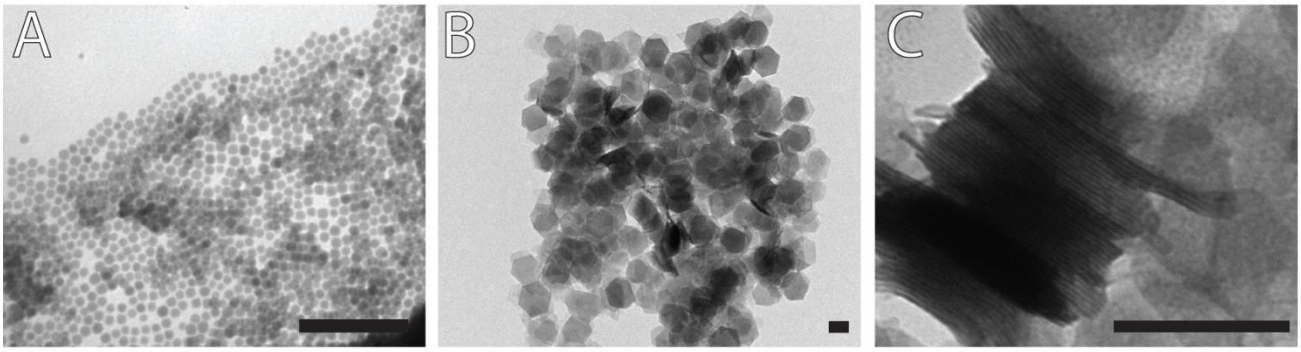


**Figure 3.1: TEM images of a synthesis without $SnBr_4$ (A) and with $SnBr_4$ (B), yielding spherical particles and hexagonal two-dimensional NSs, respectively. (C) TEM images of stacked nanosheets. Scale bars correspond to 100 nm.**

The uniformity in thickness is also displayed in the low-angle X-ray powder diffraction (XRD) measurements, as shown in Figure 3.2A. The stacked NSs give rise to a series of diffraction peaks at low angles. The 2θ separation between the observed peaks is 2.49 degree, corresponding to a periodic separation of 36.7 Å. The measured periodic spacing of 36.7 Å is in close agreement with the TEM measurements, as a sheet thickness of ~2 nm and a separation of ~1 nm (due to ligands) were measured, leading to a total thickness of ~3 nm. The diffractogram at higher angels showed only one sharp peak at 47°, indicating a $Cu_{1.8}S$ digenite crystal structure (Figure 3.2B). The

composition of digenite ($Cu_{1.8}S$) is in good agreement with the Cu:S ratio obtained from Energy-Dispersive X-ray Spectroscopy (EDS) measurements, where a typical ratio Cu:S of 1.79:1.00 was measured.

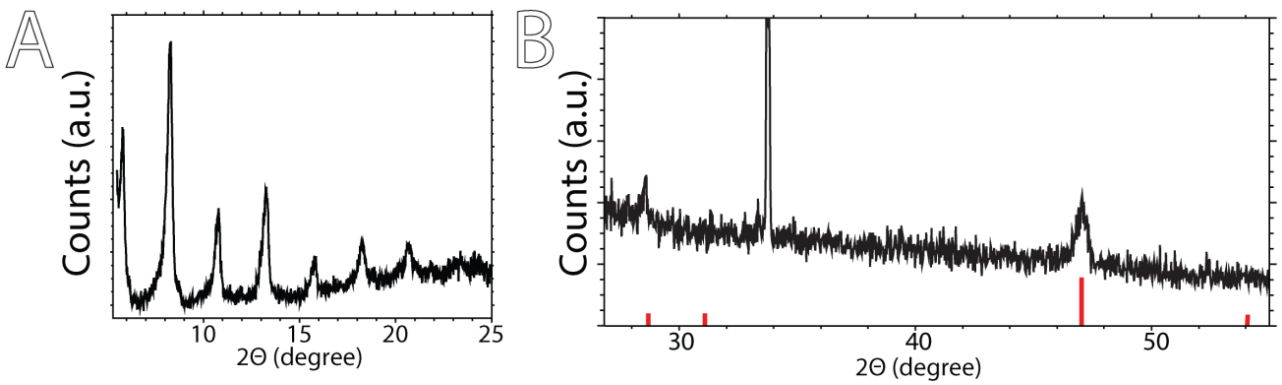


**Figure 3.2: Diffractograms at different angles of the $Cu_{1.8}S$ NSs with (A) a low angle diffractogram and (B) a diffractogram at higher angles. Red bars are from JCPDS card no. [47-1748] for hexagonal digenite.**

The thickness and crystallinity of the NSs was further investigated with High Resolution TEM (HRTEM) measurements. From the HRTEM images (Figure 3.3), a more precise thickness of the NSs was measured. The NSs are 1.96 nm thick with a 1.26 nm thick ligand layer, leading to total thickness of 3.22 nm. Furthermore, 5-6 monolayers per NSs were observed. Two lattice spacings were observed, one parallel to the surface (the {001} direction) and one perpendicular to the surface (the {002} direction). Based on the Fast Fourier Transform (FFT) (Figure 3.3A and C), a lattice spacing of 3.4 Å was determent. This proves that, although the NSs are very thin, they are crystalline.

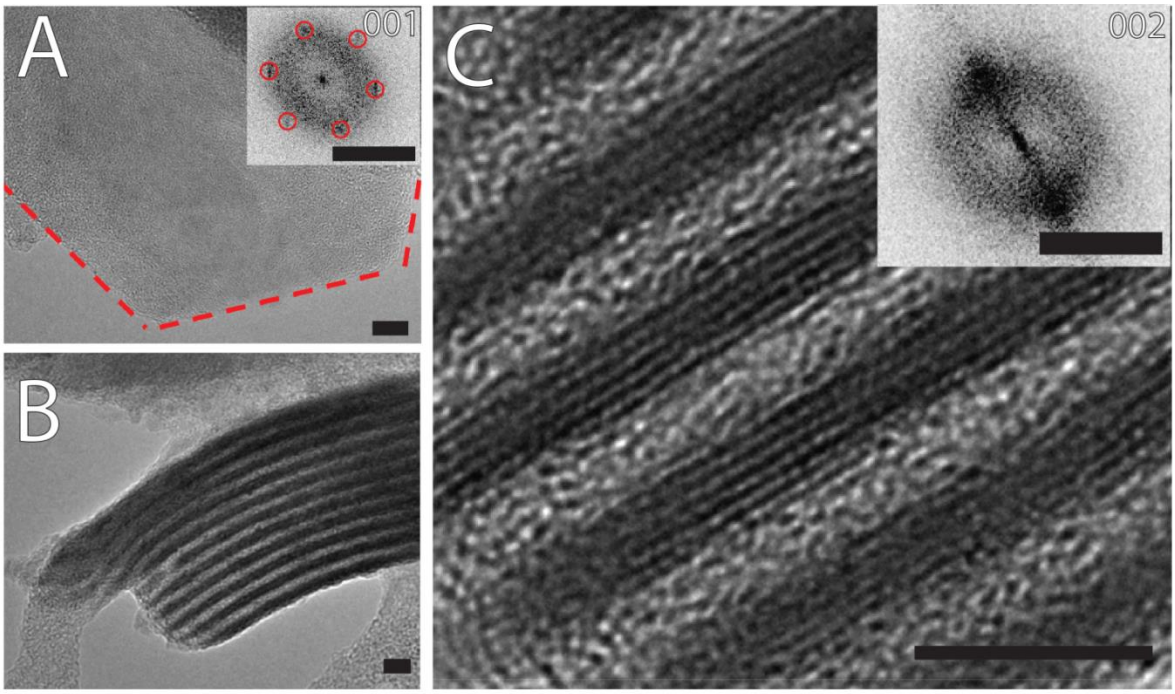


**Figure 3.3: High Resolution TEM images of the standard NSs viewed from the medial (A) and the lateral direction (B and C). Inset shows the FFT pattern. Scale bars correspond to 5 nm. Scale bars in insets correspond to 5 $nm^{-1}$.**

The absorption spectrum of the NSs (Figure 3.4) showed no Localized Surface Plasmon Resonance (LSPR). This could be due to the fact that the NSs are very thin and therefore the LSPR is too weak to be measured. This has also been seen for small $Cu_{2-x}S$ spherical nanoparticles, where a strong plasmon resonance is observed for particles of 5.9 nm and the LSPR is completely damped in the sub-3-nm regime.[21] The only absorption band observed is at 375 nm. Furthermore, the photoluminescence spectrum showed a red luminescence around 600 nm. The nature of the absorption and luminescence bands is further discussed in section 3.3.6.

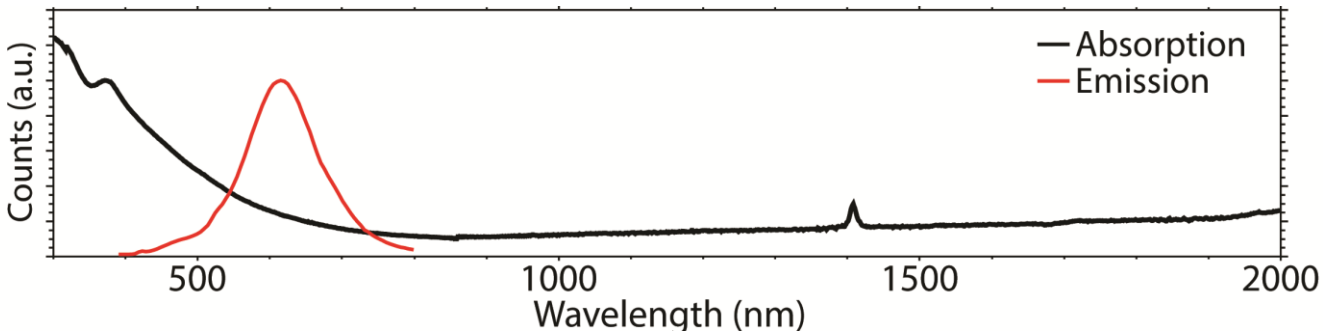


**Figure 3.4: UV/Vis-NIR absorption and photoluminescence spectra of the $Cu_{1.8}S$ NSs.**

Although it is evident that $SnBr_4$ plays a pivotal role in the formation of the $Cu_{1.8}S$ NSs, virtually no Sn was measured with EDS. Since it could be that the Sn-species are weakly bound to the NSs and are removed during the washing steps, an unwashed sample was measured with EDS. Again, no Sn was detected, excluding the possibility that Sn is washed out during the sample purification. On the other hand, a substantial amount of Br is observed in both the both washed and unwashed NSs (1.79:1.00.0.23 Cu:S:Br). Therefore, an EDS linescan and elemental mapping measurements were performed to see whether the Br is located at certain positions on the nanosheets, for instance only at the surface (Figure A3.1). It was found that Br was randomly distributed over the NSs, probably because they are highly mobile after exposure to the electron beam with long integration times. The role of the Br on the synthesis of the NSs is further discussed in sections 3.3.5 and 3.3.6.

### 3.3.2. Influence of growth time, temperature and solvent concentration

To gain insight into the formation mechanism of the ultrathin $Cu_{1.8}S$ NSs, the reaction was followed over time by taking intermediate samples as shown in Figure 3.5. Directly after injection, thin material could be observed with irregular sizes and shapes (Figure 3.5A). After 20 minutes, the hexagonal $Cu_{1.8}S$ NSs coexist with the irregular shaped thin material, suggesting that the irregular shaped thin material is a precursor for the NSs and is consumed over time (Figure 3.5B). The final sample, which was collected after 40 minutes, consisted solely of hexagonal NSs with a well-defined size and shape (Figure 3.5C). The irregular thin precursor did not contain any bromide and consisted of Cu and S in an elemental ratio of 1:1 (determent with EDS). This indicating these precursor are presumably Cu-thiolate complexes, comparable to those observed by Han *et al.*[22]

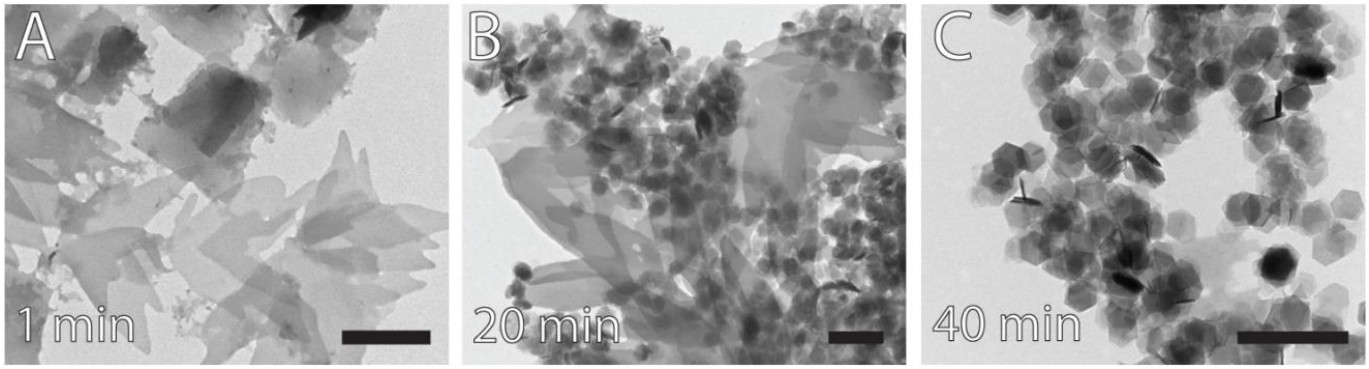


**Figure 3.5: Transmission Electron Microscopy (TEM) images of a NS synthesis followed over time by taking intermediate samples after (A) 1 minute, (B) 20 minutes and (C) 40 minutes. Scale bars correspond to 400 nm.**

The size in the lateral dimensions of the NSs were altered from approximately 110 nm to approximately 365 nm by adding more ODE, and thus making the synthesis more dilute (Figure 3.6). In this series of experiments, the molar amounts of precursors were unalterd, but the amount of non-coordinating solvent was varied from half of the ODE (Figure A3.2A) towards four times the amount ODE (Figure 3.6C). Ultrathin NSs were obtained with a well-defined hexagonal shape, only for the half amount ODE synthesis the NSs had a more triangular morphology and were more polydisperse in size. The sizes measured according to TEM for respectively the half ODE, one equivalent ODE (standard synthesis), two equivalents ODE and four equivalents ODE synthesis were 115 nm, 110 nm, 210 nm and 365 nm respective. It should be noted that the synthesis with four equivalents ODE (Figure 3.6C) needed a doubled reaction time for NSs to form.

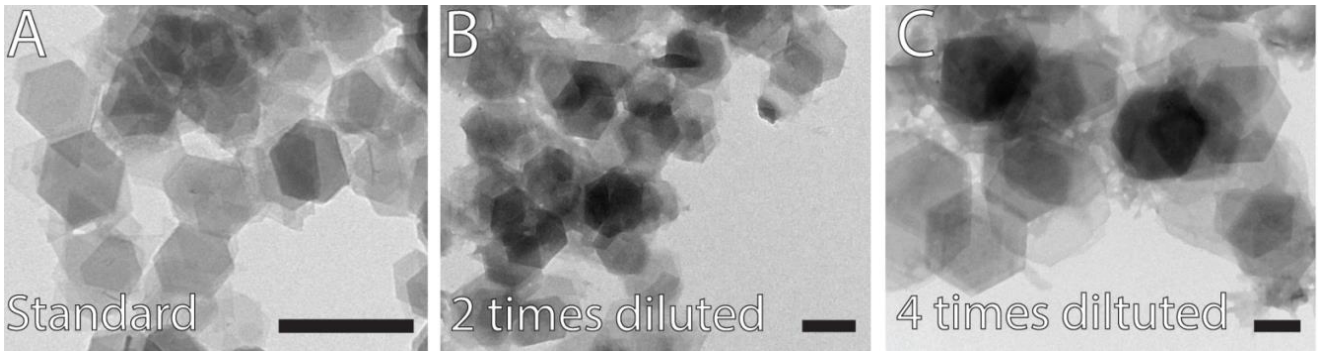


**Figure 3.6: TEM images of the size control of the NSs, with (A) the standard NSs as a comparison, (B) two times dilution and (C) four times dilution. Scale bars correspond to 200 nm.**

To further investigate the size and shape control of the $Cu_{1.8}S$ NSs, the influence of the growth temperature was investigated. The initial growth temperature for the NSs was set at 220 °C. After the DDT injection, a color change from clear yellow to turbid brown could be observed around 190 °C. Therefore, a NSs synthesis was carried out were the growth temperature was set at 190 °C. As Figure 3.7A shows, this synthesis also ultrathin nanosheets, but with a less defend shape. Presumably, these NSs are thinner and therefore form nanorolls to minimize their surface free energy. Furthermore, an experiment was carried out at 250 °C, which gave rise to comparable NSs as obtained at 220 °C. An important observation is that less stacks are observed, which could

indicate that these NSs are thicker and therefore stacking is less favorable (Figure 3.7B). Unfortunately, the control in thickness by varying the growth temperature could not be confirmed with low angle XRD due to time limitations.

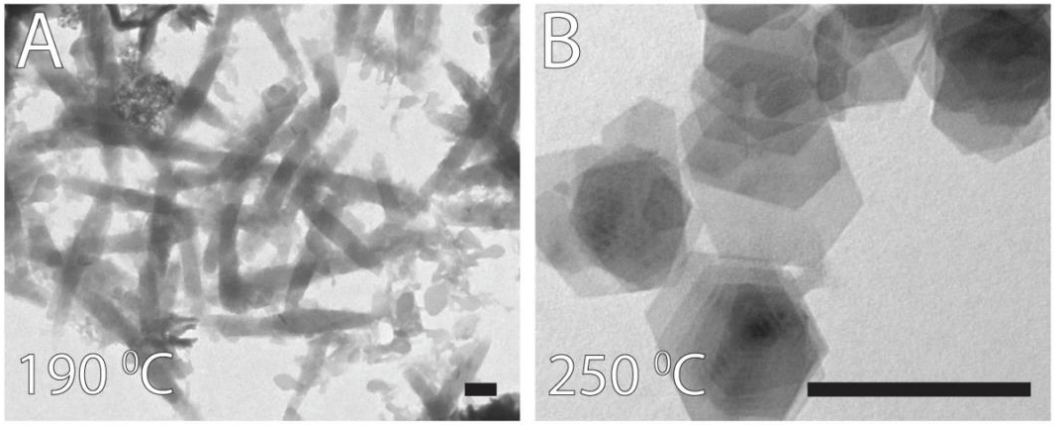


**Figure 3.7: TEM images of the NSs obtained at (A) a lower growth temperature of 190 °C and at (B) a higher growth temperature of 250 °C. Scale bars correspond to 200 nm.**

### 3.3.3. Influence of solvent and ligands

It is known in literature that both the non-coordinating solvent and ligands can play a vital role in the size and shape control of NCs synthesis.[23] To see whether changing the polarity of the solvent influenced the size and shape of the $Cu_{1.8}S$ NSs, a more polar solvent, diphenyl ether (DPE), was used (Figure A3.2). A 1:0.04 DPE:ODE mixture ($SnBr_4$ was dissolved in 0.5 ml ODE) showed more distorted hexagonal nanosheets, but no unreacted polymers for after 10 and 40 minutes. The lateral dimensions were unchanged compared to the normal synthesis. Therefore, it can be concluded that a more polar solvent accelerates the synthesis but thus not (strongly) influence the size and shape control.

When investigating the role of the ligand TOPO, it was found that the decrease of the added amount TOPO (from 550 mg to 100 mg), led to very large hexagonal NSs with a lateral size up to several micrometers (Figure 3.8A). When TOPO was completely removed from the synthesis, the large lateral dimensions were maintained but the shape changed from triangular to hexagonal (Figure 3.8B). In both cases, the thickness remained 2 nm, as XRD measurements showed the same periodic spacing of 36.7 Å at low diffraction angles (Figure 3.8C). Based on these results, it is expected that TOPO only binds to the NSs edges and thus only influences the growth in the lateral dimensions. Notable is the change in intensities between the diffraction peaks compared to the diffractogram of the standard NSs (Figure 3.2A). This can be explained by the stacking difference of the two samples. The standard NSs form large stacks consisting of up to tens of NSs. The μm sized NSs on the contrary, show no stacking due to their high aspect ratio (>1250!) and thus only show diffractions from the stacking of the nanosheets on top of each other. Spherical $Cu_{1.8}S$ dots were obtained when TOPO was replaced with TOP, the

non-oxidized version of TOPO (Figure 3.8D). TOP tends to strongly bind to copper ions, since they are a weak Lewis base and acid respectively, and therefore strongly influencing the shape of the final NCs. This further confirms that TOPO only inhibits the growth in the lateral dimensions.

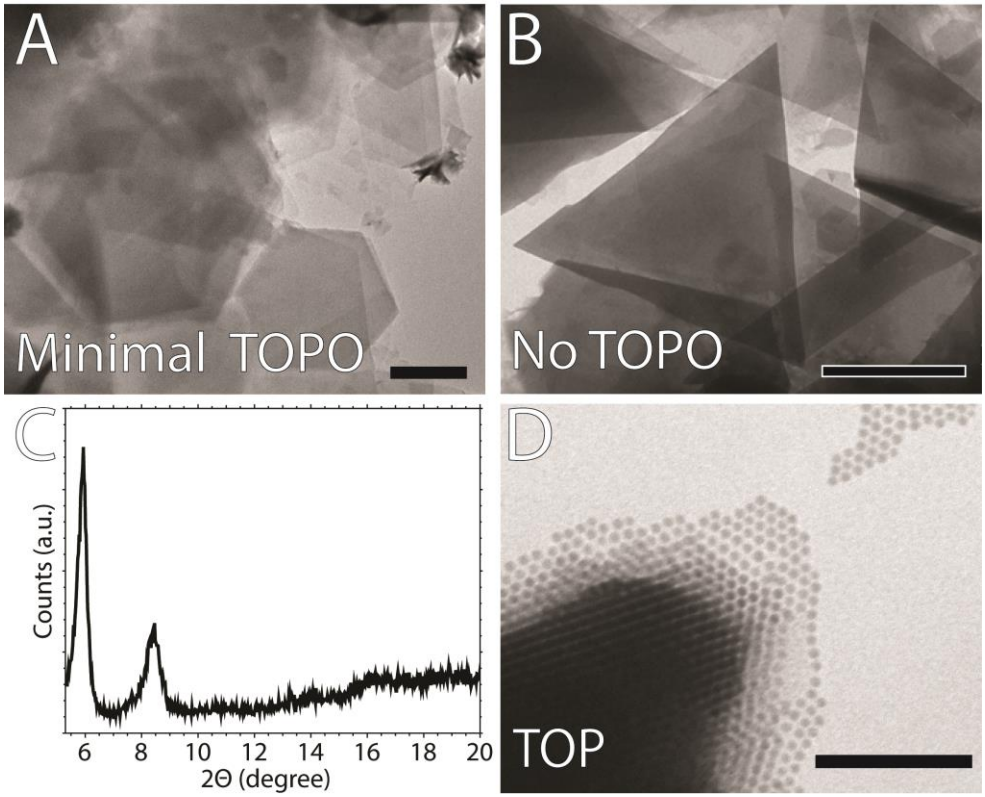


**Figure 3.8: TEM images showing the influence of the ligands; (A) NSs syntheses with 1/5 the amount of coordinating ligand TOPO and (B) without TOPO. (C) Low angle XRD diffractogram of these large NSs. (D) NSs synthesis were TOPO is replaced with TOP. Scale bars in (A) and (B) corresponds to 1 µm. Scale bar in (D) corresponds to 100 nm.**

The dispersed µm NSs were pink or red colored depending on the growth time as shown in Figure A3.3A, rather than brown as with the standard NSs. The red color was confirmed by absorption spectroscopies were two peaks around 515 nm and 575 nm where observed as shown in Figure A3.3B. The change of color for the larger NSs remains unclear and was not further investigated but could be related to the increased aspect ratios.

To see whether a more bulky phosphine oxide would influence to shape of the NSs, triphenylphospine oxide (TPPO) was used. As shown in Figure A3.4 this yielded a wide range of sizes and shapes like large irregular (up to µm) NSs, unreacted polymers and smaller sized and shaped nanosheets. Since the more 'hard' nature of the TPPO (HSAB theory),[24] it will bind less strongly to the copper explaining the large sized nanosheets observed, comparable to the size increase when removing the TOPO. Furthermore, TPPO is also more bulky compared to TOPO which leads to less ligands per edge surface and could lead to less control over the growth in the lateral dimensions.

### 3.3.4. Influence of the sulfur precursor

The influence of the sulfur precursor on the NSs was investigated by using a shorter and bulkier thiol (phenylethanethiol), a longer thiol (1-octadecanethiol) and a dithiol (1,9-nonanedithiol) as shown in Figure 3.9A, B and C respectively. Furthermore, elemental sulfur was used in as shown in Figure 3.9D. With all the different thiols, thin materials were obtained, whereas S powder yielded uncontrolled and very polydisperse particles. In the case of the shorter thiol (Figure 3.9A), the size and shape control was completely lost, whereas the dithiol (Figure 3.9C) resulted in what are presumably nanorolls. The longer alkylthiol yielded similar nanosheets as the standard synthesis, but more unreacted precursors are observed (Figure 3.9B). This might be related to the decreasing stability of [$CuSC_{18}H_{37}$] compared to [$CuSC_{12}H_{25}$].[25] Furthermore, the use 1-octadecanethiol yielded an increase of the stacking spacing from 3 nm towards 3.9 nm (Figure 3.9E), which could be caused by the longer alkyl-chain. What is evident from these experiments is that for controlled NSs growth, alkylthiols are necessary. The further role of the alkylthiols will be discussed in section 3.3.6.

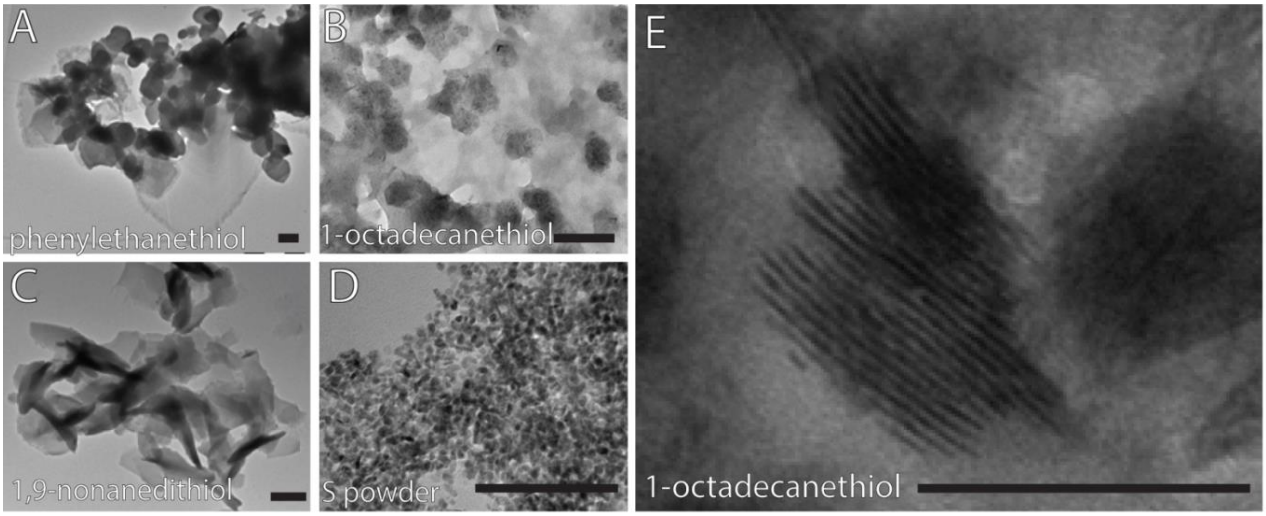


**Figure 3.9: TEM images of the experiments performed with different sulfur sources using (A) phenylethanethiol, (B+E) 1-octadecanethiol, (C) 1,9-nonanedithiol and (D) elemental sulfur. Scale bars corresponds to 50 nm.**

Next to sulfur containing precursor, different chalcogenides were used. As with the elemental sulfur, elemental selenium yielded irregular sized and shaped materials. Instead of DDT, 1-dodecaneselenol was also used as precursor. The use of 1-dodecaneselenol as precursor will be further discussed in chapter 5.

### 3.3.5. Influence of the copper and halide precursor.

In order to prove the hypothesis that the addition of halides, rather than Sn, induces the 2D growth, several control experiments were performed. In the first control experiment, $SnOAc_4$ was added as Sn-specie. As can be seen in Figure 3.10A, this led to spherical $Cu_{2-x}S$ nanocrystals, pointing in the direction that Sn has no influence

on the NSs formation and it is indeed the halide that is causing the two-dimensional growth. Furthermore, the minimal amount of $SnBr_4$ that is needed to induce the 2D growth was investigated by using different concentrations of $SnBr_4$. As shown in Figure 3.10B, adding halve the amount of $SnBr_4$ leds to an increase in irregular thin material. When the added amount of $SnBr_4$ was further decreased to ¼ mol of $SnBr_4$, no NSs were formed. Instead, this experiment yielded nanodisks as shown in Figure 3.10C. This shows that a certain minimal amount of bromide is needed to form the NSs.

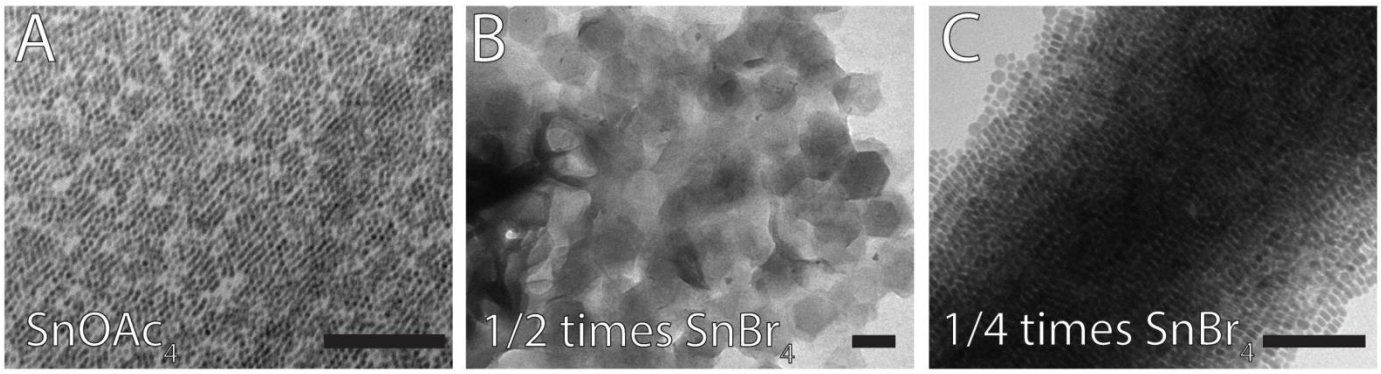


**Figure 3.10: TEM images of, (A) a synthesis with $Sn(OAc)_4$, (B) half the amount of $SnBr_4$ (½ $C_0$) compared to the standard NSs synthesis and (C) a quarter of $SnBr_4$ (¼$C_0$). $C_0$ = concentration of $SnBr_4$ in the NS synthesis. Scale bars corresponds to 100 nm.**

To further confirm the role of Br for the formation of the NSs, different bromide precursors were used. As shown in Figure 3.11A, replacing CuOAc and $SnBr_4$ with CuBr, yielded irregular thin material and a few hexagonal NSs. When additional Br-ions were added, in the form of NaBr, the irregular thin material disappeared and well-defined hexagonal NSs were obtained (Figure 3.11B). This further proves that Br causes the 2D growth NSs formation and that a minimal amount of bromides is needed to induce the formation of well-defined NSs. The later statement was further proven with a synthesis were $Sn(IV)Br_4$ was replaced with $Sn(II)Br_2$. This experiment yielded uncontrolled, crumbled thin material, presumably due to the fact that less Br was present, as shown in Figure 3.11C. Subsequently, the present Br-ions are less accessible as they are more strongly bound to Sn(II) compared to Sn(IV), according to the Hard-Soft-Acid-Base Theory (HSAB).[24]

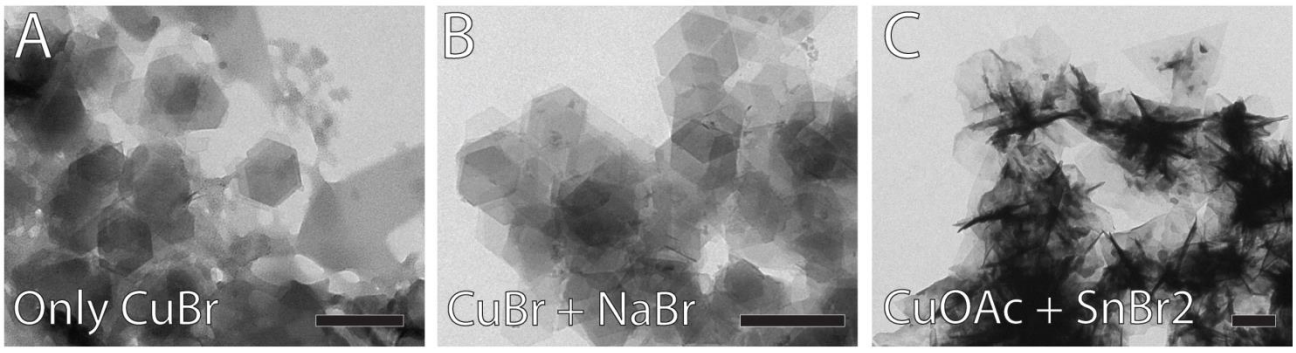


**Figure 3.11: TEM images of a NS synthesis with (A) only CuBr instead of CuOAc and $SnBr_4$, (B) CuBr with the additional of Br in the form of NaBr and (C) CuOAc with the addition of $Sn(II)Br_2$ instead of $Sn(IV)Br_4$. Scale bars correspond to 200 nm.**

The influence of the bromide was further investigated by using a different halide. When $SnCl_4$ was used instead of $SnBr_4$, triangular NSs with similar dimensions as the hexagonal NSs were obtained (Figure 3.12A and B). It should be noted that a threefold of $SnCl_4$ compared to the $SnBr_4$ was necessary for NS formation to occur. When $SnBr_4$ was replaced 1:1 with $SnCl_4$ disklike nanocrystals were obtained similar to those with ¼ $SnBr_4$ (Figure 3.12C and 3.10C). As with the hexagonal NSs, the triangular nanosheets showed large stacks (Figure 3.12B). XRD measurement showed that the triangular NSs had the same thickness and crystal structure as the hexagonal NSs (Figure A3.5). The difference between the needed amounts of $SnBr_4$ and chloride, could be explained with the HSAB theory.[24] Since Sn(IV) and Cl form a stronger bond than Sn(IV) and Br, less accessible halides are in solution.

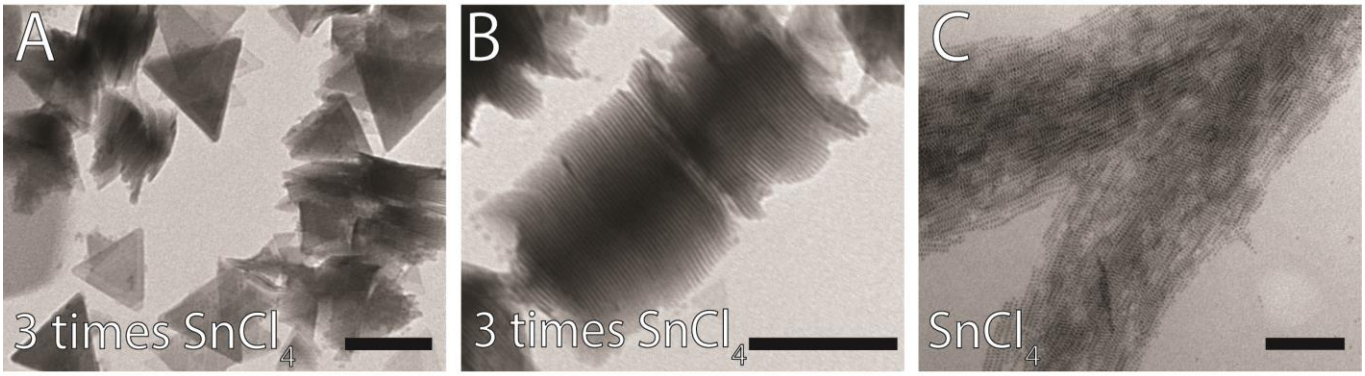


**Figure 3.12: TEM images of synthesis where $SnBr_4$ is replaced by $SnCl_4$. (A) Synthesis with the same amount of $SnCl_4$ ($C_{SnCl_4} = C_0$) and (B + C) with a threefold excess ($C_{SnCl_4} = 3C_0$). Scale bars correspond to 100 nm.**

When CuOAc and $SnCl_4$ where replaced with CuCl and NaCl, triangular NSs were still observed (Figure A3.6), confirming that Cl-ions yield triangular nanosheets whereas Br-ions result in hexagonal nanosheets. Why chlorides yield triangular NSs and bromides hexagonal NSs is unclear and should be further investigated.

### 3.3.6. Formation mechanism of the $Cu_{1.8}S$ NSs

In order to gain insight in the formation mechanism of the $Cu_{1.8}S$ NSs, the synthesis was monitored over time with absorption and photoluminescence (PL) spectroscopy (Figure 3.13). There was observed that preliminary samples, obtained 1 minute after the injection of DDT, were highly luminescent in the visible region and showed a strong absorption band in the ultraviolet at 375 nm (Figure 3.13A). Furthermore, from the absorption spectra it is clear that the absorption band decreases over time and that an absorption band around 700 nm arises, originating from the absorption of the $Cu_{1.8}S$ NSs. The inset of Figure 3.13A shows the PL of the samples that were collected overtime. There can be seen that the pre-injection solution (green line), was not luminescent, whereas directly after injection a broad and strong PL centered around 623 nm could be observed that, similar to the absorption band at 375 nm, decreased over time. In order to understand where this UV absorption band and

this visible PL originate from, a control experiment was conducted with without the addition of $SnBr_4$ (comparable to the synthesis of Figure 3.1A). Again, a strong absorption band was observed in the UV that decreased overtime, but at higher energies (340 nm), indicating that the precursor complex formed in this synthesis with halides present is not the same as for the synthesis without $SnBr_4$. In this synthesis, the pre-injection solution (green line) was weakly luminescent and the luminescence shifted directly after injection from 525 nm towards 500 nm and decreased overtime. These observations indicate that these luminescent species were precursor complexes and are consumed over time. Furthermore, different complexes are formed in the case of a synthesis with and without $SnBr_4$ added.

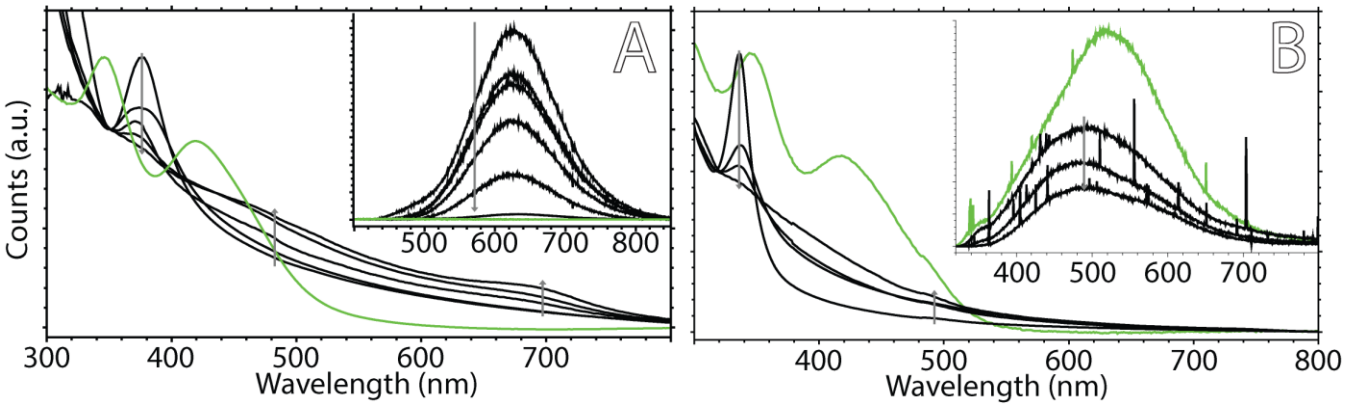


**Figure 3.13: Absorption and photoluminescence evolution over time (1-30 minutes) of a NSs synthesis with (A) $SnBr_4$ and without (B) $SnBr_4$ added. Insets show the PL of the samples.**

To verify where this absorption at 375 nm originates from, the metal salts were simply mixed in DDT and ODE and gradually heated slightly above the injection temperature (160 °C), but below the temperature at which $Cu_{1.8}S$ NS formation occurs (200 °C). The same absorption band for the standard synthesis was observed when the Cu- and Sn-salt were mixed in DDT and ODE, whereas the band observed at 340 nm was found when only the Cu-salt was added to DDT and ODE (Figure 3.14D). Furthermore, TEM showed that CuOAc and $SnBr_4$ in DDT yielded the same irregular thin material as observed previously as unreacted precursors in several syntheses (Figure 3.14B), whereas solely CuOAc in DDT yields a gel-like polymer (Figure 3.14A) similar to what has been seen by Han *et al.*[22] Furthermore, solely $SnBr_4$ in DDT (in the absence of CuOAc) resulted in large undefined clusters and no absorption band (Figure 3.14C).

As a final control experiment, solely CuBr was dissolved in DDT at slightly elevated temperatures (comparable to the synthesis in Figure 3.11A). This experiment resulted in the same absorption and PL features directly after injection as for the experiment with CuOAc and $SnBr_4$, as well as the standard NSs synthesis (Figure 3.14E). This means that those bands can be undoubtedly assigned to the Cu-thiolate complexes (Cu-thiolate at 340 nm and Cu-Br-thiolate at 375 nm), as well as the fact that Sn is not involved in the formation of the precursor

complexes and solely serves as a carrier for the Br-ions. The exact geometry of the Cu-Br-thiolate complexes although remains unknown.

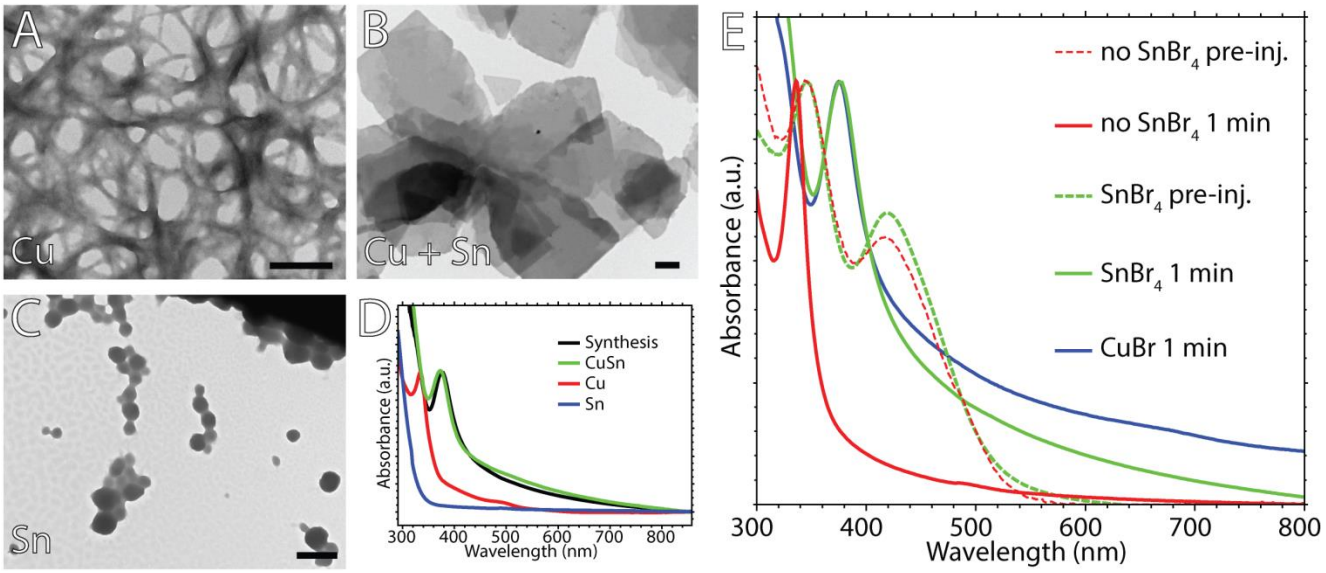


**Figure 4.14: TEM images (A-C) and absorption spectra (D) of the precursor samples prepared by mixing the metal salts in the coordinating solvent slightly below the nucleation temperature with (A) CuOAc in DDT, (B) CuOAc and $SnBr_4$ in DDT, and (C) $SnBr_4$ in DDT. (E) Absorption spectra of pre-injection sample and 1 minute samples of a NSs synthesis with and without $SnBr_4$, compared to the complex formed by mixing CuBr in DDT at elevated temperatures. Scale bars correspond to 500 nm.**

In another work performed in the group of Martin-Alvarez, there is stated that Cu(I)-thiolates can form tetranuclear platelike precursors that tend to stack in solution to form a liquid crystal.[25] These precursors are expected to polymerize in order to eventually evolve into zero-dimensional or one-dimensional nanocrystals overtime and they are thermally stable in solution up to 150 °C and maintain their platelike arrangement below this temperature.[3] Above this temperature, they tend to stack and form a columnar phase. At even higher temperatures (~200 °C), this columnar phase is broken and forms an isotropic phase that eventually leads to nanocrystal formation. There is expected that in our system these platelike columnar Cu-thiolate complexes bind with Br atoms and form another complex that is stable at elevated temperatures in their columnar phase. The columnar phase of the Cu-thiolates is preserved in this way and acts as a template for two-dimensional nanosheets growth, simultaneously limiting the growth in the direction of the c-axis.

In recent literature, a Cu-Br-thiolate complex was found and the so called $(CuBr)_5$ cluster had a hexagonal crystal structure, a two-dimensional morphology and an UV-absorption band with a strong PL in the red part of the electromagnetic spectrum, making it a very suitable candidate to compare to our reaction system.[26] In order to investigate whether this precursor photoluminescence is a material property or indeed related to the Cu-Br-thiolate complexes, excited state lifetime measurements were carried out. Very long lifetimes were observed in the µs range, indicating a similar ligand-to-metal energy transfer as seen by Espinet *et al.*[25] for Cu-Sn-thiol complexes (Figure 3.15B), but simultaneously also comparable to the lifetimes measured for the polymeric $(CuBr)_5$

complexes. Both originate from a ligand-to-metal charge transfer mechanism from the thiolate to the metal ion, in this case $Cu^{+}$, bridged by either Sn or Br. A bi-exponential fit was needed in order to properly fit the data, showing that the lifetime of the excited state consists of both radiative and non-radiative recombination. The measured lifetimes were 7.8 and 1.8 µs respectively. Furthermore, an excitation spectrum was recorded and it was shown that the photoluminescence at 623 nm originates from the Cu-Br-thiolate complexes with an absorption peak at 375 nm (Figure 3.15A), since the excitation and absorption spectra are consistent with each other.

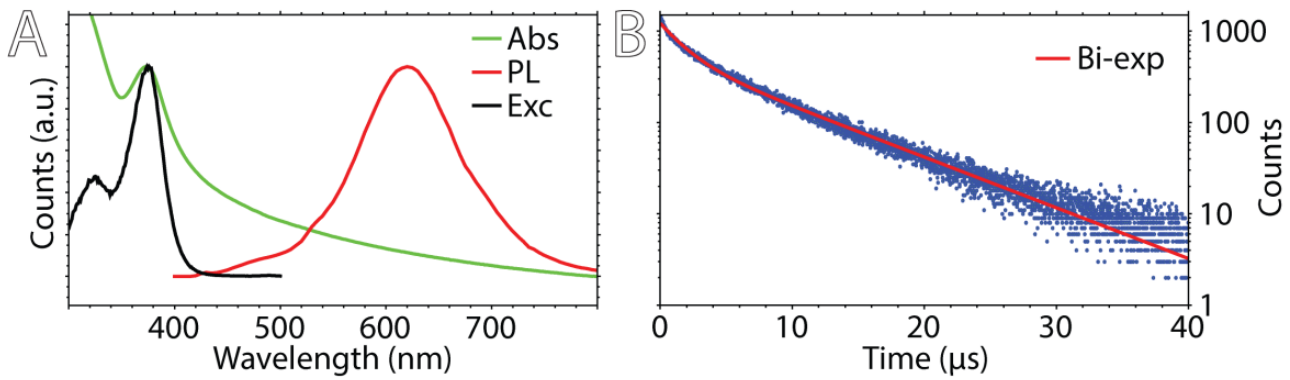


**Figure 3.15: (A) UV/Vis absorption (Abs) as well as photoluminescence (PL) and excitation (Exc) spectra of samples taken after 1 minute. (B) Excited state lifetime spectrum showed with a bi exponential fit of 7.8 and 1.8 µs.**

Presumably because of the nature of these complexes and the columnar phase that is stabilized, these Cu-Br-thiolate complexes lead to well-defined two-dimensional nanosheets after the Cu-S bonds within the Cu-thiolate start to break and the columnar crystal phase shrinks to eventually form $Cu_{1.8}S$ nanosheets. This also explains why the Br remains in the crystals, since without the Br being present the whole columnar phase collapses and one is left with bare anisotropic Cu-thiolate complexes, yielding spherical $Cu_{2-x}S$ nanocrystals.[27] Therefore, we propose a mechanism where at first the columns are stabilized by bridging Br-atoms, but when eventually the crystal starts to form, thiolates have to leave as well as Br trapped within the columns. The outer layer on the other hand, is stabilized by the bridging Br-ions, explaining why Br is still present in the final NSs. The advantage of using $SnBr_4$ over other Br containing species is that Br is easily accessible in $SnBr_4$ due to the weak bond and the fact that $SnBr_4$ is a solution and therefore dissolves very well in many solvents.

A schematic representation for the formation of the final ultrathin $Cu_{1.8}S$ NSs was developed according to the results described above and can be seen in Figure 3.16. The Cu-thiolates form a columnar phase from ~150-200 $^{0}$C (as described by Martin-Alvarez *et al.*)[25], but fall apart into an isotropic phase at elevated temperatures. Because the Cu-thiolate disks are no longer in close vicinity to each other, spherical particles, as discussed in Figure 3.1A, are formed. The addition of Br-atoms stabilize the columnar Cu-thiolate phase above the temperature needed for the formation of the $Cu_{2-x}S$ NCs (>200 $^{0}$C). The halide stabilized columnar phase therefor acts as a 2D constraining templates, leading to the formation of the ultrathin NSs. The formation mechanism as well as a schematic representation of the final termination of the NSs can be seen in Figure 3.16.

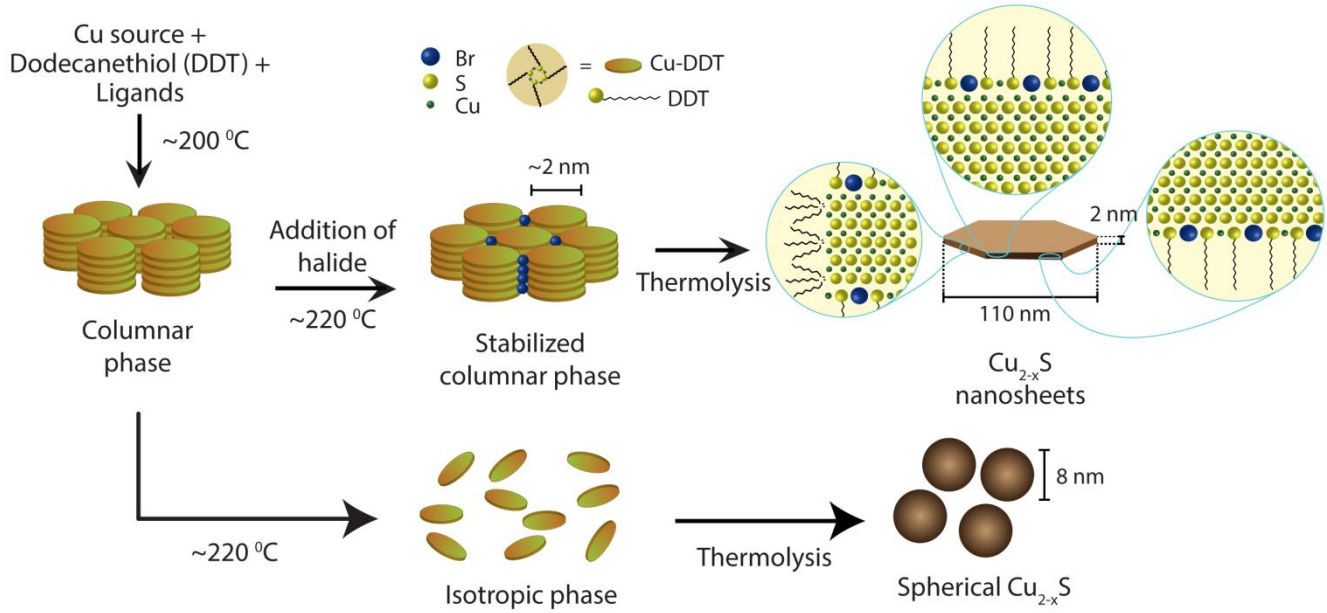


**Figure 3.16: Schematic representation of the proposed reaction mechanism, where Br-ions stabilize columnar stacked Cu-thiolate complexes.**

### 3.3.7. PbS, CdS, and ZnS NSs via cation exchange

PbS, CdS, and ZnS NSs were obtained by cation exchange on the $Cu_{1.8x}S$ NSs with the method described in section 3.2.3. This low temperature method was used due to the fragile nature of the $Cu_{1.8}S$ NSs, since elevated temperatures destroyed the nanosheets as shown in Figure A3.7A. TEM analysis showed preservation of the size and shape of the exchanged NSs compared to the parent NSs as shown in Figure 3.17. It must be noted that the PbS and CdS NSs maintained their size and shape but seemed porous as shown in Figure A3.7B. This could also be related to the NSs being very beam-sensitive, which can also lead to burning and melting of the nanosheets.

EDS analysis showed a conversion of the $Cu_{1.8}S$ NSs to PBS, ZnS and CdS as indicated in Table 3.1. From these measurements it could be concluded that the CE is in fact a near full CE, since there was still $Cu^+$ present. For CdS and PbS, the $Cu^+$ impurities were always in the range between 3% and 6%. In the case of the CE towards ZnS the $Cu^+$ impurities remained as high as 30%, indicating a partial cation exchange. Allowing the CE for one week showed no decrease in the $Cu^+$ impurities. Furthermore, there is noted that the Br ions were not (completely) removed after the CE. For the PbS and ZnS, the Br concentration dropped from 23% to 14% and 11%, respectively. The Br concentration in the CdS NSs dropped to 3% indicating hardly any Br left in the NSs. Where this discrepancy originates from is unclear, but it is clear that the bromides are strongly bound within the NSs and thus confirms the vital role of the halides which stabilize the growth of the lamellar Cu-thiolate complexes.

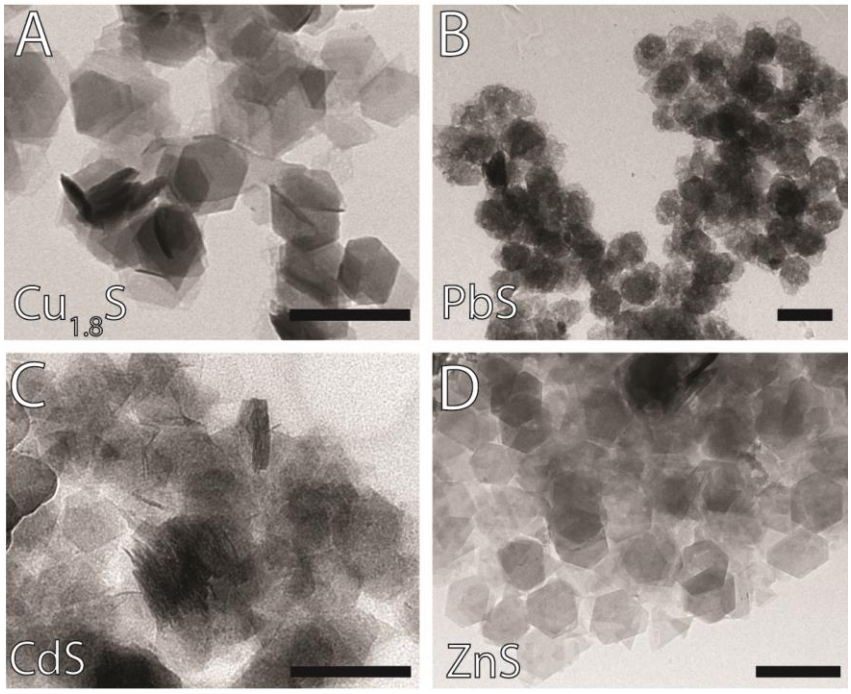


**Figure 3.17: TEM images of synthesized (A) $Cu_{2-x}S$ (parent particles), (B) PbS, (C) CdS and (D) ZnS NSs. Scale bars correspond to 200 nm.**

**Table 3.1: Measured ratios for M:S:Cu:Br (with M=Cd, Pb or Zn).**

| Main composition | EDS ratio M:S:Cu:Br, with M=Cd, Pb and Zn |
|---|---|
| $Cu_{1.8}S$ | -----:1.00:1.79:0.23 |
| CdS | 0.93:1.00:0.06:0.03 |
| PbS | 1.12:1.00:0.03:0.14 |
| ZnS | 0.97:1.00:0.32:0.11 |

The optical properties of the CdS NSs were investigated with absorption, PL and PL excitation spectroscopy (Figure 3.18). The CdS NSs exhibited a strong first excitonic absorption band at 385 nm. The PL spectrum showed a broad (defect) related luminescence centered at ~700 nm with a large Stokes shift of ~300 nm. Such a large Stokes shift was not observed for a direct CdS NSs synthesis.[28] This broad defect related PL could originate from surface defects created after the CE or by Cu and/or Br-atoms traps. The origin of this luminescence was not further investigated, but the excitation spectrum showed that the photoluminescence at 700 nm originates from CdS nanosheets with an absorption peak at 385 nm. When the absorption peak position is compared to what has been observed for CdS two-dimensional nanosheets by Ithurria *et al.*[29], a thickness of 6 monolayers was estimated, which is in agreement with the previously shown results in section 3.3.1.

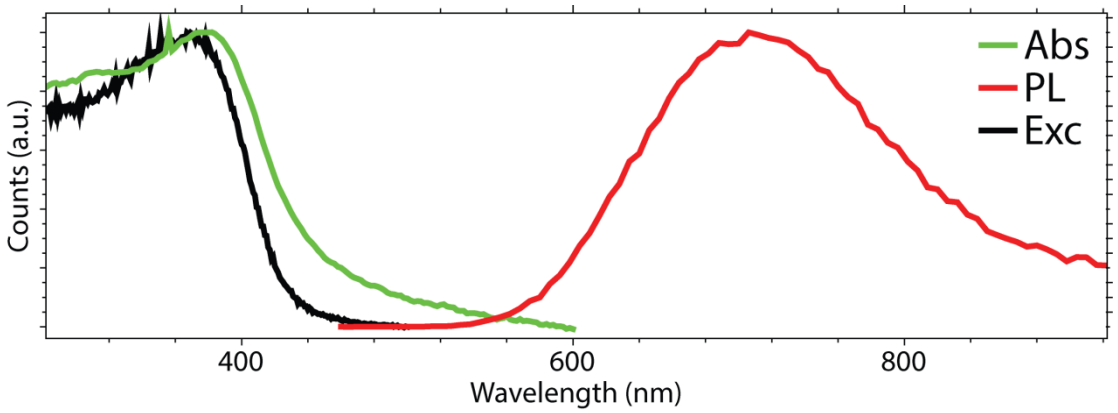


**Figure 3.18: Absorption, PL and PL excitation spectra obtained from the CdS NSs.**

## 3.4. Conclusions

In this chapter, a synthesis method to obtain ultrathin two-dimensional $Cu_{1.8}S$ NSs is described. High control over the size and in shape in the lateral dimensions, leading to large aspect ratios of up to several micrometers and both hexagonal and triangular NSs, has been obtained. The formation mechanism of the two-dimensional $Cu_{1.8}S$ nanosheets was investigated in close detail and there is found that columnar Cu-thiolate complexes are stabilized by Br-ions. These Cu-Br-thiolate complexes consist of tetranuclear Cu-thiolate disks stabilized by Br-atoms that form *in situ* and act as templating agent for two-dimensional $Cu_{1.8}S$ NSs growth. The digestion of these luminescent precursor complexes and the formation of $Cu_{1.8}S$ NSs was proven by following the reaction overtime with absorption and PL spectroscopy, which showed a decrease of the absorption and PL corresponding to so-called Cu-Br-thiolate complexes and the appearance of a $Cu_{1.8}S$ absorption band. Further measurements have shown that Br-ions are part of the crystal in the form of a Cu-Br-thiolate monolayer and remain in the crystal in the same ratio, even after CE. Finally, the $Cu_{1.8}S$ NSs were exchanged to CdS, PbS and ZnS with preservation of the size and shape of the NSs. The CE reactions confirmed the thickness of the NSs and the stable bonding of the halides within the crystal structure. Altogether, the synthesis of the $Cu_{1.8}S$ NSs combined with the cation exchange reactions opens a novel route towards the fabrication of new two-dimensional structures and their possibly interesting properties and applications.

## 3.5. Outlook

For further understanding of the mechanism of the NSs, Density functional theory calculations are being performed on $Cu_{1.8}S$ digenite crystal structure. The calculations and modelling of the NSs could lead to further understanding of the vital role of the halides and their stabilization. For instance, an understanding of the shape control difference between the bromides leading to hexagonal NSs and the halides leading to triangular NSs could be obtained.

Since the size and shape control is only within the lateral dimensions, the control over the thickness should be further explored. The TEM images of the syntheses with different growth temperatures (section 3.3.2) indicated what could be a change in thickness but so far the XRD measurements were inconclusive. Further investigation into the growth temperature or injection temperature (and gradient of heating) could lead to control over the thickness, which lacking in the current synthesis method developed in this thesis.

Although the cation exchange reactions worked and were confirmed with EDS, it does require further investigation, for instance by determining the crystal structure with XRD. As mentioned earlier, it is not clear why certain samples suffered greatly form degradation after the CE reactions. Furthermore, only the optical properties of the CdS NSs were investigated in detail where those of PbS and ZnS were not. Moreover, understanding the case of ZnS, where always a percentage of up to 30% of residual $Cu^{+}$ was left within the NSs should be further investigated.

Finally, it should be investigated whether this mechanism is applicable for other metal sulfides since it is known for a wide variety of metals to form stable lamellar metal-thiolate complexes.[30–33] If this synthesis could be generalized for metal sulfides (or even selenides, as described in chapter 5) it could led to a very versatile tool for synthesizing ultrathin colloidal semiconductors.

## References


1. W. Li; A. Shavel; R. Guzman; J. Rubio-Garcia; C. Flox; J. Fan; D. Cadavid; M. Ibáñez; J. Arbiol; J. R. Morante; A. Cabot. Morphology Evolution of Cu(2-x)S Nanoparticles: From Spheres to Dodecahedrons. Chem. Commun. (Camb). 2011, 47, 10332–10334.

2. H. Shen; H. Wang; H. Yuan; L. Ma; L. S. Li. Size-, Shape-, and Assembly-Controlled Synthesis of Cu2–xSe Nanocrystals via a Non-Injection Phosphine-Free Colloidal Method. CrystEngComm 2012, 14, 555–560.

3. Y.-B. Chen; L. Chen; L.-M. Wu. The Structure-Controlling Solventless Synthesis and Optical Properties of Uniform Cu2S Nanodisks. Chemistry 2008, 14, 11069–11075.

4. Y. Zhao; H. Pan; Y. Lou; X. Qiu; J. Zhu; C. Burda. Plasmonic Cu(2-x)S Nanocrystals: Optical and Structural Properties of Copper-Deficient copper(I) Sulfides. J. Am. Chem. Soc. 2009, 131, 4253–4261.

5. B. Jia; M. Qin; X. Jiang; Z. Zhang; L. Zhang; Y. Liu; X. Qu. Synthesis, Characterization, Shape Evolution, and Optical Properties of Copper Sulfide Hexagonal Bifrustum Nanocrystals. J. Nanoparticle Res. 2013, 15, 1469.

6. Y. Wang; Y. Hu; Q. Zhang; J. Ge; Z. Lu; Y. Hou; Y. Yin. One-Pot Synthesis and Optical Property of copper(I) Sulfide Nanodisks. Inorg. Chem. 2010, 49, 6601–6608.

7. J. B. Rivest; P. K. Jain. Cation Exchange on the Nanoscale: An Emerging Technique for New Material Synthesis, Device Fabrication, and Chemical Sensing. Chem. Soc. Rev. 2013, 42, 89–96.

8. H. Li; M. Zanella; A. Genovese; M. Povia; A. Falqui; C. Giannini; L. Manna. Sequential Cation Exchange in Nanocrystals: Preservation of Crystal Phase and Formation of Metastable Phases. Nano Lett. 2011, 11, 4964–4970.

9. J. M. Luther; H. Zheng; B. Sadtler; a P. Alivisatos. Synthesis of PbS Nanorods and Other Ionic Nanocrystals of Complex Morphology by Sequential Cation Exchange Reactions. J. Am. Chem. Soc. 2009, 131, 16851–16857.

10. B. Sadtler; D. O. Demchenko; H. Zheng; S. M. Hughes; M. G. Merkle; U. Dahmen; L.-W. Wang; a P. Alivisatos. Selective Facet Reactivity during Cation Exchange in Cadmium Sulfide Nanorods. J. Am. Chem. Soc. 2009, 131, 5285–5293.

11. S. Oriol; L. Dominik; K. Metin; R. Aleksandra; K. Andras. Ultrasensitive Photodetectors Based on Monolayer MoS2. Nat. Nanotechnol. 2013, 8, 497–501.

12. B. Radisavljevic; a Radenovic; J. Brivio; V. Giacometti; a Kis. Single-Layer MoS2 Transistors. Nat. Nanotechnol. 2011, 6, 147–50.

13. Q. H. Wang; K. Kalantar-Zadeh; A. Kis; J. N. Coleman; M. S. Strano. Electronics and Optoelectronics of Two-Dimensional Transition Metal Dichalcogenides. Nat. Nanotechnol. 2012, 7, 699–712.

14. S. Ithurria; M. D. Tessier; B. Mahler; R. P. S. M. Lobo; B. Dubertret; A. L. Efros. Colloidal Nanoplatelets with Two-Dimensional Electronic Structure. Nat. Mater. 2011, 10, 936–941.

15. C. Schliehe; B. H. Juarez; M. Pelletier; S. Jander; D. Greshnykh; M. Nagel; A. Meyer; S. Foerster; A. Kornowski; C. Klinke; H. Weller. Ultrathin PbS Sheets by Two-Dimensional Oriented Attachment. Science 2010, 329, 550–553.

16. W. Shi; J. Zhu; X. Rui; X. Cao; C. Chen; H. Zhang; H. H. Hng; Q. Yan. Controlled Synthesis of Carbon-Coated Cobalt Sulfide Nanostructures in Oil Phase with Enhanced Li Storage Performances. ACS Appl. Mater. Interfaces 2012, doi:10.1021/am3003654

17. S. Pedetti; B. Nadal; E. Lhuillier; B. Mahler; C. Bouet; B. Abe; X. Xu; B. Dubertret. Optimized Synthesis of CdTe Nanoplatelets and Photoresponse of CdTe Nanoplatelets Films. Chem. Mater. 2013, 25, 2455–2462.

18. S. Ithurria; B. Dubertret. Quasi 2D Colloidal CdSe Platelets with Thicknesses Controlled at the Atomic Level. J. Am. Chem. Soc. 2008, 130, 16504–16505.

19. K. H. Park; K. Jang; S. U. Son. Synthesis, Optical Properties, and Self-Assembly of Ultrathin Hexagonal In2S3 Nanoplates. Angew. Chem. Int. Ed. Engl. 2006, 45, 4608–12.

20. D. D. V. Ii; S. In; R. E. Schaak; V. E. T. Al. A Precursor-Limited Nanoparticle Coalescence Pathway for Tuning the Thickness of Laterally-Uniform Colloidal Nanosheets : The Case of SnSe. ACS Nano 2011, 8852–8860.

21. J. M. Luther; P. K. Jain; T. Ewers; a P. Alivisatos. Localized Surface Plasmon Resonances Arising from Free Carriers in Doped Quantum Dots. Nat. Mater. 2011, 10, 361–366.

22. E. Groeneveld; L. Witteman; M. Lefferts; X. Ke; S. Bals; G. Van Tendeloo; C. de Mello Donega. Tailoring ZnSe-CdSe Colloidal Quantum Dots via Cation Exchange: From Core/Shell to Alloy Nanocrystals. ACS Nano 2013, 7, 7913–7930.

23. Y. Wang; A. Tang; K. Li; C. Yang; M. Wang; H. Ye; Y. Hou; F. Teng. Shape-Controlled Synthesis of PbS Nanocrystals via a Simple One-Step Process. Langmuir 2012, 28, 16436–16443.

24. A. E. Martell. Hard and Soft Acid-Base Behavior in Aqueous Solution: Steric Effects Make Some Metal Ions Hard: A Quantitative Scale of Hardness-Softness for Acids and Bases. J. Chem. Educ. 1996, 73, 654–661.

25. P. Espinet; M. C. Lequerica. Synthesis , Structural Characterization and Mesogenic Behavior of Copper(i) N-Alkylthiolates. Chem. Eur. J 1999, 5, 1982–1986.

26. A. Lapprand; A. Bonnot; M. Knorr; Y. Rousselin; M. M. Kubicki; D. Fortin; P. D. Harvey. Formation of an Unprecedented (CuBr)5 Cluster and a Zeolite-Type 2D-Coordination Polymer: A Surprising Halide Effect. Chem. Commun. (Camb). 2013, 49, 8848–8850.

27. T. Kuzuya; Y. Tai; S. Yamamuro; K. Sumiyama. Synthesis of Copper and Zinc Sulfide Nanocrystals via Thermolysis of the Polymetallic Thiolate Cage. Sci. Technol. Adv. Mater. 2005, 6, 84–90.

28. J. S. Son; K. Park; S. G. Kwon; J. Yang; M. K. Choi; J. Kim; J. H. Yu; J. Joo; T. Hyeon. Dimension-Controlled Synthesis of CdS Nanocrystals: From 0D Quantum Dots to 2D Nanoplates. Small 2012, 8, 2394–2402.

29. X. Li; M. Wang; H. Shen; Y. Zhang; H. Wang; L. S. Li. Inorganic Sn-X-Complex-Induced 1D, 2D, and 3D Copper Sulfide Superstructures from Anisotropic Hexagonal Nanoplate Building Blocks. Chem. Eur. J 2011, 17, 10357–10364.

30. Z. Zhuang; X. Lu; Q. Peng; Y. Li. A Facile “Dispersion-Decomposition” Route to Metal Sulfide Nanocrystals. Chemistry 2011, 17, 10445–52.

31. Y. Chui; K.-H. Low; J. Lu; V. a L. Roy; S. L.-F. Chan; C.-M. Che. Homoleptic platinum(II) and palladium(II) Organothiolates and Phenylselenolates: Solvothermal Synthesis, Structural Determination, Optical Properties, and Single-Source Precursors for PdSe and PdS Nanocrystals. Chem. Asian J. 2010, 5, 2062–2074.

32. Y. X. Zhang; H. C. Zeng. Gold(I)“Alkanethiolate Nanotubes. Adv. Mater. 2009, 21, 4962–4965.

33. M. F. Calderón; E. Zelaya; G. a Benitez; P. L. Schilardi; A. H. Creus; A. G. Orive; R. C. Salvarezza; F. J. Ibañez. New Findings for the Composition and Structure of Ni Nanoparticles Protected with Organomercaptan Molecules. Langmuir 2013, 29, 4670–4678.

# 4. Synthesis of other $Cu_{2-x}S$ NC morphologies

## 4.1. Introduction

While the previous chapter was devoted to the synthesis of ultrathin $Cu_{1.8}S$ nanosheets, this chapter will focus on the synthesis of larger, three-dimensional anisotropic $Cu_{2-x}S$ NCs and converting these into other metal sulfide NCs by using cation exchange (CE). The synthesis of large anisotropic NCs has been thoroughly investigated, leading to a plethora of different sized and shaped $Cu_{2-x}S$ NCs.[1–3] On the other hand, CE reactions on these larger NCs have not been widely investigated.

This chapter will describe several different synthesis methods for large $Cu_{2-x}S$ NCs, namely isotropic quasi-spherical NCs and anisotropic hexagonal bipyramids (BP) and bifrustums (BF). The presented NCs in this chapter are generally in the order of ~10-40 nm and therefore can be considerd to be 'large'. As mentioned earlier, CE reactions are considered to be a useful tool for the synthesis of NCs with a crystal structure or shape which are not attainable in a direct synthesis.[4] The CE reactions discussed in this chapter, for example, resulted in the synthesis of metastable crystal structures, such as wurtzite ZnS as well as hexagonal shaped rocksalt PbS NCs. The synthesized NCs in this chapter will be used as building blocks for self-assembled structures, as further described in chapter 6.

This chapter is divided as follows. After the experimental section (section 4.2), containing the materials and the different used synthesis methods, section 4.3 will give the main results for this chapter as well as a discussion. This chapter will be ended with conclusions (section 4.4) and a brief outlook (section 4.5).

## 4.2. Experimental

In this section the used materials (section 4.2.1), the three different methods used to synthesize large anisotropic $Cu_{2-x}S$ NCs (sections 4.2.2-4.2.4) and the method used for the CE (section 4.2.5) will be presented. Sections 4.2.6-4.2.8 will give further details on the used equipment including the syntheses set-ups, electron microscopes and the x-ray diffractometer.

### 4.2.1. Materials

Copper(I) acetate (CuOAc, 97%), Tin(IV) tetrabromide ($SnBr_4$, 99%), Zinc(II) dichloride ($ZnCl_2$, 98+%), Copper(I) chloride (CuCl, 97%) and Copper(II) dichloride dihydride ($CuCl_2{\cdot}2H_2O$, 97%) were purchased from Sigma Aldrich and used without further purification. Other metal salts used for the cation exchange experiments were also bought from Sigma Aldrich, such as Tin(II) dichloride ($SnCl_2$), Tin(IV) acetate ($SnOAc_4$), Lead(II) acetate trihydrate ($PbOAc_2{\cdot}3H_2O$, 99.999% trace metals basis), Cadmium(II) nitrate tetrahydrate ($Cd(NO_3)_2{\cdot}4H_2O$, 98%) and were used without further purification. 1-dodecanethiol (DDT) and tributyldisulfide

(TBDS), 1-octadecene (ODE, 90%), trioctylphosphine oxide (TOPO, 99%), oleylamine (OLAM, 90%), trioctylphosphine (TOP, 90%), tributylphosphine (TBP, 99%), anhydrous toluene, methanol and butanol were purchased from Sigma Aldrich as well. ODE, TOPO and OLAM needed to be degassed prior to synthesis.

### 4.2.2. $Cu_{2-x}S$ large quasi-spherical NCs

The first described synthesis method, yielding large quasi-spherical $Cu_{2-x}S$ NCs, is an adaption from Wang *et al.*[2] Here, 0.3 mmol CuOAc and 1.1 g TOPO were dissolved in 25 ml degassed ODE. After degassing for one hour at 100 $^0$C, the reaction was heated to 160 $^0$C and 1 ml DDT was swiftly injected into the dark green solution under nitrogen conditions. After 3.5 hours, a solution containing 0.15 mmol $SnBr_4$ dissolved in 4.8 ml DDT and 1.2 ml OLAM, was swiftly injected and the temperature was further increased to 220 $^0$C for one hour. The final turbid brown solution was quickly cooled by using a water bath. The NCs were washed by adding methanol/butanol solution as anti-solvent, followed by centrifugation and redispersion in toluene. This cycle was repeated 3 times.

### 4.2.3. $Cu_{1.96}S$ Hexagonal bipyramids

The second method, an adaptation of the work by Norako *et al.*[5] and Kuzuya *et al.*[6], was used to synthesize hexagonal bipyramid NCs of up to ~40 nm. Both the synthesis method as the synthesized NCs described in this section were provided by Ward v. d. Stam. Typically, 1.0 mmol CuCl and 0.5 mmol $SnBr_4$ were mixed in 8 mL DDT and 2 mL OLAM and gradually heated to 225 $^0$C. At first, a turbid white suspension was obtained at RT. The solution turned turbid yellow around 80 ˚C, and clear yellow at 130 $^0$C. When the temperature reached 225 $^0$C, the solution turned brown/black, indicating the formation and growth of $Cu_{1.96}S$ NCs. The solution was maintained at this temperature for one hour. Finally, the nanoparticles were washed by adding methanol/butanol solution as anti-solvent, followed by centrifugation and redispersion in toluene. This cycle was repeated 3 times.

### 4.2.4. $Cu_{1.96}S$ Hexagonal bifrustums

The synthesis for the $Cu_{1.96}S$ hexagonal bifrustums is based on the work by Li *et al.*[3] In a typical synthesis, 8 mmol of $CuCl_2{\cdot}2H_2O$ and 12 g OLAM were heated to 200 $^0$C under nitrogen flow. After one hour the clear dark brown solution was cooled to 180 $^0$C and 2 mL TBDS (10 mmol) was swiftly injected. The solution was re-heated to 200 $^0$C and after 40 minutes of growth the reaction mixture was cooled. Subsequently, the NCs were washed three times with a methanol/butanol solution as anti-solvent, and redispersed in toluene. This cycle was repeated 3 times.

### 4.2.5. ZnS, PbS and CdS hexagonal bipyramids and frustums via cation exchange

This method was first described by Li *et al.*[7] First, 1 mmol $ZnCl_2$ was dissolved in 3 mL 1-octadecene and 2 mL OLAM (both previously degassed) at 250 $^0$C. Subsequently, $Cu_{2-x}S$ NCs dispersed in trioctylphosphine (TOP) were injected at that temperature. The mixture was allowed to react for 5 minutes under heating and stirring, after which the temperature was lowered to 70 $^0$C, followed by the addition of several mL´s toluene. The final sample was precipitated by adding a methanol/butanol solution. The NCs were isolated by centrifugation and redispersed in toluene. This cycle was repeated twice.

### 4.2.6. Synthesis set-up

For the hot-injection syntheses, the following set-up was used; a 50 ml 3-neck-roundbottomflask containing a magnetic stirring bean was fitted with two septa (one for the thermocouple and the other for the hot injection) and a Vigreux condenser. The Vigreux condenser was connected to a Schlenkline with a 2.5 torr vacuum and a 40 $L_n$/h nitrogen pressure. The heating source was a Horst HTMC1/69 thermocouple set at step 2 and was changed to step 1 20 $^0$C below the final growth temperature to prevent the temperature from rising too high. A VWR hotplate/stirrer was used for stirring and was set at 600 rpm. Samples were taken with a 20 mL glass syringe with an iron needle and stored in glass vials with a septum. These vials were prepared within a glove box to keep the samples oxygen free. The cation exchange reactions were performed in 20 ml glass vials in an aluminum block placed on an A VWR hotplate/stirrer. The CE reactions were performed within a glovebox.

### 4.2.7. Electron microscopy

For the transmission electron microscopy (TEM) measurements, a standard FEI Tecnai-10 or FEI Tecnai-12 was used. The energy dispersive x-ray spectroscopy (EDS) and scanning electron microscopy (SEM) measurements were conducted with a FEI Tecnai-20F equipped with a Field Emission Gun, a Gatan 694 CCD camera and an EDA spectrometer. The microscope was operated at 200 kV. Acquisition time for the EDS measurements was 30 s. Samples were prepared on carbon coated polymer film copper grids (300 mesh) in a glove box by dropcasting 10-50 µl (depending on the dilution) of sample on the grids.

### 4.2.8. X-ray diffractometry

For the X-ray diffractometry, a Philips PW1729 x-ray generator and PW 3710 MBP controller were used at 40 kV and 20 mA and with a Cu $K_\alpha$ source ($\lambda$=1.5418 Å). Samples were prepared by dropcasting a concentrated NCs solution on a Si wafer. The concentrated NCs solution was prepared as follows. 1 mL of sample was sedimented with a methanol/butanol solution at 3000 rpm for 15 minutes and redispersed in a few drops of chloroform. The chloroform dispersion was dropcasted on a small piece of Si wafer and the chloroform was evaporated. The small

piece of wafer was taped on an aluminum holder. Multiply measurements (5-15 measurement, depending on the quality) were conducted to increase the signal to noise ratio.

## 4.3. Results and discussion

### 4.3.1. $Cu_{2-x}S$ large quasi-spherical NCs

When the synthesis as described above (section 4.2.2) was carried out until just before the second injection, small (4.8 nm) quasi-spherical $Cu_{2-x}S$ NCs were obtained (Figure 4.1A), as was described by Wang *et al.*[2] To allow these $Cu_{2-x}S$ seeds to grow *in situ*, a second solution containing OLAM, DDT and $SnBr_4$, was injected. After the second injection and by increasing the growth temperature to 220 $^0$C, the solution turned from clear brown to turbid brown within the first 10 minutes, indicating the rapid growth of the $Cu_{2-x}S$ seeds. After 30 min, (Figure 4.1B), the $Cu_{2-x}S$ seeds had grown to 8.4 nm. Additional growth of 30 minutes resulted in large quasi-spherical NCs of 10.9 nm (Figure 4.1C), which corresponds to a 11.7 times volume increase compared to the 4.8 nm seeds. EDS analysis indicated a Cu:S:Sn ratio of 1.94:1.00:0.07 after the second injection, confirming that the large quasi-spherical NCs are indeed $Cu_{2-x}S$. Furthermore, a small amount of Sn is present in the NCs, which will be further discussed later on in this section.

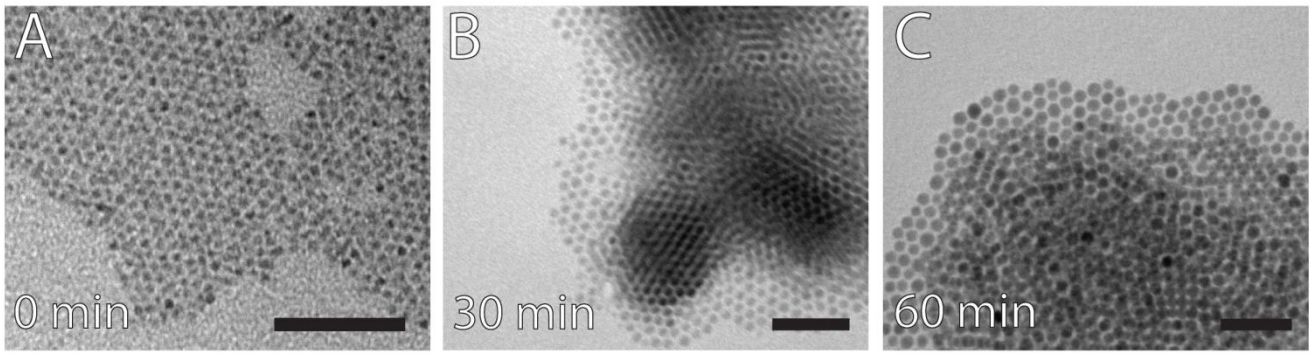


**Figure 4.1: TEM images of the quasi-spherical $Cu_{2-x}S$ NCs (A) before the second injection (4.8 nm), (B) 30 minutes after the second injection (8.4 nm) and (C) 60 minutes after the second injection (10.9 nm). Scale bars correspond to 50 nm.**

As the second injection did not introduce any new Cu precursors, the growth could only either come from Ostwald ripening, or from unused Cu precursors within the reaction mixture. The high monodispersity indicates that growth from unused precursors is more likely. As mentioned earlier for the $Cu_{1.8}S$ sheets, the active copper precursors are Cu-thiolate complexes rather than the added CuOAc. Since these Cu-thiolate complexes can be stable up to 200 $^0$C, and the growth of the seeds is at 180 $^0$C, it could be that after 3.5 hours of growth, an equilibrium is reached, where part of the $Cu^+$ is in the NCs and the other part is left behind in the Cu-thiolate complexes as described in the previous chapter.[8] This leads to unused Cu-precursors within the reaction mixture which can be consumed by a second injection chalcogenide precursor, yielding the larger quasi-spherical $Cu_{2-x}S$ NCs. Due to time limitations, the nature of these unused Cu-precursors were not further investigated.

To further investigate the role of the added $SnBr_4$, two control experiments were conducted. When the second injection was carried out in the absence of $SnBr_4$, both with DDT and OLAM (Figure 4.2A) and solely with DDT (Figure 4.2B), thick platelets were obtained. These thick platelets are also obtained without a second injection at elevated temperatures (220 $^0$) and therefore confirm the active role of $SnBr_4$ in controlling the size and shape of the quasi-spherical NCs. As mentioned in the previous chapter, the addition of $SnBr_4$ to a $Cu_{1.8}S$ NSs synthesis leds to a huge change in size and shape of the final NCs by the stabilization of the Cu-thiolate complexes by halide ions. EDS analyses detected no bromide for the quasi-spherical NCs but rather only Sn, which indicates a different mechanism compared to the NSs. From literature, it is know that Sn can be used to form inorganic ligands which can strongly influence to surface properties of NCs.[9–11] As Kovalenko *et al.* proposed, these inorganic ligands are formed as charged metal chalcogenides.[11] Since no bromide was measured with the EDS analysis, we propose that after the second injection containing $SnBr_4$, Sn(IV)-complexes are formed *in situ*, comparable to $SnS_4^{4-}$ species shown by Kovalenko *et al.*, which subsequently bind to certain facets of the $Cu_{2-x}S$ seeds and therefore control the growth of the seeds into larger quasi-spherical NCs.[11]

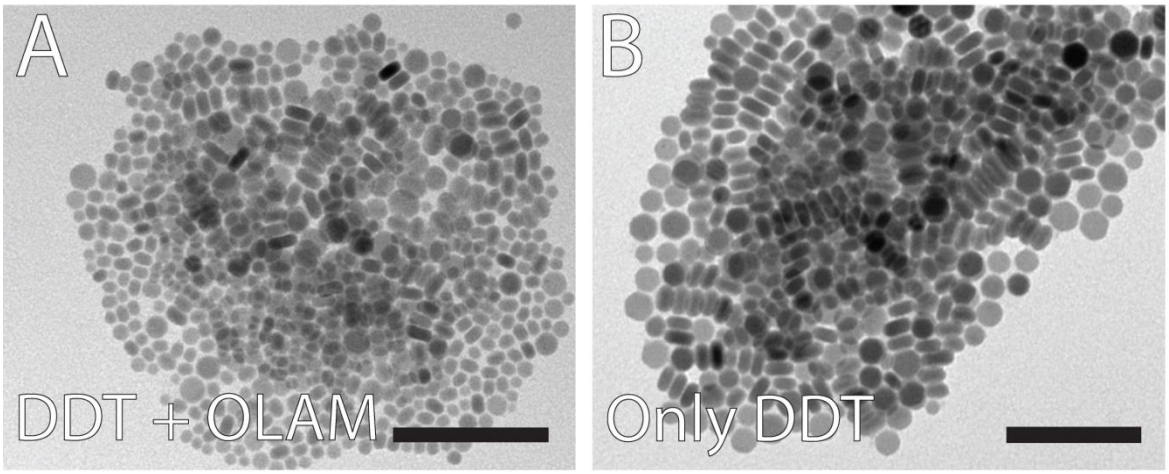


**Figure 4.2: TEM images of $Cu_{2-X}S$ platelets obtained with the double injection method when (A) DDT and OLAM or (B) using solely DDT was used for the second injection. Scale bars correspond to 100 nm.**

### 4.3.2. $Cu_{1.96}S$ Hexagonal bipyramids

The synthesis as described in section 4.2.3 yielded truncated hexagonal BPs as shown in Figure 4.3. Although the hexagonal structure is not visible from the TEM images, scanning electron microscopy (SEM) revealed the hexagonal base and the twelve trapezoidal facets, as shown in Figure 4.3C. Furthermore, SEM measurements showed no preferred orientation of the NCs to the TEM grid. The BPs are ~38 nm in length and ~28 nm in width. XRD analysis showed a djurleite $Cu_{1.96}S$ crystal structure, as shown later on in Figure A4.7. As with the large quasi-spherical NCs obtained with the double injection method, the final size and shape of these crystals is controlled by the addition of Sn(IV)-complexes. The exact formation of these NCs will not be further discussed

in this thesis. The $Cu_{1.96}S$ hexagonal BPs were used to synthesis ZnS hexagonal BPs (section 4.3.4), which were further used as building blocks for micrometer scaled two-dimensional superstructures (Chapter 6).

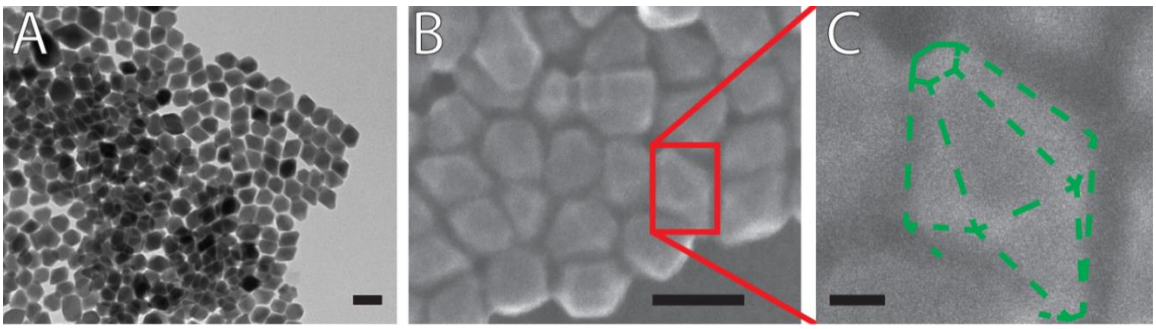


**Figure 4.3: TEM (A) and SEM (B+C) images showing the hexagonal bipyramidal $Cu_{1.96}S$ NCs synthesized by Ward v. d. Stam. Panel (C) shows a zoom in of (B). Scale bars in (A) and (B) correspond to 50 nm. Scale bar in (C) corresponds to 10 nm.**

### 4.3.3. $Cu_{1.96}S$ Hexagonal bifrustums

As described by Li *et al.*, the synthesis as depicted in section 4.2.4 should results in hexagonal BP $Cu_{2-x}S$ NCs.[3] When this procedure was followed, highly monodisperse hexagonal BFs (in the article wrongly named as Tetradecahedron) were synthesized (Figure 4.4). These BFs are ~33 nm in both width and length and XRD showed, similar to the hexagonal bipyramids, a djurleite $Cu_{1.96}S$ crystal structure (shown later on in Figure 4.7). TEM measurements only revealed hexagonal NCs (Figure 4.4A), which also could be hexagonal platelets. SEM was used to determine the three-dimensional shape as shown in Figure 4.4B-D. Here, the twelve trapezoidal and two hexagonal facets belonging to the hexagonal BFs can be clearly seen, and thus ruling out the platelet morphology. As with the BPs, the SEM images showed no preferred orientation on the TEM grid. This is further supported by comparing individual NCs with a simple three-dimensional model of a hexagonal bifrustum with roughly the same aspect ratios as the $Cu_{1.96}S$ NCs. Here, it is clear that different orientations of a BF yield a hexagonal two-dimensional projection (Figure 4.4E and A4.1). These BF NCs were further used in CE reactions to obtain ZnS, CdS and PbS NCs, as will be discussed in the following section.

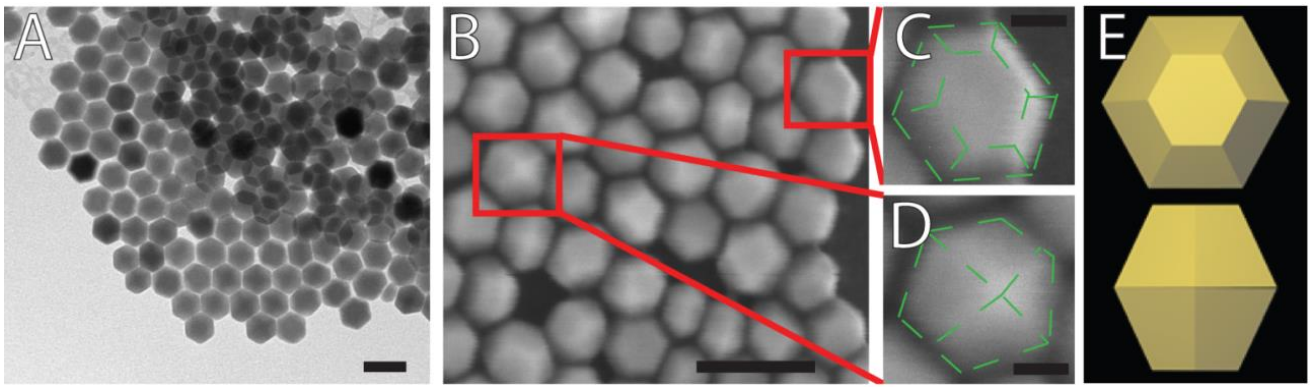


**Figure 4.4: TEM (A) and SEM (b) images showing the hexagonal bifrustum $Cu_{2-X}S$ NCs. Panel (C) and (D) show a zoom in of the BFs indicating the different facets. (E) Two simple three-dimensional models are shown as references. Scale bars in (A) and (B) correspond to 50 nm. Scale bars in (C) and (D) correspond to 10 nm.**

To find the difference between the hexagonal bipyramids obtained in this work and the hexagonal bipyramids obtained by Li *et al.*, several control syntheses were conducted.[3] However, small changes in the growth temperature, the concentrations and the purity of the used chemicals all resulted either in an increase in polydispersity (Figure A4.2) or monodisperse hexagonal platelets (Figure A4.3).

### 4.3.4. ZnS, PbS and CdS hexagonal bipyramids and frustums via cation exchange

For the anisotropic hexagonal $Cu_{1.96}S$ NCs as described in the previous two sections, CE reactions to ZnS NCs were performed according to method described in section 4.2.5. Due to the different absorption properties of $Cu_{1.96}S$ and ZnS, the color of the washed NCs dispersions changed from turbid dark brown to turbid white. In some cases, the dispersion remained slightly brown due to residual $Cu^+$ ions in the ZnS NCs. TEM measurements indicated preservation of the size and shape of the NCs after the CE reaction, as shown in Figure 4.5. For both the BPs and the BFs, TEM measurements revealed a noticeable change in the clustering behavior after the CE, as the ZnS NCs had less attractive interaction and therefore display less three-dimensional clustering. This change in clustering behavior opens up possibilities for the formation of two-dimensional monolayers by self-assembly techniques, since large attractive interactions limit the two-dimensional monolayer formation. The self-assembly of these anisotropic ZnS NCs into two-dimensional monolayers will be further discussed in chapter 6.

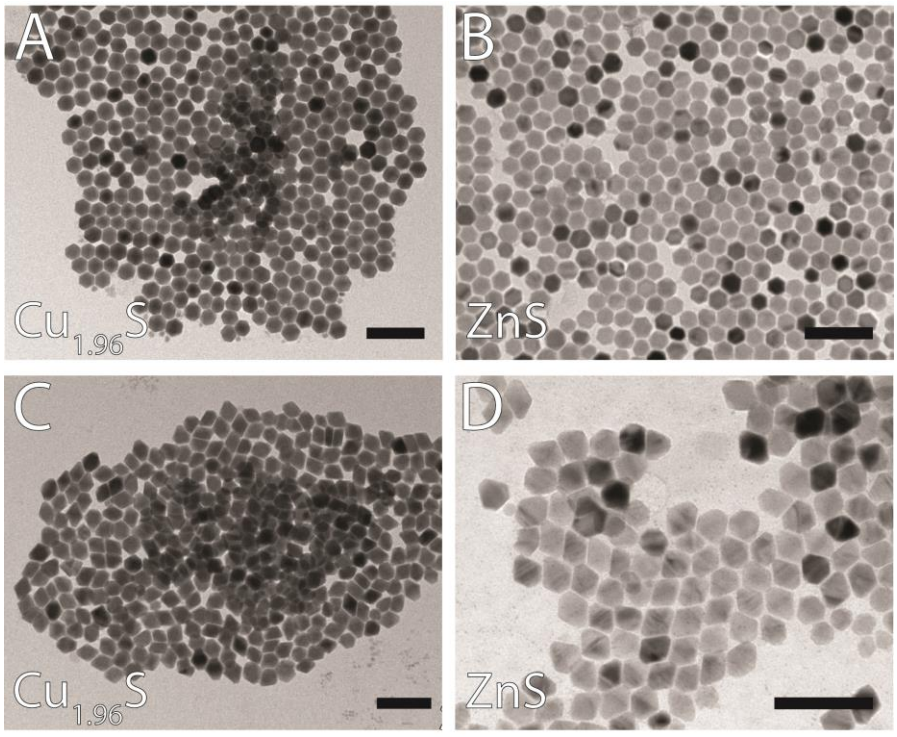


**Figure 4.5: TEM images of the BFs (A) before and (B) after the CE reaction of $Cu^+$ for $Zn^{2+}$. (C) and (D) show the BPs before and after the CE reaction of $Cu^+$ for $Zn^{2+}$. Scale bars correspond to 100 nm.**

Next to hexagonal BFs and BPs, the spherical NCs obtained from the double injection and two samples containing hexagonal $Cu_{2-x}S$ platelets as described in Figure A4.3 were exchanged to ZnS (Figure A4.4). As for the hexagonal $Cu_{1.96}S$ and ZnS NCs described above, the clustering behavior of the NCs changed after the CE. For the platelets, this leads to a decrease of platelet stacks and an increase of platelets lying flat on the TEM grid.

For the synthesis of the CdS and PbS BFs and BPs, the CE method described in section 3.2.3 was used. As with the CE reactions for the CdS NSs, the solutions turned from dark brown to either yellow for CdS or black for PbS during the exchange, but were all turbid due to the large size of the BFs and BPs. TEM measurements showed the preservation of the size and shape of the BFs after the CE (Figure 4.6). In contrast with the CE towards ZnS, the CdS and PbS NCs showed no decrease in clustering behavior. The CdS and PbS NCs did however show interesting self-assembled three-dimensional supercrystals (Figure A4.5). Finally, there should be noted that after the CE towards PbS, the NCs showed an interparticle contrast (Figure A4.6). The origin of these contrasts are unclear and were not further investigated due to time limitations but could be related to the high amounts of residual $Cu^+$ left after the cation exchange (as described in the following section).

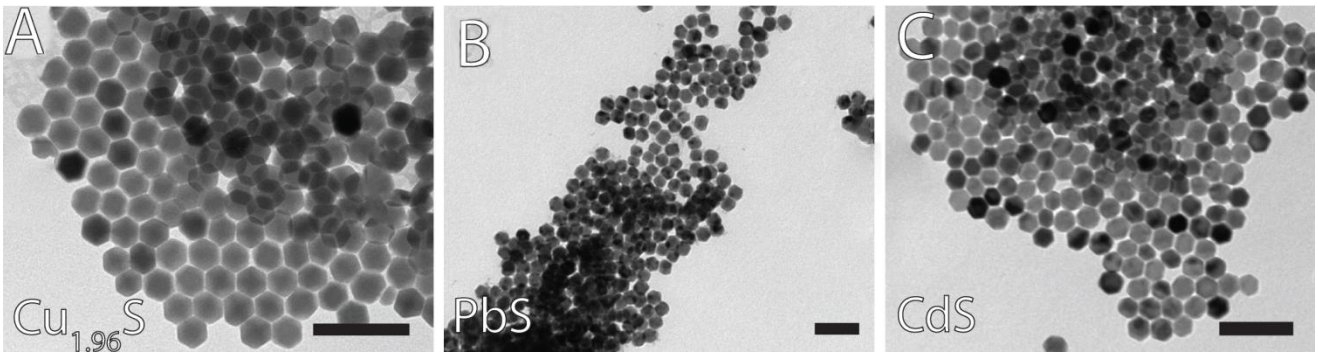


**Figure 4.6: TEM images of the CE reaction of $Cu^+$ for $Cd^{2+}$ and $Pb^{2+}$. (A) $Cu_{1.8}S$ hexagonal bifrustums parent NCs and the (B) PbS and (C) CdS NCs after the CE. Scale bars correspond to 100 nm.**

EDS measurements were performed to investigate the composition of the cation exchanged NCs. These results are shown in Table 4.1. For the ZnS and CdS BFs, less than 5% residual $Cu^+$ was detected and thus indicated a near full exchange. The percentage of $Cu^+$ in PbS could be lowered from 30% to 10% by allowing the CE reaction to proceed over one week. A lower $Cu^+$ content could not be achieved. There is thought that the remaining

**Table 4.1: Measured ratios for M:S:Cu (with M=Cd, Pb or Zn) with EDX on larger hexagonal NCs.**

| Main composition | Shape | Exchange Method | EDX ratio M:S:Cu with M=Cd, Pb and Zn |
|---|---|---|---|
| ZnS | BP | High T | 0.99:1.00:0.05 |
| CdS | BF | Low T | 0.92:1.00:0.03 |
| PbS | BF | Low T | 0.73:1.00:0.30 |
| ZnS | BF | High T | 1.11:1.00:0.01 |

copper ions in the PbS NCs are stabilizing the NCs due to the large crystal mismatch of the thermodynamically stable crystal structure (rock salt Figure 4.7), with the hexagonal shape of the PbS NCs. The residual $Cu^{+}$ ions are thus harder to exchange and are needed for the stability of the PbS NCs. Therefore, a complete exchange of $Cu^{+}$-ions for $Pb^{2+}$-ions would probably lead to the collapse of the highly unstable hexagonal PbS NCs.

XRD analysis was conducted to investigate the crystal structures of the different obtained BFs, as shown in Figure 5.8. The diffractograms show a clear change of crystal structure from the djurleite $Cu_{1.96}S$ to rocksalt PbS and wurtzite ZnS. The CE on the BPs towards ZnS also showed a wurtzite crystal structure as shown in Figure A4.7. As noted earlier, CE reactions can yield NCs with metastable shapes and crystal structures. This is also the case for the obtained ZnS NCs, since hexagonal BP- and BF-shaped metastable wurtzite ZnS NCs are obtained, rather than the thermodynamically stable zinc blende ZnS. The crystal structure of the CdS NCs could not be determined due to the lack of material.

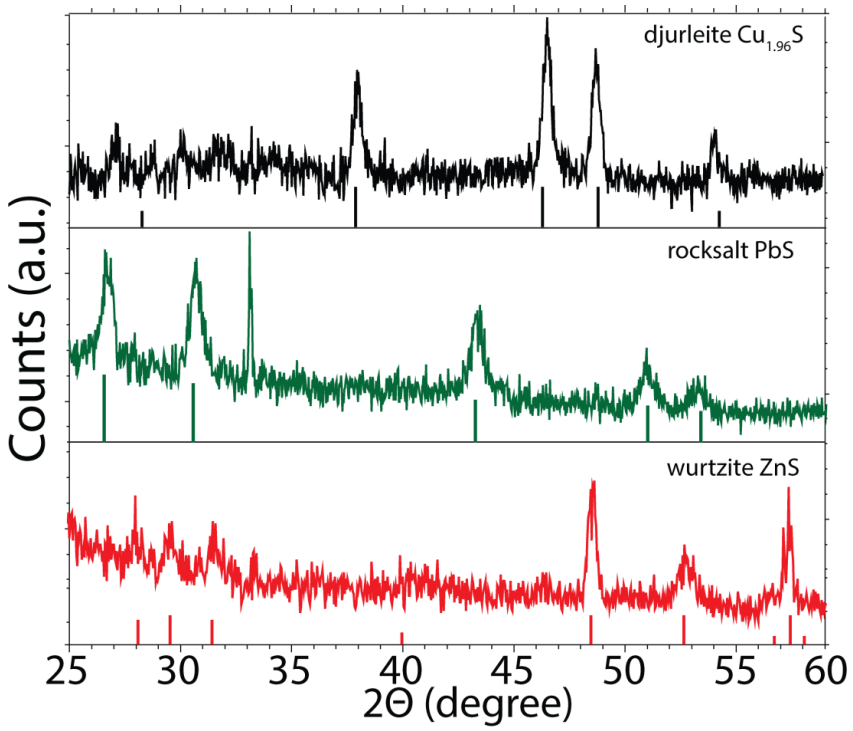


**Figure 4.7: X-ray difractograms of the $Cu_{1.96}S$, ZnS and PbS BFs. Reference bars are from JCPDS card no. [20-0365], [65-0302] and [05-0492] for djurleite $Cu_{1.96}S$, rocksalt PbS and wurtzite ZnS, respectively.**

## 4.4. Conclusions

In this chapter we showed, together with the previous chapter describing the $Cu_{1.8}S$ NSs, the versatility of the size and shape control of $Cu_{2-x}S$ NCs and the accessibility of the $Cu^{+}$ ions for cation exchange reactions. Large (up to 11 nm) quasi-spherical $Cu_{2-x}S$ NCs were synthesized by a new develop method. Here, a second precursor solution containing DDT and $SnBr_4$, was injected into a solution containing *in situ* $Cu_{2-x}S$ dots. Furthermore, large (up to

~40 nm) djurleite, $Cu_{1.96}S$, hexagonal bifrustum and bipyramid NCs were synthesized. The $Cu_{1.96}S$ BFs were successfully converted to ZnS, PbS and CdS BFs via cation exchange reactions. Whereas the ZnS and the CdS CE reactions were near full exchanges (1-3% residual $Cu^+$ ions left), the PbS NCs showed a substantial amount of $Cu^+$ ions which were not exchanged due to their stabilization effect onthe highly unstable hexagonal shaped rocksalt PbS NCs. Furthermore, ZnS BPs were synthesized via cation exchange with only 5% residual $Cu^+$ ions. XRD analysis showed that all the NCs changed in crystal structure. Both for the BFs and BPs, the metastable wurtzite ZnS was synthesized, rather than the stable zinc blende crystal structure. This shows that the NCs after CE are indeed 'trapped' within the shape of the parent crystal and therefore being forced into a metastable crystal structure, which is not attainable with a direct synthesis.

### 4.5. Outlook and ongoing work

As mentioned earlier, the role of $SnBr_4$ as a ligand during synthesis of the large quasi-spherical $Cu_{2-x}S$ NCs and the $Cu_{1.96}S$ has not been investigated thoroughly. An ongoing investigation into these surface controlling Sn(IV) complexes could unravel the mechanism and therefore could lead to an interesting new tool for the size and shape control of NCs. As for the double injection method, further exploration into different seeds could be interesting for instance for the thickness control of the $Cu_{1.8}S$ NSs. Here the amount of DDT (and OLAM) should be precisely tuned for an increase of the thickness. Another adaption for the double injection could be the synthesis of core|shell NCs. This could be achieved by either including other metal ions into the second injection (leading for instance to $Cu_{2-x}S$|ZnS core|shell NCs) or by using a different alkyl chalcogenide (for instance 1-dodecaneselenol, as described in the next chapter) for the second injection (leading to $Cu_{2-x}S$| $Cu_{2-x}Se$ core|shell NCs). This method could for instance be interesting for the synthesis of PbS|PbSe or CdS|CdSe core|shell NCs via CE.

## References


1. Y.-B. Chen; L. Chen; L.-M. Wu. The Structure-Controlling Solventless Synthesis and Optical Properties of Uniform Cu2S Nanodisks. *Chemistry* **2008**, *14*, 11069–11075.

2. Y. Wang; Y. Hu; Q. Zhang; J. Ge; Z. Lu; Y. Hou; Y. Yin. One-Pot Synthesis and Optical Property of copper(I) Sulfide Nanodisks. *Inorg. Chem.* **2010**, *49*, 6601–6608.

3. W. Li; A. Shavel; R. Guzman; J. Rubio-Garcia; C. Flox; J. Fan; D. Cadavid; M. Ibáñez; J. Arbiol; J. R. Morante; A. Cabot. Morphology Evolution of Cu(2-x)S Nanoparticles: From Spheres to Dodecahedrons. *Chem. Commun. (Camb).* **2011**, *47*, 10332–10334.

4. J. M. Pietryga; D. J. Werder; D. J. Williams; J. L. Casson; R. D. Schaller; V. I. Klimov; J. A. Hollingsworth. Utilizing the Lability of Lead Selenide to Produce Heterostructured Nanocrystals with Bright, Stable Infrared Emission. *J. Am. Chem. Soc.* **2008**, *130*, 4879–4885.

5. M. E. Norako; M. a. Franzman; R. L. Brutchey. Growth Kinetics of Monodisperse Cu–In–S Nanocrystals Using a Dialkyl Disulfide Sulfur Source. *Chem. Mater.* **2009**, *21*, 4299–4304.

6. T. Kuzuya; Y. Tai; S. Yamamuro; K. Sumiyama. Synthesis of Copper and Zinc Sulfide Nanocrystals via Thermolysis of the Polymetallic Thiolate Cage. *Sci. Technol. Adv. Mater.* **2005**, *6*, 84–90.

7. H. Li; M. Zanella; A. Genovese; M. Povia; A. Falqui; C. Giannini; L. Manna. Sequential Cation Exchange in Nanocrystals: Preservation of Crystal Phase and Formation of Metastable Phases. *Nano Lett.* **2011**, *11*, 4964–4970.

8. P. Espinet; M. C. Lequerica. Synthesis , Structural Characterization and Mesogenic Behavior of Copper(i) N-Alkylthiolates. *Chem. Eur. J* **1999**, *5*, 1982–1986.

9. J. B. Rivest; P. K. Jain. Cation Exchange on the Nanoscale: An Emerging Technique for New Material Synthesis, Device Fabrication, and Chemical Sensing. *Chem. Soc. Rev.* **2013**, *42*, 89–96.

10. X. Li; H. Shen; J. Niu; S. Li; Y. Zhang; H. Wang. Columnar Self-Assembly of Cu2S Hexagonal Nanoplates Induced by Tin ( IV ) -X Complex as Inorganic Surface Ligand. *J. Am. Chem. Soc.* **2010**, *132*, 12778–12779.

11. M. V. Kovalenko; M. I. Bodnarchuk; J. Zaumseil; J.-S. Lee; D. V. Talapin. Expanding the Chemical Versatility of Colloidal Nanocrystals Capped with Molecular Metal Chalcogenide Ligands. *J. Am. Chem. Soc.* **2010**, *132*, 10085–10092.

# 5. Dodecaneselenol: a new selenium precursor

## 5.1. Introduction

As shown in chapter 3, 1-dodecanethiol (DDT) forms lamellar Cu-thiolate complexes which, after stabilization with halides, can be used for the synthesis of ultrathin $Cu_{1.8}S$ NSs. To see whether this mechanism also applies for a synthesis of $Cu_{2-x}Se$ NSs, a new precursor, 1-dodecaneselenol (DDSe), was synthesized and investigated. This new selenium precursor has some advantages over the currently used Se precursors, since very few reactive Se precursors are known. Although organic precursors like bis(trimethylsilyl)selenide can be used, most of these organic precursors suffer from stability issues due to the decreasing bonding strength of selenium.[1] Furthermore, the heavier chalcogenides like selenium and tellurium are rather difficult to dissolve in non-coordinating solvents like ODE, which forces the synthesis to be either diluted or requires the aid of strong coordinating ligands.[2,3] The most widely used coordinating ligands are trialkylphosphine ligands.[4,5] When heating is applied, selenium can be coordinated to trioctylphosphine (TOP), forming a trialkylphosphine selenide as shown in Scheme 5.1A. The main issue with using trialkylphosphine in metal chalcogenide syntheses is the habit of trialkylphosphines to strongly bind to metals, especially softer metals like $Cu^+$.[6] Therefore, the use of TOP=Se strongly influences the size and shape of the final NCs, as previously shown in chapter 3 (Figure 3.8D), where the addition of TOP to the $Cu_{2-x}S$ NSs synthesis yielded quasi-spherical QDs rather than NSs, and thus suppressed the halide the Cu-thiolate complexes.

Although DDSe has been used to study self-assembled monolayers on noble metal substrates, the use as a Se-precursor in the synthesis of NCs has not been demonstrated.[7,8] Therefore, the synthesis of DDSe (Scheme 5.1B) introduced in this chapter holds a large promise as an interesting alternative for the currently used Se-precursors. Furthermore, the use of DDSe as Se-precursor could result in the synthesis of ultrathin $Cu_{2-x}Se$ NSs in a similar way as described in chapter 3.

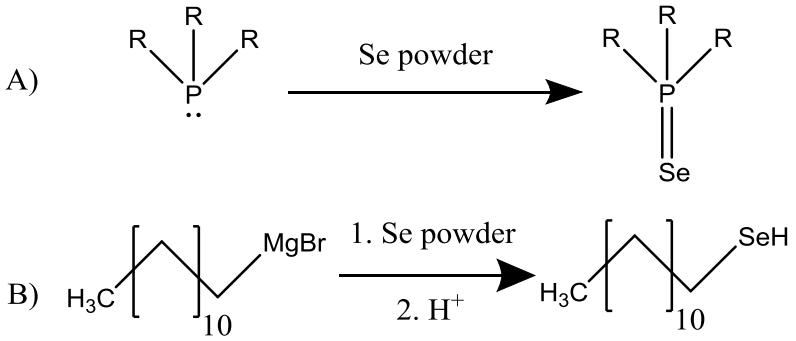


**Scheme 5.1: (A) Currently the most used selenium precursor; coordination of selenium to a trialkylphosphine. (B) Proposed selenium precursor from this thesis; 1-dodecaneselenol synthesized with a Grignard reaction.**

This chapter will cover the synthesis of the DDSe precursor and the use of DDSe in the synthesis of $Cu_{2-x}Se$ platelets as follows. The experimental section (5.2) will describe the used materials, the synthesis of the DDSe precursor, the synthesis of $Cu_{2-x}Se$ platelets using the DDSe precursor, the cation exchange on the $Cu_{2-x}Se$ platelets towards CdSe and finally the used equipment. The results and discussion, section 5.3, will cover the results of the synthesis of the DDSe precursor, the $Cu_{2-x}Se$ platelets and CdS platelets. The final two sections will present the conclusions drawn from these syntheses (section 5.4) and an outlook containing further research possibilities (section 5.5).

## 5.2. Experimental

This section, containing al the experimental information, will be divided as follows. After the used materials in section 5.2.1, the synthesis of the DDSe precursor will be described (section 5.2.2). The third section, 5.2.3, will describe the synthesis of the $Cu_{2-x}Se$ platelets obtained by using the DDSe precursor. Section 5.2.4 will describe the method used for the cation exchange synthesis of the CdSe platelets. The final section sections, 5.2.5-5.2.8, will give further details on the used equipment including the syntheses set-ups for the NCs, the electron microscope, the x-ray diffractometer and the absorption and PL measurements.

### 5.2.1. Materials

Dodecylmagnesium bromide solution (DMB, 1M in ether) was purchased from Sigma Aldrich and used without any further purification. The selenium powder (Se, 99.99%) was bought from Alfa. The metal salts copper(I) bromide (CuBr, 98%), copper(I) acetate (CuOAc, 97%), tin(IV) tetrabromide ($SnBr_4$, 99%), tin(IV) tetrachloride pentahydrate ($SnCl_4.5H_2O$, 98%), cadmiun(II) oxide (CdO, trace metal, 99.5 %), sodium bromide (NaBr, ≥99%) and calcium chloride (CaCl, 93.0%) were also purchased from Sigma Aldrich and used without further purification. Ligands and solvents were purchased from Sigma Aldrich, like trioctylphosphine (TOP, 90%), 1-dodecanethiol (DDT, ≥98%), 1-octadecene (ODE, tech., 90 %), trioctylphosphine oxide (TOPO, 99%), oleic acid (OA, 90%), anhydrous toluene, methanol and butanol. ODE, TOPO and OA needed to be degassed prior to synthesis.

### 5.2.2. 1-Dodecaneselenol

The synthesis of the DDSe is an adaptation of the synthesis described by G. Froster *et al.* in 1955, where phenylselenol was synthesized using a Grignard reaction.[9] In this synthesis, a selenium atom is inserted into alkyl magnesium bromide forming magnesium bromide alkylselenolate, which can be further protonated with hydrochloric acid to finally form the alkylselenol. The general reaction scheme is given in Scheme 5.2.

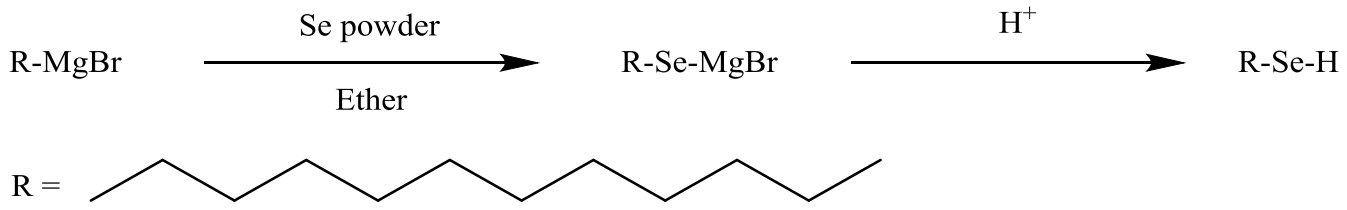


**Scheme 5.2: Reaction scheme for the synthesis of the DDSe precursor.**

For this synthesis, a 250 ml 3-neck roundbottom flask with a water-cooled condenser, a glass stop and a $90^0$ turn extension with a reversed glass stop, were flame dried under vacuum and put under a nitrogen atmosphere. Meanwhile, 4.56 g (57.8 mmol) selenium powder was weighted into a flame dried schlenktube in a glovebox. The schlenktube, while maintained under nitrogen atmosphere, was connected to a second schlenkline. The schlenktube containing the Se and the $90^0$ turn extension on the roundbottom flask, both with an overpressure of nitrogen, assuring no oxygen entered the dried set-up, were connected and the schlenktube was disconnected from the schlenkline. The glass stop on the roundbottom flask was replaced with a rubber septum. A graphical representation of the set-up before the start of the synthesis, as described till this point, is given in Figure A5.1. Subsequently, 60 ml DMB solution (60 mmol) was added through the septum with a nitrogen flushed syringe. While rapidly stirring, the selenium powder was slowly added over a period of 30 minutes by slowly turning the schlenktube horizontal and 'tapping' the schlenktube. While adding the selenium, the reaction mixture turned from clear dark black/brown to turbid white/grey indicating the formation of the insoluble magnesium bromide dodecylselenolate. After stirring for an extra three hours while slowly refluxing, the reaction mixture was poured into (~1:1 in volume) iced water. While stirring the mixture, ~9 ml 37 % hydrochloric acid was slowly added. The now white suspension was filtered with filter paper and collected in a 250 ml separation funnel. The lower water layer was removed and the upper layer containing the DDSe, ether, dodecane (a side product due to the protonation of the Grignard reagent with water) and dodecanediselenide (oxidation product of DDSe) were dried with $CaCl_2$. After the removal of $CaCl_2$ by filtration, the crude DDSe was collected in a 100 ml roundbottom flask. The ether was removed by using a rotary evaporator. The dodecaneselenol was further purified by using vacuum distillation where the clear colorless to slight yellow DDSe was collected at a temperature of ~105 $^0$C with a pressure of 2.5 torr. The residue of the distillation was dark yellow, indicating the separation of the dodecanediselenide (DDSe-SeDD) from the DDSe. The final product was collected in a vial taped with black tape and finally stored in a glovebox. This is done due to the fact that DDSe is easily oxidized by light and air to form the yellow solid DDSe-SeDD, as shown in Scheme 5.3. For the same reason, the washing and work up of the reaction was carried out as fast as possible, to minimize oxidation by air.

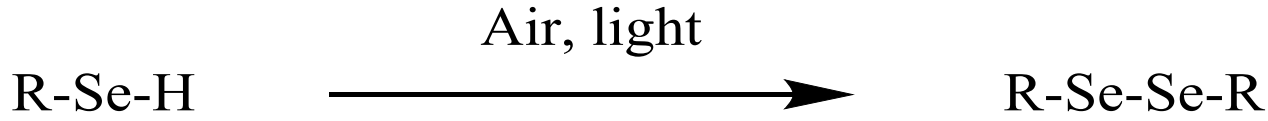


**Scheme 5.3: Oxidation of DDSe into the di-selenide, DDSe-SeDD.**

### 5.2.3. $Cu_{2-x}Se$ platelets

This synthesis is an adaptation of the synthesis for the $Cu_{1.8}S$ NSs (section 3.2.2) but with the use of CuBr, NaBr and DDSe as precursors. Typically, 31.6 mg (0.22 mmol) of CuBr and 30.8 mg (0.30 mmol) of NaBr were dispersed in 12.5 mL previously degassed ODE together with 0.55 g of TOPO. The mixture was degassed for 30 minutes at a temperature of 100 ˚C. Following, the solution was gradually heated to 130 ˚C and at this temperature, 0.6 mL DDSe was swiftly injected under vacuum. Directly after the injection, the reaction solution turned clear yellow/orange and was purged with a $N_2$ gas flow. The temperature was further increased to 170 ˚C and turned turbid brown/black at ~150 $^0$C. The solution was maintained at this temperature for 40 minutes. The $Cu_{2-x}Se$ NCs were precipitated by adding a methanol/butanol solution and centrifuging at 3000 rpm for 15 minutes. Afterwards, the particles were redispersed in toluene. These washing steps were repeated three times.

### 5.2.4. CdSe nanoplatelets via cation exchange

This method was first described by Li *et al.*[10] Here, 1.0 mmol CdO was dissolved in 1.3 ml OA and 1.3 ml ODE at 280 $^0$C in a glovebox. 1 ml of $Cu_{2-x}Se$ NCs were redispersed in 1.5 ml TOP and swiftly injected into the hot Cd-precursor solution. After 10 minutes, the mixture was cooled to room temperature by removal of the heating source. Subsequently, the NCs were washed once with a methanol/butanol solution and centrifuged at 3000 rpm for 15 minutes. Afterwards, the particles were redispersed in toluene.

### 5.2.5. Synthesis set-ups

For the hot-injection syntheses, the following set-up was used; a 50 ml 3-neck-roundbottomflask containing a magnetic stirring bean was fitted with two septa (one for the thermocouple and the other for the hot injection) and a Vigreux condenser. The Vigreux condenser was connected to a Schlenkline with a 2.5 torr vacuum and a 40 $L_n$/h nitrogen pressure. The heating source was a Horst HTMC1/69 thermocouple set at step 2 and was changed to step 1 20 $^0$C below the final growth temperature to prevent the temperature from rising too high. A VWR hotplate/stirrer was used for stirring and was set at 600 rpm. Samples were taken with a 20 mL glass syringe with an iron needle and stored in glass vials with a septum. These vials were prepared within a glove box to keep the samples oxygen free. The cation exchange reactions were performed in 20 ml glass vials placed on an A VWR hotplate/stirrer within a glovebox.

### 5.2.6. Electron microscopy

For the Transmission electron microscopy (TEM) measurements, a standard FEI Tecnai-10 or FEI Tecnai-12 was used. Samples were prepared on carbon coated polymer film copper grids (300 mesh) in a glove box by dropcasting 10-50 µl (depending on the dilution) of sample on the grids.

### 5.2.7. X-ray diffractometry

For the X-ray diffractometry, a Philips PW1729 x-ray generator and PW 3710 MBP controller were used at 40 kV and 20 mA and with a Cu $K_\alpha$ source ($\lambda$=1.5418 Å). Samples were prepared by dropcasting a concentrated NCs solution on a Si wafer. The concentrated NCs solution was prepared as follows. 1 mL of sample was sedimented with a methanol/butanol solution at 3000 rpm for 15 minutes and redispersed in a few drops of chloroform. The chloroform dispersion was dropcasted on a small piece of Si wafer and the chloroform was evaporated. The small piece of wafer was taped on an aluminum holder. The low angle measurements ranged from 5.3-25$^0$. The crystal structure determination measurements ranged from 20-75$^0$. In both cases multiple measurements (5-15 measurements, depending on the quality) were conducted to increase the signal to noise ratio.

### 5.2.8. Absorption and photoluminescence spectroscopy

Absorption spectra were measured on a Perkin-Elmer Lamdba 950 UV/VIS spectrophotometer. In general, samples were diluted in toluene and absorbance was measured from 280-800 nm with a step size of 1 nm. Photoluminescence (PL) and PL excitation spectra were measured on an Edinburgh Instruments Spectrofluorometer equipped with a detector sensitive in the visible region (either a Hamamatsu H7422-02 or Hamamatsu R928) and a 900W Xe lamp as source. Each spectrum consisted of three measurements to increase the signal to noise ratio. In general, a stepsize of 2 nm and a dwell time of 0.5 s were used. Samples were prepared in a glove box and transferred to quartz cuvettes (1 cm pathlenght), which were closed with a screwcap to keep the samples from oxidation.

## 5.3. Results and discussion

### 5.3.1. 1-Dodecaneselenol

When the synthesis described in section 5.2.2 was carried out, a colorless to slight clear yellow liquid product was obtained. As with thiols, the product had a foul stench, being the first indication of a successful synthesis of DDSe. The synthesis had a relative low yield of 30% according to analysis of the product with $^1$H-NMR, as shown in Figure 5.1. The triplet at 0.85 ppm belongs to the –$CH_3$ protons situated at the end of the alkyl chain

of DDSe. The -$CH_2$- protons situated next to the –SeH shifts to 2.58 ppm. The quintet at 1.75 ppm belongs to the –$CH_2$- protons situated next to the –$CH_2$SeH, as these are still being influenced by the selenium atom. The –$CH_2$- protons between the –$CH_3$ and the –$CH_2CH_2$SeH overlap at 1.5-1.2 ppm. Finally, the selenol proton shows a clear triplet at -0.7 ppm. The selenium of a diselenide is more δ- compared to the selenium of a selenol and therefore, the first and second –$CH_2$- protons next to the diselenide, shift towards a higher chemical shift compared to the same protons in the selenol. The diselenide impuritie can thus be seen at higher chemical shifts, namely at 3.62 ppm and 2.79 ppm. The impurities of the protonated alkyl chain, dodecane (DDH), overlap in the broad peak at 1.5-1.2 ppm. The purity can thus be calculated by comparing the peaks at 1.5-1.2 ppm (DDSe + DDSe-SeDD + DDH), the peak at 2.58 ppm (DDSe + DDSe-SeDD) and the peak at 3.62 ppm (DDSe-SeDD). The purity calculated with these peaks was; 76% DDSe, 22% DDH and 2% DDSe-SeDD. As the main impurity was dodecane, which should not influence the synthesis at low concentrations, no further purification steps were performed. A $^{13}$C-NMR spectrum was also obtained, as shown in Figure A5.2.

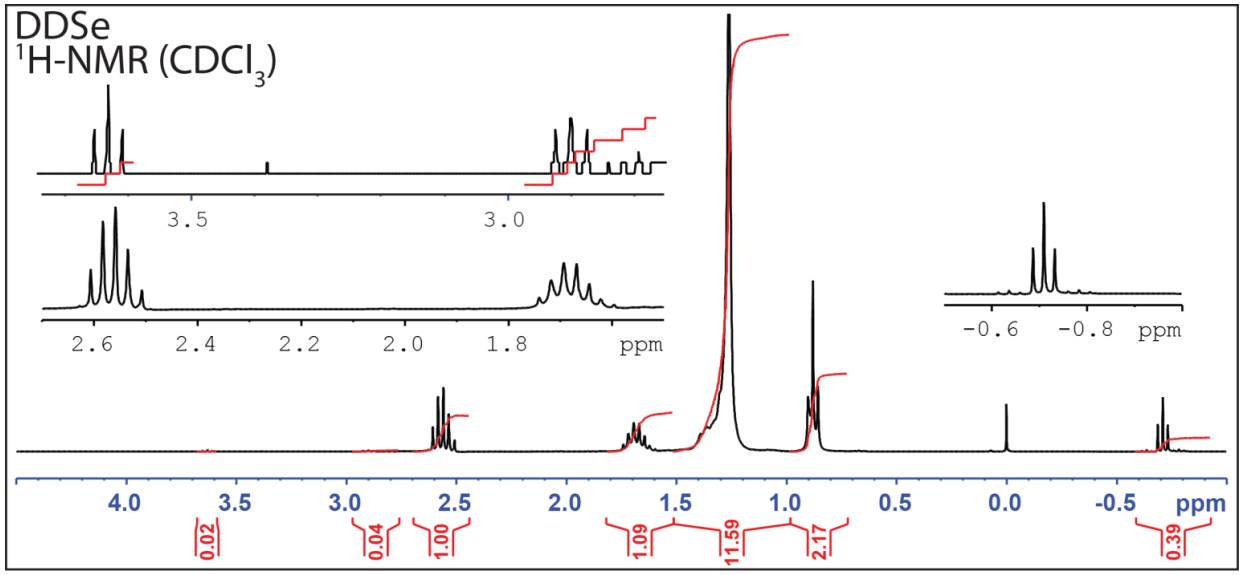


**Figure 5.1: $^1$H-NMR spectrum of the synthesized DDSe.**

When the DDSe was stored either outside the glovebox or in the light, it started to oxidize to the more stable DDSe-SeDD. This was visible as the DDSe slowly turned to a clear yellow solution. After a week of exposure to air and light, yellow crystals could be isolated. These yellow DDSe-SeDD crystals were also characterized with $^1$H-NMR, indicating a purity of 96% (Figure A5.3).

### 5.3.2. $Cu_{2-x}Se$ nanoplatlets

When the synthesis as described in section 5.2.3 was conducted, $Cu_{2-x}Se$ disks (4.8 nm by 28.6 nm) were obtained as shown in Figure 5.2A. Due to the decreased stability of the C-Se bond of DDSe compared to the C-S bond of DDT, lower injection and growth temperatures were needed. The growth and injection temperatures were determined by a heating up variation of the $Cu_{2-x}S$ NSs synthesis. Here, after degassing the Cu-precursor

solution, the solution was brought back to room temperature by removing the heating source. When the precursor solution reached room temperature, DDSe was injected and the temperature was raised to 220 $^0$C. The solution was monitored for color changes indicating the growth of NCs. As mentioned earlier in chapter 3, the NSs synthesis with DDT showed a transition from clear yellow to turbid brown around 200 $^0$C (section 3.2.2). For the heating up synthesis with DDSe, this temperature shifted to 150 $^0$C, indicating the growth of $Cu_{2-x}Se$ NCs. Therefore, the injection temperature for the DDSe was set at 120 $^0$C and the final growth temperature was set at 170 $^0$C. XRD was used to confirm that the platelets indeed were $Cu_{2-x}Se$. Here, a cubic $Cu_{2-x}Se$ crystal structure was found, as will be shown later on in section 5.3.3 (Figure 5.5A).[6]

Although no ultrathin $Cu_{2-x}Se$ NSs were obtained, a synthesis was performed with only CuOAc (comparable to the conditions as described for Figure 3.1A) and thus in the absence of bromide, to see whether a similar mechanism as for the $Cu_{1.8}S$ NSs is a valid for DDSe. As shown in Figure 5.2B, $Cu_{2-x}Se$ polydisperse disk were obtained (3.1 nm by 7.1 nm), indicating that the addition of halides indeed induces lamellar growth.

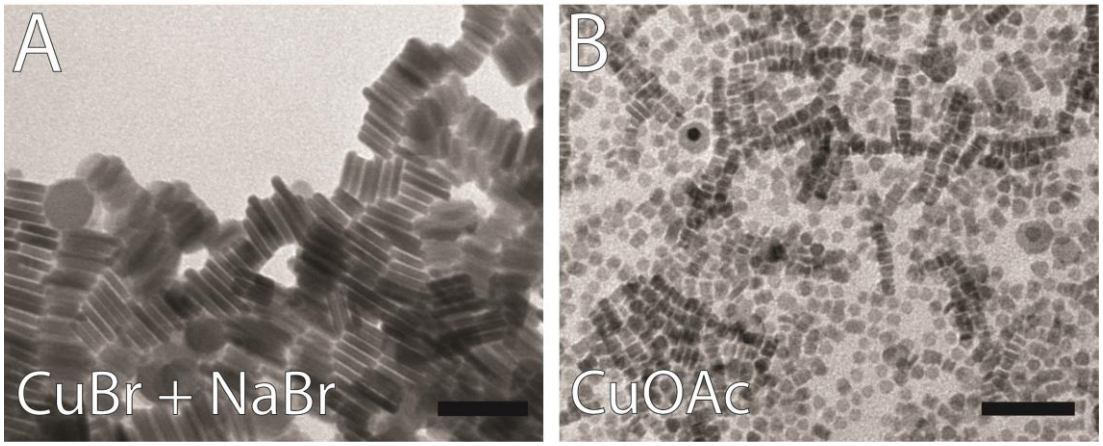


**Figure 5.2: TEM images of $Cu_{2-x}Se$ platelets obtained with the use of DDSe with (A) in the presences of halides, and (B) in the absence of halides. Scale bars correspond to 50 nm.**

To further see whether Cu-DDSe complexes, similar to those of Cu-DDT, are formed, a sample taken one minute after the injection was investigated with XRD. As the low angle XRD diffractogram shows (Figure 5.3A), periodic peaks were observed comparable to the lamellar Cu-thiol complexes.[11] The diffraction peaks of the DDSe and DDT stabilized complexes are identical, both in peak position as in the relative peak intension, which further indicates the formation of the lamellar Cu-selenol complexes. The atomic radii of $S^{2-}$ and $Se^{2-}$ only differ 0.06 nm, which cannot be distinguished with the XRD setup.[12] As with the DDT, a periodic thickness of 3.7 nm was found. A TEM measurement on this sample showed thin cubic sheet like materials, as shown in Figure A5.4. Although these sheets were not further investigated, it could be a stabilized lamellar Cu-Br-selenol complex, comparable to what has been shown previously in chapter 3 for lamellar Cu-thiolate complexes (Figure 3.5A).

Furthermore, absorption and PL spectra were measured on this preliminary sample as shown in Figure 5.3B. These spectra show features comparable to the measured optical properties of the stabilized Cu-Br-thiol complexes as shown in Figure 3.16A. For the Cu-DDSe complex, a strong PL band around 600 nm and a strong absorption band in the ultraviolet around 375 nm were observed. Therefore, it was concluded that the addition of Br indeed induced similar lamellar bromide stabilized Cu-DDSe complexes comparable to those of Cu-Br-thiolates. The absorption and emission bands were ~15 nm blue shifted compared to the absorption and emission band of the Cu-Br-thiol complexes. This can be explained due to the selenol being less electronegative and a softer base compared to a thiol.[13] Therefore, the selenol will bind stronger to the soft $Cu^+$ base, and thus increases the crystal field splitting. The increase of the crystal field will lead to an increase in the $E_g$ and thus to a blue shift of the absorption and emission band.[14]

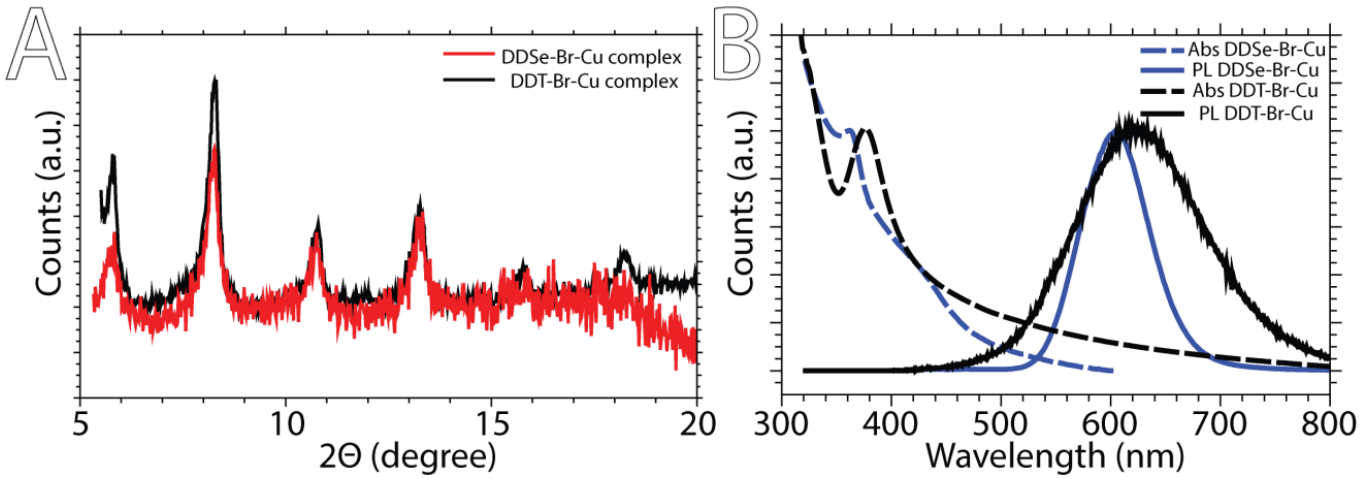


**Figure 5.3: (A) XRD difractogram and optical (absorption and PL) spectra of a sample taken 1 minute after the injection of DDSe compared to a sample taken 1 minute after the injection of DDT of the $Cu_{1.8}S$ NSs synthesis.**

Based on these TEM, XRD and optical measurements, it can be concluded that lamellar Cu-Br-selenol complexes are indeed formed, yet only thick platelets are obtained, and no thin NSs. This could be related to the increase strength of the Cu-Se bond and the decreased strength of the Se-C bond (compared to Cu-S and S-C bond). This may led to the breaking of the Se-C bond, and thus the formation of an isotropic phase as shown in Figure 3.16, before the formation of the $Cu_{2-x}Se$, even with the stabilization of the added bromides.

To see whether the bromide stabilized lamellar Cu-DDSe complexes could be further stabilized, a small amount (0.3 ml) of DDT was injected along with the DDSe. This resulted in platelets with an increased aspect ratio, as shown in Figure 5.4A. These platelets were 4.0 nm thick and 26.0 nm in width, and therefore had an aspect ratio of 6.5. Although the DDT is more stable than the DDSe and therefore needs higher growth temperatures, side nucleation was still observed, leading to small dots aside the $Cu_{2-x}Se$ platelets (Figure 5.4B). Presumably, these small dots are $Cu_{2-x}S$ QDs. Other adaptations for increasing the aspect ratios of the platelets, like using $SnBr_4$ or

$SnCl_4$, lowering the growth temperature, or removing TOPO, all led to either lowering of the aspect ratios of the platelets or to uncontrolled NC growth. These results are shown in Figure A5.5.

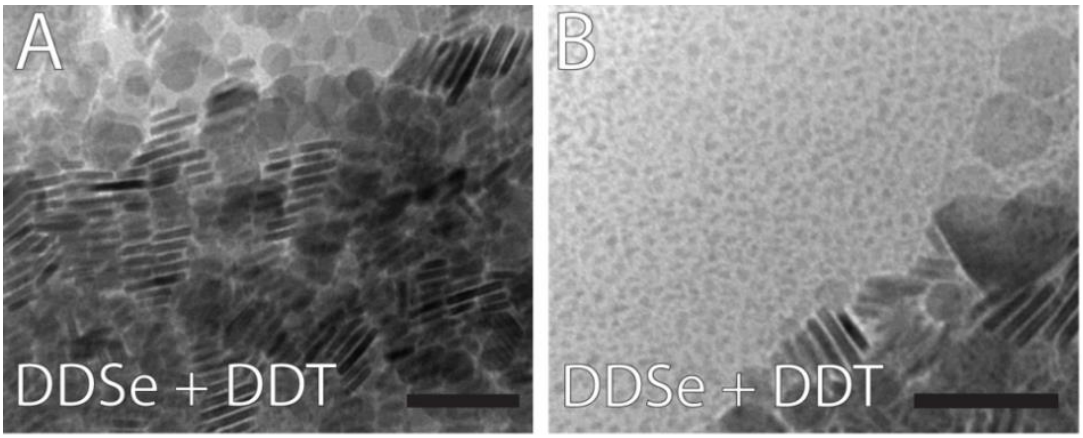


**Figure 5.4: TEM images of (A) the $Cu_{2-x}Se$ platelets obtained with the addition of DDT. (B) Side nucleation was also observed leading to small, dot like NCs. Scale bars correspond to 50 nm.**

### 5.3.3. CdSe nanoplatelets via cation exchange

CdSe platelets were synthesized by the cation exchange method described in section 5.2.4. TEM measurements showed the preservation of the shape and a slight increase in thickness of 4.0 nm to 4.2 nm, as shown in Figure 5.A and B. This increase in size is in agreement with what was found for the cation exchange of $Cu_2Te$ disk to CdTe disks. Li *et al.* ascribed this increase in thickness to the displacement of the Te atoms during the change of crystal structure leading to an perpendicular expansion perpendicular to the lamellar plane, and thus an increase in thickness.[10] Furthermore, XRD analysis was performed to investigate the crystal structure before and after the cation exchange. As Figure 5.5C shows, a crystal structure change from cubic $Cu_{2-x}Se$ to wurtzite CdSe was observed.

The optical properties of the CdSe platelets were investigated with absorption and PL spectroscopy as shown in Figure 5.6. For these measurements, a set of two different sized CdSe platelets was used, namely 3.9 nm and 4.2 nm thick (Figure A5.6). For the 3.9 nm thick platelets, an absorption and emission band at ~620 nm and ~640 nm respectively, were observed. For these platelets, even the second absorption peak was observed at 505 nm. Unlike the CdS NSs described in chapter 3.3.7, the CdSe platelets showed a small Stokes shift of ~60 meV, indicating exitonic emission, comparable to what has been found for spherical CdSe NCs.[15] As for the 4.2 nm thick platelets, a comparable absorption and emission band at slightly lower energies of ~640 nm and ~670 nm were observed. This red shift indicates that these one-dimensional confined CdSe platelets are still experiencing quantum confinement effects. This one-dimensional quantum confinement has been observed for CdSe platelets of several monolayers (1.2-2.1 nm) thick, but has not been shown before for thicker one-dimensional confined CdSe platelets.[16]

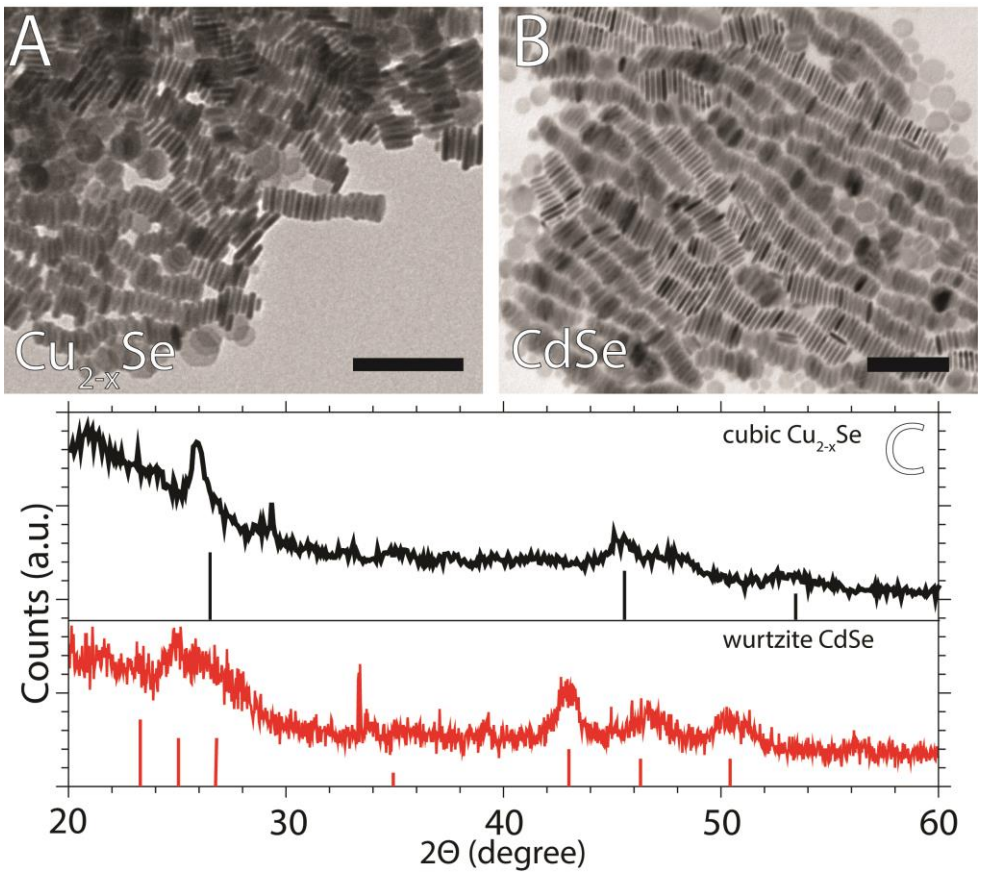


Figure 5.5: Cation exchange on the (A) $Cu_{2-x}Se$ platelets to (B) CdSe platelets. (C) XRD measurements showed a crystal structure change from cubic $Cu_{2-x}Se$ to wurtzite CdSe. Scale bars correspond to 100 nm. Reference bars are from JCPDS card no. [06-0680] and [08-0459] for cubic $Cu_{2-x}Se$ and wurtzite CdSe, respectively.

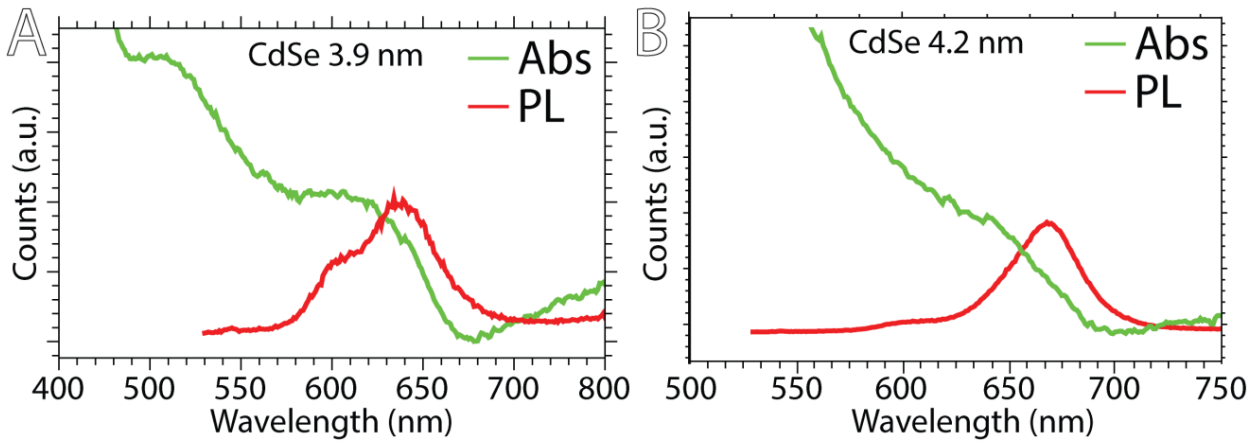


Figure 5.6: Absorption and PL spectra of (A) 3.9 nm thick and (B) 4.2 nm thick CdSe platelets.

When comparing the absorption of the CdSe platelets to the absorption of spherical (three-dimensional quantum confined) CdSe NCs, a red shift is observed. Whereas the 4.2 nm thick platelets have an absorption band at 640 nm, spherical dots with a diameter of 4.3 nm have a absorption band at 590 nm.[17] The absorption band of the platelets is also more broadened, compared to absorption of the spherical CdSe dots. Both the red shift towards bulk CdSe and the broadening of the absorption band indicated that for the one-dimensional confined CdSe

platelets, quantum confinement effects are less dominant, compared to spherical particles with the same diameter. This less strong confinement has been observed for other one-dimensional confined cadmium chalcogenides. For instance, the absorption band of 2.13 nm thick CdSe sheets synthesized by Ithurria *et al.* red shifted approximately 40 nm, which is comparable with the red shift found for the CdSe platelets described in this section. Also CdTe disks of 2.9 nm thickness synthesized by Li *et al.* exhibit this behavior.[10] Here, the red shift, compared to CdTe dots described by Groeneveld *et al.*, can be as high as 100 nm, indicating a strong difference in quantum confinement between three-dimensional and one-dimensional confined NCs. Finally, a red shift of approximately 35 nm can be observed for the CdS sheets synthesized in section 4.3.7, when compared to CdS dots by Yu *et al.*[18]

This red shift and broadening of the absorption band can be explained by the density of states as described in section 2.2.3. With decreasing dimensionality comes an increase of the ground state ($E_g$(bulk) < $E_1$(quantum well) <$E_{11}$(quantum wire) < $E_{111}$(quantum dot). Increasing the dimensionality from a quantum dot (zero-dimensional) to a quantum well (two-dimensional) thus decreases the ground state leading to a smaller bandgap and thus a red shift to lower energies. The peak broadening can be explained by the decreasing number of states with increasing dimensionality. Whereas a quantum dot has very discrete energy levels, a quantum well has less localized energy states and a stepwise shape DOS (Figure 2.3). Therefore, more excitation states are available for a quantum well and thus broader absorption peaks are observed.

## 5.4. Conclusions

In this chapter, a new selenium precursor, 1-dodecaneselenol, was synthesized and used for the synthesis of $Cu_{2-x}Se$ platelets. The synthesis of DDSe was conducted via a Grignard reaction and had a purity of 76% according to $^1$H-NMR and a yield of 30%. As with DDT, the DDSe is able to form Cu-DDSe complexes which can be stabilized by halides, as was confirmed with both XRD and with optical spectroscopy. The use of DDSe in a synthesis adapted from the $Cu_{2-x}S$ NSs yielded $Cu_{2-x}Se$ platelets which were 4.8 nm thick and 28.6 nm in width and therefore had an aspect ratio of 6.0. The addition of a small amount of DDT during the injection of DDSe led to a decrease in thickness and an increase in the width. Therefore, the injection of DDSe with DDT led to an increase of the aspect ratio to 6.8. Based on these results, the stabilizing effect of the bromide did increase the lamellar growth, but not in an extent as with the synthesis of the $Cu_{2-x}S$ NSs.

Furthermore, $Cu_{2-x}Se$ platelets were converted to CdSe with the use of cation exchange, as was confirmed with XRD and optical measurements. Absorption and emission spectra were measured for CdSe platelets with a thickness of 3.9 and 4.2 nm. These measurements showed a red shift of 20 nm for the thicker 4.2 nm CdSe platelets compared to the 3.9 nm platelets, confirming that these one-dimensional platelets still experience quantum confinement effects. Furthermore, a red shift and band broadening for the absorption band compared to

CdSe quantum dots with the same thickness/diameter were observed. This red shift and peak broadening could be explained by the different density of states for the different dimensionality of the NCs.

### 5.5. Outlook

Although the synthesis of the DDSe was successful, the yield and purity were still low. As the main impurity was dodecane, which comes from unreacted dodecylmagnesium bromide, the reaction could be conducted with a slight excess of Se powder. The selenium can later on be removed by the filtration steps. The low yield comes from the loss of DDSe to DDSe-SeDD or due to the final step, the vacuum distillation. The loss of DDSe to DDSe-SeDD can be decreased by working with amber glassware and with glassware purged with nitrogen (as far as possible), preventing oxidation by light and air. The loss by the vacuum distillation comes from the use of a relative long vacuum Vigreux, which led to long distillation times (oxidation by light), high heating temperatures (pyrolysis of DDSe) and simple loss of DDSe left behind after distillation. Conducting the vacuum distillation with a Claisen Adapter instead of a Vigreux, already improved the yield. If the yield and purity cannot be further increased, a different synthesis method could be investigated, for instance the alkylation of selenourea.

It was proven that DDSe was able to form lamellar Cu-selenol complexes, which could be stabilized with bromide ions. Unfortunately, these lamellar complexes still are rather unstable as only platelets were synthesized, rather than NSs, indicating less strong control over the lamellar growth. The synthesis of the $Cu_{2-x}Se$ NPs should be further explored to increase the aspect ratio, or if possible, to eventually synthesize $Cu_{2-x}Se$ platelets by stabilization of the Cu-selenol complexes. Further investigation into growth times and temperatures are still needed. The change to the softer selenium instead of sulfur might also need a different stabilizing ion, for instance the softer $I^-$.

Since DDSe is a new precursor for the synthesis of NCs, other metal precursors should be tested. As mentioned earlier, a variety of lamellar metal-thiolate complexes are known and thus the use of DDSe could led to an interesting general method for the synthesis of ultrathin metal selenide NSs. Moreover, it would be interesting to see whether 1-dodecanol and 1-dodecanetellurol could be used in the same manner as DDSe and DDT for the lamellar Cu-Br complexes. Although DDO and DDTe will suffer from stability issues, as the C-O bond will be hard to break and the C-Te bond will be quite unstable, it could led to a general synthesis method for metal chalcogenide ultrathin nanosheets.

Finally, to further investigate the limit of the one-dimensional quantum confinement on the CdSe platelets, a series of samples should be taken during a synthesis of $Cu_{2-x}Se$ platelets. After CE of these samples to CdSe, absorption, PL, PL excitation and excitation lifetime spectroscopy could give further insight in the quantum confinement limits for these two-dimensional CdSe NCs.

## References


1. S. Kim; Y. T. Lim; E. G. Soltesz; A. M. De Grand; J. Lee; A. Nakayama; J. A. Parker; T. Mihaljevic; R. G. Laurence; D. M. Dor; L. H. Cohn; M. G. Bawendi; J. V Frangioni. Near-Infrared Fluorescent Type II Quantum Dots for Sentinel Lymph Node Mapping. *Nat. Biotechnol.* **2004**, *22*, 93–97.

2. C. Bullen; J. van Embden; J. Jasieniak; J. E. Cosgriff; R. J. Mulder; E. Rizzardo; M. Gu; C. L. Raston. High Activity Phosphine-Free Selenium Precursor Solution for Semiconductor Nanocrystal Growth. *Chem. Mater.* **2010**, *22*, 4135–4143.

3. C. Bullen; J. van Embden; J. Jasieniak; J. E. Cosgriff; R. J. Mulder; E. Rizzardo; M. Gu; C. L. Raston. Phosphine-Free Synthesis of CdSe Nanocrystals. *J. Phys. Chem. B* **2005**, *109*, 20665–20668.

4. C. Bouet; B. Mahler; B. Nadal; B. Abecassis; M. D. Tessier; S. Ithurria; X. Xu; B. Dubertret. Two-Dimensional Growth of CdSe Nanocrystals, from Nanoplatelets to Nanosheets. *Chem. Mater.* **2013**, *25*, 639–645.

5. S. Ithurria; G. Bousquet; B. Dubertret. Continuous Transition from 3D to 1D Confinement Observed during. *J. Am. Chem. Soc.* **2011**, *133*, 3070–3077.

6. J. Choi; N. Kang; H. Y. Yang; H. J. Kim; S. U. Son. Colloidal Synthesis of Cubic-Phase Copper Selenide Nanodiscs and Their Optoelectronic Properties. *Chem. Mater.* **2010**, *22*, 3586–3588.

7. G. Fonder; J. Delhalle; Z. Mekhalif. Exchange versus Intercalation of N-Dodecanethiol Monolayers on Copper in the Presence of N-Dodecaneselenol and Vice Versa. *Appl. Surf. Sci.* **2010**, *256*, 2968–2973.

8. L. V. Protsailo; W. R. Fawcett; D. Russell; R. L. Meyer. Electrochemical Characterization of the Alkaneselenol-Based SAMs on Au(111) Single Crystal Electrode. *Langmuir* **2002**, *18*, 9342–9349.

9. G. Froster; C. F. H. Allen; H. W. J. Cressman. SELENOPHENOL. *Org. Synth.* **1955**, *3*, 771.

10. H. Li; R. Brescia; M. Povia; M. Prato; G. Bertoni; L. Manna; I. Moreels. Synthesis of Uniform Disk-Shaped Copper Telluride Nanocrystals and Cation Exchange to Cadmium Telluride Quantum Disks with Stable Red Emission. *J. Am. Chem. Soc.* **2013**, *135*, 12270–12278.

11. P. Espinet; M. C. Lequerica. Synthesis , Structural Characterization and Mesogenic Behavior of Copper(i) N-Alkylthiolates. *Chem. Eur. J* **1999**, *5*, 1982–1986.

12. Shriver & Atkins – Inorganic Chemistry, 5th Ed., 2010, Oxford Pub.

13. A. E. Martell. Hard and Soft Acid-Base Behavior in Aqueous Solution: Steric Effects Make Some Metal Ions Hard: A Quantitative Scale of Hardness-Softness for Acids and Bases. *J. Chem. Educ.* **1996**, *73*, 654–661.

14. R. H. Crabtree. The Oranometallic Chemistry of the Transion Metals. *(John Wiley Sons, Inc., Hoboken, New Jersey.)*. **2005**,

15. A. Efros; M. Rosen; M. Kuno; M. Nirmal; D. Norris; M. Bawendi. Band-Edge Exciton in Quantum Dots of Semiconductors with a Degenerate Valence Band: Dark and Bright Exciton States. *Phys. Rev. B. Condens. Matter* **1996**, *54*, 4843–4856.

16. S. Ithurria; M. D. Tessier; B. Mahler; R. P. S. M. Lobo; B. Dubertret; A. L. Efros. Colloidal Nanoplatelets with Two-Dimensional Electronic Structure. *Nat. Mater.* **2011**, *10*, 936–941.

17. C. B. Murray; D. J. Norris. Synthesis and Characterization of Nearly Monodisperse CdE (E = S, Se, Te) Semiconductor Nanocrystallites. *J. Am. Chem. Soc.* **1993**, *115*, 8706–8715.

18. W. W. Yu; L. Qu; W. Guo; X. Peng. Experimental Determination of the Extinction Coefficient of CdTe, CdSe, and CdS Nanocrystals. *Chem. Mater* **2003**, *125*, 2854–2860.

# 6. Self-Assembly of hexagonal Bipyramid- and Bifrustum-Shaped ZnS Nanocrystals*

## 6.1. Introduction

Whereas the previous chapters focused on the synthesis and properties of NCs, this chapter focuses on the self-assembly of NCs into ordered superlattices (NC solids). The self-assembly of colloidal NCs into NC solids is emerging as a versatile approach to design and fabricate novel materials with tailored optoelectronic properties, which are promising for a variety of devices, such as solar cells, LEDs, photodetectors, and lasers.[2–11] The collective properties of NC solids arise from the intrinsic characteristics of the building blocks and the synergistic interactions between them, and can thus be engineered by the choice of the colloidal NCs (composition, size, shape, surface), and the stoichiometry and spatial symmetry of the resulting self-assembled superstructure.[2–5,12,13]

Single- and multicomponent superlattices of isotropic, nearly spherical NCs have been extensively investigated over the last two decades, producing a remarkable variety of superstructures and greatly advancing the fundamental understanding of the self-assembly process.[2,3,14–20] In particular, two-dimensional (2D) superstructures of anisotropic NCs are attracting increasing attention, since their properties may be substantially different from those of three-dimensional (3D) NC superstructures, making them suitable for the fabrication of functional ultrathin films and membranes that take full advantage of the shape-dependent and directional properties of anisotropic NCs. The formation of two-dimensional and three-dimensional self-assembled superstructures has also been studied for other anisotropic colloidal NCs, such as nanoplatelets, truncated cubes, octahedrons, or octapods, both experimentally and by theory and simulation.[17,21–27] Although these studies provided valuable insight in the self-assembly behavior of anisotropic colloidal NCs, the driving forces behind the self-organization process are still not fully understood. For instance, the relationship between the NC shape and the symmetry of the self-assembled superlattice has not yet been investigated in detail.

This chapter will present a combined experimental, theoretical, and simulation study of the self-assembly of hexagonal bipyramid- (BP) and hexagonal bifrustum-shaped (BF) ZnS NCs into two-dimensional superlattices in the following manner. The experimental section, section 6.2, will cover the synthesis of the self-assembled two-dimensional structures and the used methods for the theoretical calculations and the simulations. The next



Ward van der Stam, Anjan P. Gantapara, Quinten A. Akkerman, Giuseppe Soligno, Johannes D. Meeldijk, René van Roij, Marjolein Dijkstra, and Celso de Mello Donega.

Self-Assembly of Colloidal Hexagonal Bipyramid- and Bifrustum-Shaped ZnS Nanocrystals into Two-Dimensional Superstructures.

*Nano Lett.*, **2014**, *14* (2), pp 1032–1037.

chapter (section 6.3) will present the results found for the experimental, theoretical and simulation work conducted. The final two sections will cover the conclusion (section 6.4) and an outlook (section 6.5).

## 6.2. Experimental

The experimental section of this chapter will be presented as follows. The first section, section 6.2.1, will contain the used materials for this chapter. The second section (section 6.2.2) will describe the method used to obtain the self-assembled superstructures. Section 6.2.3 will present the method used for the ligand exchange on the NCs before the self-assembly. The details on the TEM measurements are given in section 6.2.4. The final two sections will present further details on the absorption free energy calculations (section 6.2.5) and the Monte Carlo simulations (section 6.2.6).

### 6.2.1. Materials

Di-ethylene glycol (DEG, 99.0%), was purchased from Sigma Aldrich and used without further purification. Ligands and solvents were purchased from Sigma Aldrich, like trioctylphosphine (TOP, 90%), 1-dodecanethiol (DDT, ≥98%), oleylamine (OLAM, 90%) and anhydrous toluene, methanol and butanol. OLAM needed to be degassed prior to synthesis.

### 6.2.2. Two-dimensional self-assembly at the liquid air interface

In this method, first described by Dong *et al,* a concentrated NC solution is brought onto a very dense liquid surface (DEG).[28] The toluene is allowed to slowly evaporate at room temperature, resulting in the formation of a continuous membrane at the liquid-air interface as shown in Figure 6.1. These membranes were transferred to a TEM-grid by dipping the TEM grid in the solution. Subsequently, the grid was dried overnight prior to further investigation.

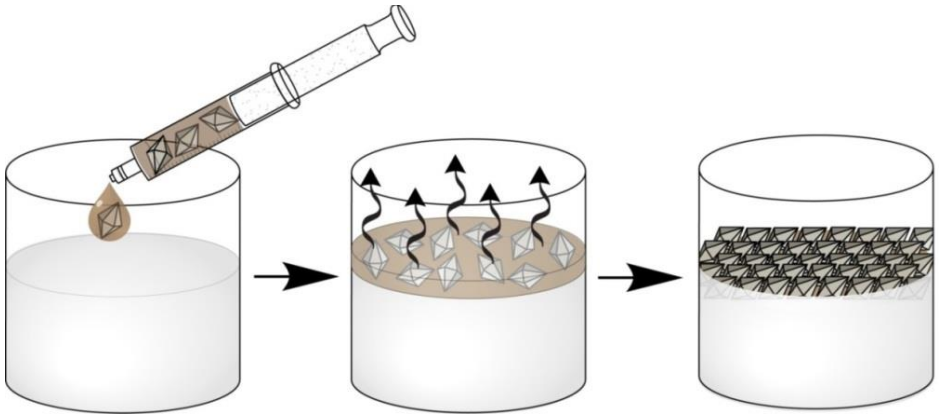

**Figure 6.1: Graphical representation of the liquid air interface method describe by Dong *et al.*[28] Here, a NC solution is slowly evaporated on di-ethylene glycol. This allows for a slow and controlled self-assembly.**

### 6.2.3. Ligand exchange

Here, the ligands on the surface of the NCs were exchanged by dispersing the NCs with the native capping ligands in an excess of the new ligand at ~100 °C for several hours. The NCs were subsequently precipitated by the addition of methanol/butanol solution, isolated by centrifugation, and redispersed in toluene. These reactions were conducted in a glovebox.

### 6.2.4. Electron microscopy

Transmission Electron Microscopy (TEM) measurements were performed on a Tecnai20F (FEI) microscope equipped with a Field Emission Gun, a Gatan 694 CCD camera and an EDAX spectrometer. The microscope was operated at 200 kV. Samples for TEM imaging were prepared by dipping a carbon coated polymer film copper grid (300 mesh) into a self-assembled thin film on a dense di-ethylene glycol surface after evaporation of the solvent (toluene). The TEM-grids were dried overnight prior to imaging.

### 6.2.5. Adsorption free energy calculations

These calculations were performed by G. Soligno, A. P. Gantapara, R. van Roik and M. Dijkstra but are crucial for the understanding of the theoretical work of this chapter and therefore, are described in this section. In this method, the preferred orientation of the NC at a planar air-toluene interface (tension $\gamma_{at}$= 28.52 mN/m) was theoretically obtained by calculating Pieranski-type interfacial adsorption free energies of individual NCs using a triangular tessellation technique,[29] and choosing the configuration that minimizes the adsorption free energy. The NCs were modeled as anisotropic polyhedral hard nanoparticles, with the same dimensions as those experimentally observed (28 by 38 nm for the bipyramids and 33 nm for the bifrustums). Following Pieranksi,[30] the interfacial free energy of a nanoparticle with its center of mass at a height z (with respect to the planar air-toluene interface) and with polar angle $\phi$ (with respect to the interface normal) and $\psi$ (the internal Euler angle about the long axis of the nanoparticle) is written as equation 6.1.

$$F(z, \phi, \psi) = \gamma_a S_a(z, \phi, \psi) + \gamma_t S_t(z, \phi, \psi) - \gamma_{at} S_{at}(z, \phi, \psi) + \text{const.} \qquad (6.1)$$

Here, $S_a$ and $S_t$ denote the area of the particle surface that is in contact with air and toluene, respectively, and $S_{at}$ is the intersection area between the particle and the interface. All three areas $S_a$, $S_t$, and $S_{at}$ depend nontrivially on the position and orientation of the particle, and need to be calculated numerically. The particle-toluene tension is denoted by $\gamma_t$, the particle-air tension by $\gamma_a$, and the arbitrary constant in Equation 6.1 is chosen such that F=0 for a particle that is completely immersed in toluene. The adsorption free energy ignores capillary deformations and line tension contribution for simplicity. In fact, given that the total particle surface area $S_a + S_t$ is a constant, it can

be easily checked that F (z, ϕ, ψ) does not depend on $\gamma_t$ and $\gamma_a$ separately, but only on their difference through the contact angle θ defined by $\cos\theta = (\gamma_a - \gamma_t)/\gamma_{at} = 0.8$, where the numerical value is an estimate based on the observed favorable (low free-energy) configurations (Figure 6.2). With a triangular tessellation technique which calculates the surface areas $S_a$, $S_t$, and $S_{at}$, the equilibrium configuration from minimizing F with respect to the particle configuration can be calculated, as will be presented in the results and discussion (section 6.3.2).

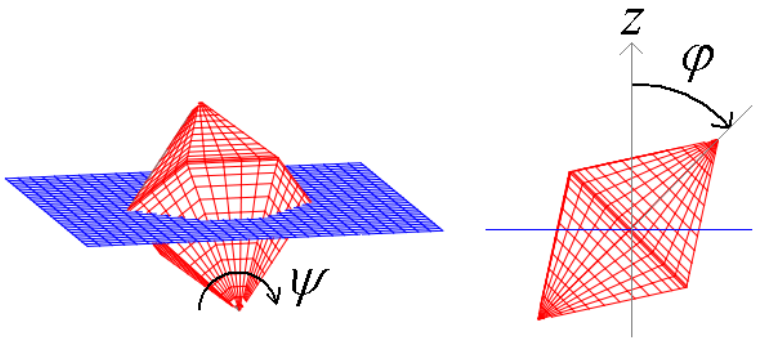


**Figure 6.2: Definition of different orientation angles of the hard particles with respect to the interface (Equation 6.1). Reproduced with permission from ref [1]. Copyright (2014) American Chemical Society.**

### 6.2.6. Monte Carlo simulations

The self-assembled structures were predicted by using the floppy-box Monte Carlo (FBMC) method[31,32] in combination with the separating-axis-based overlap algorithm and performed by A. P. Gantaparaand M. Dijkstra.[33] In the FBMC method, the Monte Carlo simulations were performed in an isothermal-isobaric ensemble (*NPT*) and by compressing a system from the isotropic fluid phase to the solid phase using a variable shape of the simulation box. The immersion depth z and the polar angle ϕ of the nanoparticle with respect to the air-toluene interface are kept fixed according to the values determined for the equilibrium adsorption configurations, and the particles are only allowed to translate and rotate in the plane of the interface. Due to the symmetry of the BFs (*ca.* 33 nm in all directions), the orientation of the NC is not important for the overall self-assembly behavior, since the NC can occupy a hexagonal site in the array regardless of whether a trapezoidal or hexagonal facet is adsorbed to the interface (Figure 6.3). Therefore, for simplicity, only the hexagonal adhered surface is considered in the FBMC simulations. The volume of the nanoparticles v was set to unity in all cases.

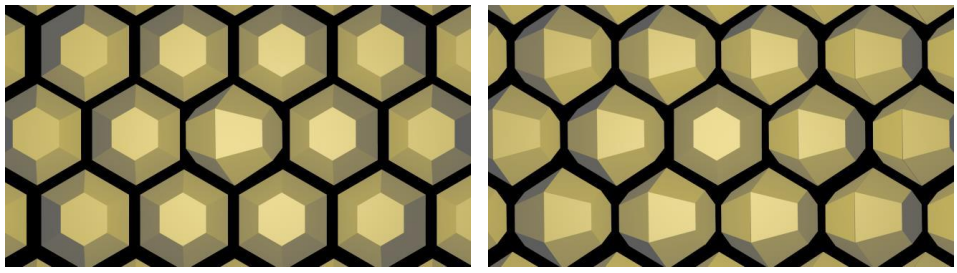

**Figure 6.3: Schematic showing the different orientations of the BFs at the interface. Reproduced with permission from ref [1]. Copyright (2014) American Chemical Society.**

## 6.3. Results and discussion

This section is organized as follows. First, the synthesis and experimental observations will be presented (section 6.3.1). The second section, section 6.3.2, will describe the results of the theoretical calculations and simulations performed for the self-assembled structures.

### 6.3.1. Two-dimensional self-assembly at the liquid air interface

The hexagonal BP and BFs-shaped ZnS NCs used in this chapter were obtained by the exchange of $Cu^{+}$ for $Zn^{2+}$ in djurleite $Cu_{1.96}S$ NCs, as was described in chapter 4 (section 4.2.5). The ZnS BF and BP NCs were self-assembled using the solvent evaporation technique on a liquid-air interface, as described in section 6.2.4. Micrometer scale ordered superlattices were obtained in all cases (Figure 6.4A and B). The BP ZnS NCs yielded self-assembled arrays with tetragonal symmetry (Figure 6.4A-C), whereas the BF ZnS NCs self-organized into hexagonal superlattices (Figure 6.4D-F). SEM analysis revealed that the BP NCs are all oriented in the same direction, with one tip pointing upwards, and the other adhered to the substrate (Figure 6.4C). SEM analysis also revealed that the tips of the BP ZnS NCs are slightly truncated. This tip truncation is very common in colloidal NCs, since it minimizes their overall free energy.[34] As with the $Cu_{1.96}S$ BF NCs (Figure 6.4), SEM showed that the BF NCs can adopt multiple spatial orientations at the substrate (Figure 6.4F), while yielding similar hexagonal two-dimensional TEM projections (Figure 6.4E). This is mainly due to the shape uniformity of the bifrustum NCs viewed from different directions (Figure A6.2).

In contrast to the ZnS NCs assemblies, the parent $Cu_{1.96}S$ NCs did not form two-dimensional superlattices with the liquid-air interface method, but instead formed small domains of three-dimensional superstructures as shown in Figure A6.1. Considering that the size and shape of the parent $Cu_{1.96}S$ NCs are preserved in the product ZnS NCs, the disparity in their self-organization behaviors can be ascribed to their dissimilar surfaces (both in terms of chemical composition and ligand capping), which could give rise to different inter-NC interactions, and hence alter the forces driving the self-assembly process. The inability of the parent $Cu_{1.96}S$ NCs to form two-dimensional superlattices under the same conditions as used for the product ZnS NCs was further investigated with a ligand exchange experiment. The $Cu_{1.96}S$ NCs are capped by alkylthiols, while the ZnS NCs are likely capped by OLAM and Cl ions. After the ligand exchange as described in section 6.2.3, superlattices were no longer formed for ZnS NCs coated with DDT (Figure 6.5A) or TOP (Figure 6.5B), while an excess of OLAM had no effect on the ability to form superstructures (Figure 6.5C).

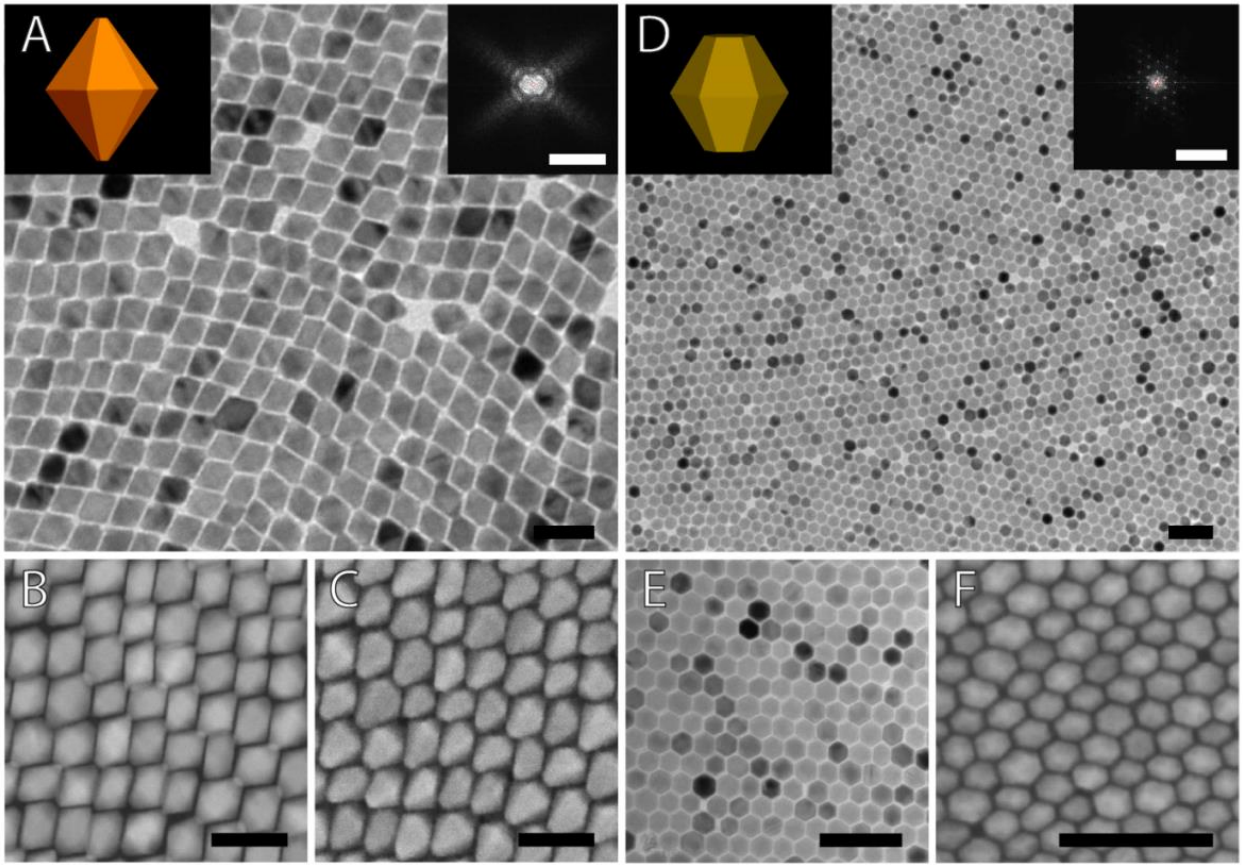


Figure 6.4: Electron Microscopy images of self-assembled superlattices of hexagonal bipyramid-shaped ZnS NCs (A-C, TEM, dark-field STEM, SEM, respectively), and hexagonal bifrustum-shaped ZnS NCs (D-F, TEM and SEM, respectively). Fast Fourier Transform (FFT) patterns of the superlattices are shown as insets in the top right corner of the corresponding TEM images (A and D). Insets in the top left corner show schematic representations of the shapes of the NCs (slightly truncated hexagonal bipyramid and hexagonal bifrustum, for A and D, respectively). The scale bars correspond to 50 nm in A-C and to 100 nm in D-F. FFT: 0.2 $nm^{-1}$. Reproduced with permission from ref [1]. Copyright (2014) American Chemical Society.

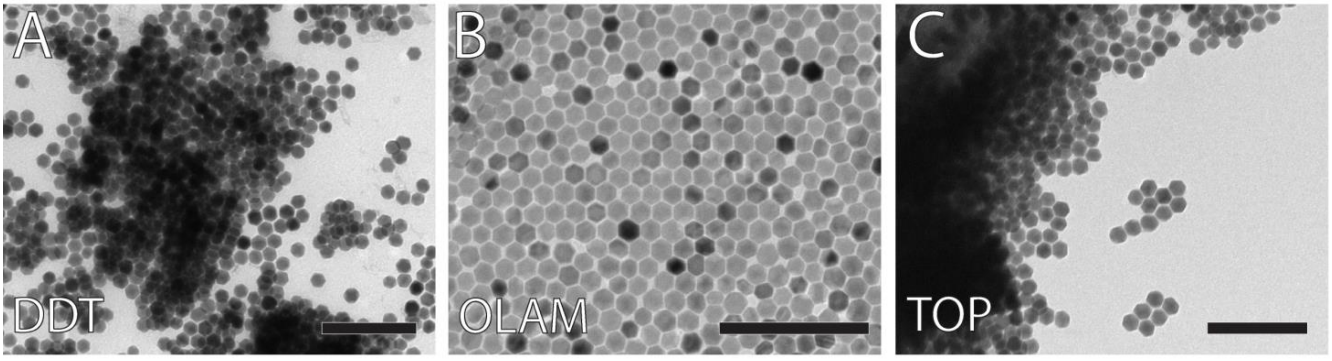


Figure 7.5: TEM images of the NC solids obtained from self-assembly experiments using hexagonal bifrustum ZnS NCs with different capping ligands: (A) DDT, (B) additional OLAM and (C) TOP. Scale bars correspond to 200 nm. Reproduced with permission from ref [1]. Copyright (2014) American Chemical Society.

### 6.3.2. Adsorption free energy calculations and Monte Carlo simulations

To understand the experimentally observed self-assembly behavior of both the product ZnS NCs and the parent $Cu_{1.96}S$ NCs, theoretical calculations and computer simulations were performed by Anjan P. Gantapara and Giuseppe Soligno. Using the method described in section 6.2.4, the equilibrium configuration of the absorption free energy could be calculated for three different particle shapes (perfect hexagonal bipyramids, truncated hexagonal bipyramid and hexagonal bifrustum). Figure 6.6 shows these equilibrium configurations, as well as the free energy as a function of the polar angle (minimized with respect to z and the internal angle ψ). The perfect BP has minimum free-energy when one of its triangular facets is completely adhered to the interface (Figure 6.6A). For this configuration, a local minimum of $F \approx -200\ k_BT$ is found. It is interesting to note that the particle remains completely immersed in the liquid phase, except for the facet that is adhered to the interface (whereas the particle pays a free energy penalty of $F \approx 10^4\ k_BT$ if it is completely in air). The colloidal NCs used in the self-assembly experiments were, however, not perfect BP, but instead have slightly truncated tips (5% of their length). Nevertheless, according to the calculation this small truncation does not affect the single-particle equilibrium configuration at the interface, which remains essentially the same as that of a perfect BP (Figure 6.6B). By contrast, according to the calculations a BF NCs has *two* possible equilibrium configurations, in which either one of the twelve trapezoidal facets or one of the two hexagonal facets is adhered to the interface (Figure 6.6C). Both free-energy minima are sufficiently deep (more than 200 kT) to make the adhesion irreversible (Figure 6.6C), and consequently the hexagonal bifrustum nanoparticles have multiple options for interfacial adhesion.

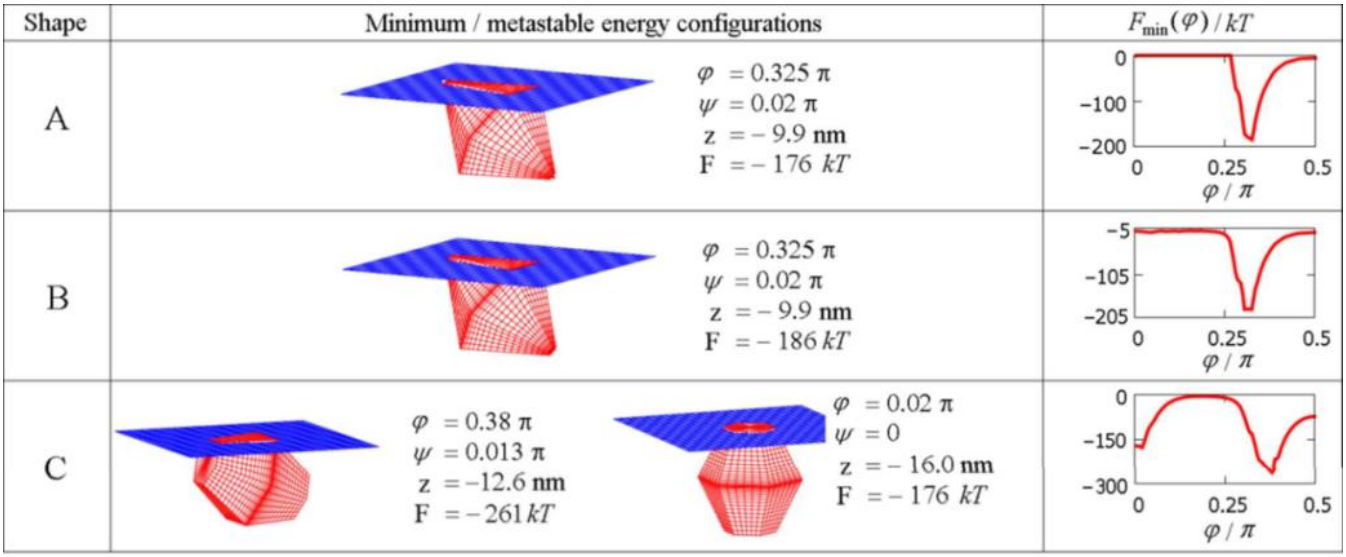


**Figure 6.6. Minimum free-energy orientations obtained from theoretical free-energy calculations for hard particles with three different shapes: (A) perfect hexagonal bipyramid, (B) slightly truncated hexagonal bipyramid, and (C) hexagonal bifrustums. The right panels give the interfacial free-energy of the particle as a function of the internal Euler angle about the long axis of the nanoparticle, φ. Reproduced with permission from ref [1]. Copyright (2014) American Chemical Society.**

Once the equilibrium adsorption configurations of the three different shapes at the air-toluene interface were theoretically determined, the self-assembled structures were predicted by using the floppy-box Monte Carlo (FBMC) method, described in section 6.2.5. The self-assembled structures in Monte Carlo simulations were used to determine the phase behavior of an ensemble of NCs. Furthermore, the equations of states for the Monte Carlo simulations were calculated as shown in Figure A6.2. A set of snapshots of various stages during the *NPT* compression is shown in Figure 6.7. The change in the color of the particles is related to the orientation of the particles. Therefore, a more uniform color means that more NCs are oriented in the same direction.

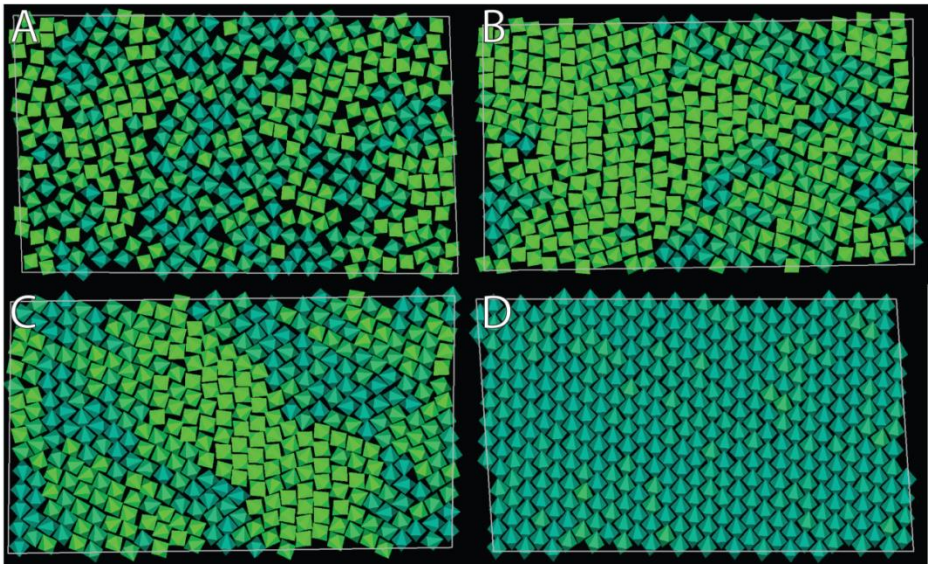


**Figure 6.7: Snapshots of the isothermal-isobaric Monte Carlo simulations on the perfect BP NCs. Snapshots A-D show an increasing compression. As is clear from the increase in the uniformity of the color, the NCs orient in the same direction with increasing packing density. Courtesy of Anjan P. Gantapara.**

The crystal structure can be determined from the reciprocal space pattern of the center of mass of the particles in the simulated NC superstructure. Figure 6.8 shows the reciprocal space patterns and the real space configurations of the NC superlattices formed during the FBMC simulations at two different reduced densities $\rho^* = \rho v^{2/3} = 0.65$ and 0.69 with v as the particle volume, $\rho = N/A$ is the areal number density, N is the number of particles, and A is the surface area of the interface. The experimentally observed NC superlattices are also included for comparison (Figure 6.8A–B). The simulations show that perfect hexagonal bipyramids crystallize via a first-order phase transition with coexisting densities $\rho^* \approx 0.56$ and 0.57 into a hexagonal superlattice (Figure 6.8C). Hexagonal bifrustums also crystallize via a firstorder transition from the isotropic fluid into a hexagonal lattice with coexisting densities $\rho^* \approx 0.50$ and 0.52 (Figure 6.8E). In contrast, slightly truncated bipyramids show a weak first-order transition from the isotropic phase to a tetragonal phase around $\rho^* \approx 0.58$ (Figure 6.8D). This is remarkable because the equilibrium configuration of the single NC adhered to the air–toluene interface was not significantly affected by the truncation (Figure 6.6). This can be rationalized by considering that the truncation allows the

NCs to come in closer proximity, thereby leading to a higher packing density, and hence a tetragonal rather than hexagonal lattice.

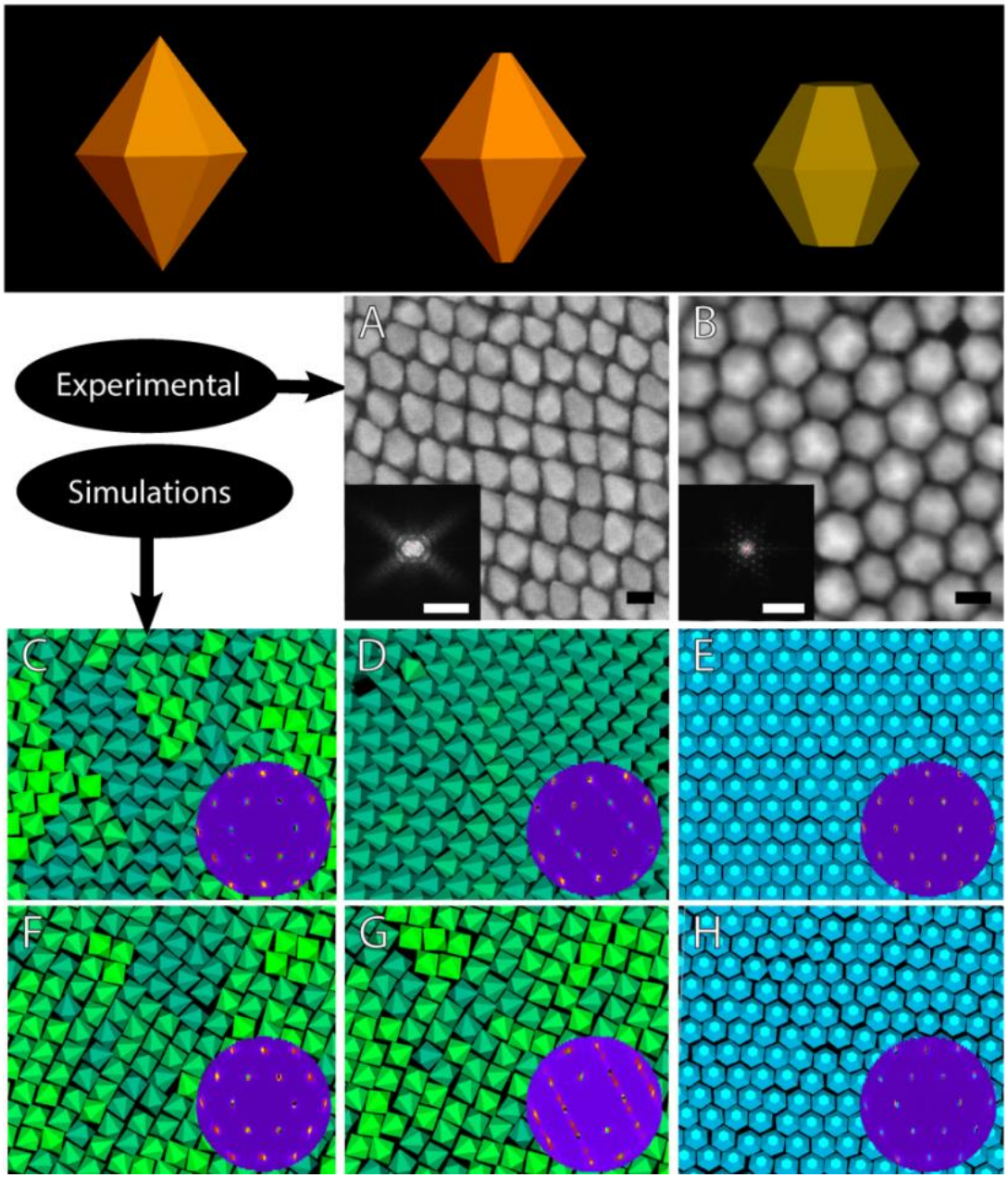


Figure 7.8: Top panel: Schematics of the particle geometries used in the Monte Carlo simulations. Second row from top: SEM images of selfassembled superlattices of (A) hexagonal bipyramid-shaped ZnS NCs, and (B) hexagonal bifrustum-shaped ZnS NCs. The insets give the FFT patterns of the superlattices. The scale bars correspond to 20 nm (0.2 nm−1 in the insets). Bottom two rows. Snapshots of the isothermal–isobaric Monte Carlo simulations showing the various structures that form during the 2D self-assembly of hexagonal bipyramids (C,D,F,G) and hexagonal bifrustums (E,H) adhered to an air–toluene interface. The corresponding reciprocal space patterns of the center of mass of the particles in the simulated NC superlattice are also displayed (bottom right insets). The orientation of the particles with respect to the interface is fixed based on the equilibrium configurations obtained from the interfacial free-energy calculations (see Figure 2). The relative orientation of the particles is color coded. (C–E) Simulation snapshots at a reduced density $\rho^* = \rho v^{2/3} = 0.69$ with v as the particle volume. (F–H) Simulation snapshots at $\rho^* = 0.65$. Reproduced with permission from ref [1]. Copyright (2014) American Chemical Society.

The agreement between the simulated and experimentally obtained two-dimensional NC superlattices is very good, indicating that the self-assembly process of the ZnS NCs is driven primarily by minimization of the interfacial free energies and maximization of the packing densities. The inability of the parent $Cu_{1.96}S$ NCs to form two-dimensional superlattices under the same conditions as used for the product ZnS NCs can be thus attributed to the presence of additional inter-NC interactions that disrupt the self-assembly process by modifying the interfacial tensions and/or introducing attractive/repulsive potentials.

## 6.4. Conclusions

In conclusion, this chapter shows that micrometer scale two-dimensional superlattices of hexagonal BP- and BF shaped ZnS NCs can be obtained by self-assembly at the liquid-air interface. The self-assembly behavior is well described by a combination of theoretical adsorption free-energy calculations and Monte Carlo simulations, which shows that the superlattice formation is driven primarily by minimization of the interfacial free energies and maximization of the packing densities. Moreover, the results show that truncation of the tips of hexagonal bipyramids by as little as 5% is sufficient to change the symmetry of the resulting superlattice from hexagonal to tetragonal. This demonstrates that precise shape control is of crucial importance in the fabrication of functional materials by self-assembly of colloidal NCs. The work described in this chapter may thus provide a versatile design and fabrication route for tailored two-dimensional superlattices of anisotropic NCs of metal chalcogenides, in which cation exchange reactions are used to convert self-assembled superlattices of zinc chalcogenide NCs into different materials, while preserving the size and shape of the NC building blocks as well as the symmetry and long-range order of the superstructure. From a theoretical and modelling perspective it is very comfortable to note that the relatively simple Pieranski potential, Equation 6.1, combined with Monte Carlo simulations actually has quantitative predictive power, which may be further exploited in the study of other particle shapes and material parameters.

## 6.5. Outlook

The size, shape and composition of the anisotropic NCs could be further investigated. Combining the morphology rich chemistry of the parent $Cu_{1.96}S$ NCs and the CE towards ZnS could lead to a general versatile tool for highly crystalline anisotropic ZnS superlattices. Furthermore, combining the use of different shaped parent NCs and either exchanging the $Cu^{+}$ (prior CE) or $Zn^{2+}$ (post CE) to for instance $Cd^{2+}$ or $Pb^{2+}$ could lead to an overall general method for the self-assembly of highly crystalline anisotropic metal sulfide superlattices.

As mentioned earlier, the single- and multicomponent superlattices of isotropic, nearly spherical NCs have been extensively investigated. Binary superlattices containing anisotropic NCs only were very recently made possible[4,35]. Currently, Ward v. d. Stam and Da Wang are working on these binary self-assembled superlattices containing

anisotropic ZnS NCs. Here, the binary superlattice contains the anisotropic ZnS BF or BP NCs in combination with isotropic spherical gold or $Fe_2CoO_4$ NCs. Ideally, the spherical NCs will be situated in between the corners of the ZnS NCs as shown in Figure 6.9A. One of the self-assemblies with the ZnS BPs and the $Fe_2CoO_4$ NCs already showed the favored position of the $Fe_2CoO_4$ NCs at the corners between the ZnS NCs (Figure 6.9B). This method could lead to large two-dimensional binary superlattices or three-dimensional binary supercrystals.

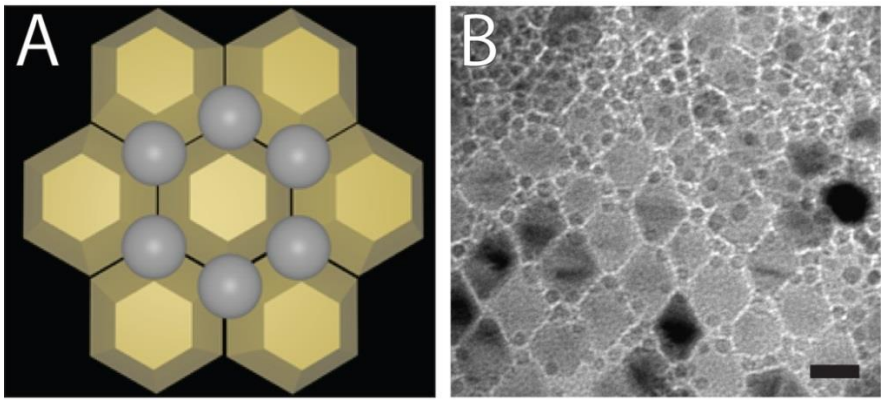


**Figure 6.9: (A) Three-dimensional model of binary superlattices with anisotropic ZnS BFs NCs and isotropic spherical NCs. (B) TEM images of the first trial with the ZnS BP and 6.0 nm spherical $Fe_2CoO_4$ NCs already shows a preferred position for the spherical NCs in between the ZnS BP NCs. The scale bar in (B) correspond to 20 nm.**

## References


1. W. van der Stam; A. P. Gantapara; Q. a Akkerman; G. Soligno; J. D. Meeldijk; R. van Roij; M. Dijkstra; C. de Mello Donega. Self-Assembly of Colloidal Hexagonal Bipyramid- and Bifrustum-Shaped ZnS Nanocrystals into Two-Dimensional Superstructures. *Nano Lett.* **2014**, *14*, 1032–7.

2. M. V. Kovalenko; M. I. Bodnarchuk; J. Zaumseil; J.-S. Lee; D. V. Talapin. Expanding the Chemical Versatility of Colloidal Nanocrystals Capped with Molecular Metal Chalcogenide Ligands. *J. Am. Chem. Soc.* **2010**, *132*, 10085–10092.

3. D. Vanmaekelbergh. Self-Assembly of Colloidal Nanocrystals as Route to Novel Classes of Nanostructured Materials. *Nano Today* **2011**, *6*, 419–437.

4. T. Paik; C. B. Murray. Nanocrystal Puzzle with Shape-Complementary Building Blocks. *Nano Lett.* **2013**, *13*, 2952–2956.

5. Z. Nie; A. Petukhova; E. Kumacheva. Properties and Emerging Applications of Self-Assembled Structures Made from Inorganic Nanoparticles. *Nat. Nanotechnol.* **2010**, *5*, 15–25.

6. Y. Shirasaki; G. J. Supran; M. G. Bawendi; V. Bulović. Light-Emitting Technologies. *Nano photonics* **2013**, *7*, 13–23.

7. L. Sun; J. J. Choi; D. Stachnik; A. C. Bartnik; B.-R. Hyun; G. G. Malliaras; T. Hanrath; F. W. Wise. Bright Infrared Quantum-Dot Light-Emitting Diodes through Inter-Dot Spacing Control. *Nat. Nanotechnol.* **2012**, *7*, 369–373.

8. F. Pisanello; L. Martiradonna; P. Spinicelli; A. Fiore; J. P. Hermier; L. Manna; R. Cingolani; E. Giacobino; M. De Vittorio; A. Bramati. Dots in Rods as Polarized Single Photon Sources. *Superlattices Microstruct.* **2010**, *47*, 165–169.

9. E. Talgorn; Y. Gao; M. Aerts; L. T. Kunneman; J. M. Schins; T. J. Savenije; M. a van Huis; H. S. J. van der Zant; A. J. Houtepen; L. D. A. Siebbeles. Unity Quantum Yield of Photogenerated Charges and Band-like Transport in Quantum-Dot Solids. *Nat. Nanotechnol.* **2011**, *6*, 733–739.

10. A. H. Ip; S. M. Thon; S. Hoogland; O. Voznyy; D. Zhitomirsky; R. Debnath; L. Levina; L. R. Rollny; G. H. Carey; A. Fischer; K. W. Kemp; I. J. Kramer; Z. Ning; A. J. Labelle; K. W. Chou; A. Amassian; E. H. Sargent. Hybrid Passivated Colloidal Quantum Dot Solids. *Nat. Nanotechnol.* **2012**, *7*, 577–582.

11. J. Tang; K. W. Kemp; S. Hoogland; K. S. Jeong; H. Liu; L. Levina; M. Furukawa; X. Wang; R. Debnath; D. Cha; K. W. Chou; A. Fischer; A. Amassian; J. B. Asbury; E. H. Sargent. Colloidal-Quantum-Dot Photovoltaics Using Atomic-Ligand Passivation. *Nat. Mater.* **2011**, *10*, 765–771.

12. R. Y. Wang; J. P. Feser; J.-S. Lee; D. V Talapin; R. Segalman; A. Majumdar. Enhanced Thermopower in PbSe Nanocrystal Quantum Dot Superlattices. *Nano Lett.* **2008**, *8*, 2283–2288.

13. Y. Kang; X. Ye; J. Chen; L. Qi; R. E. Diaz; V. Doan-Nguyen; G. Xing; C. R. Kagan; J. Li; R. J. Gorte; E. a Stach; C. B. Murray. Engineering Catalytic Contacts and Thermal Stability: Gold/iron Oxide Binary Nanocrystal Superlattices for CO Oxidation. *J. Am. Chem. Soc.* **2013**, *135*, 1499–1505.

14. J. J. Urban; D. V Talapin; E. V Shevchenko; C. R. Kagan; C. B. Murray. Synergism in Binary Nanocrystal Superlattices Leads to Enhanced P-Type Conductivity in Self-Assembled PbTe/Ag2 Te Thin Films. *Nat. Mater.* **2007**, *6*, 115–121.

15. E. V Shevchenko; D. V Talapin; N. a Kotov; S. O'Brien; C. B. Murray. Structural Diversity in Binary Nanoparticle Superlattices. *Nature* **2006**, *439*, 55–59.

16. J. R. Heath. Synergy in a Superlattice. *Nature* **2007**, *445*, 492–493.

17. W. H. Evers; B. Goris; S. Bals; M. Casavola; J. de Graaf; R. van Roij; M. Dijkstra; D. Vanmaekelbergh. Low-Dimensional Semiconductor Superlattices Formed by Geometric Control over Nanocrystal Attachment. *Nano Lett.* **2013**, *13*, 2317–2323.

18. Z. Chen; S. O'Brien. Structure Direction of II-VI Semiconductor Quantum Dot Binary Nanoparticle Superlattices by Tuning Radius Ratio. *ACS Nano* **2008**, *2*, 1219–1229.

19. M. Grzelczak; J. Vermant; E. M. Furst; L. M. Liz-marza. Directed Self-Assembly of Nanoparticles. *ACS Nano* **2010**, *445*, 3591–3605.

20. M. P. Boneschanscher; W. H. Evers; W. Qi; J. D. Meeldijk; M. Dijkstra; D. Vanmaekelbergh. Electron Tomography Resolves a Novel Crystal Structure in a Binary Nanocrystal Superlattice. *Nano Lett.* **2013**, *13*, 1312–1316.

21. D. C. Reifsnyder; X. Ye; T. R. Gordon; C. Song; C. B. Murray. Three-Dimensional Self-Assembly of Chalcopyrite Copper Indium Diselenide Nanocrystals into Oriented Films. *ACS Nano* **2013**, *7*, 4307–4315.

22. T. R. Gordon; T. Paik; D. R. Klein; G. V Naik; H. Caglayan; A. Boltasseva; C. B. Murray. Shape-Dependent Plasmonic Response and Directed Self-Assembly in a New Semiconductor Building Block, Indium-Doped Cadmium Oxide (ICO). *Nano Lett.* **2013**, *13*, 2857–2863.

23. W. Qi; J. de Graaf; F. Qiao; S. Marras; L. Manna; M. Dijkstra. Ordered Two-Dimensional Superstructures of Colloidal Octapod-Shaped Nanocrystals on Flat Substrates. *Nano Lett.* **2012**, *12*, 5299–5303.

24. K. Miszta; J. de Graaf; G. Bertoni; D. Dorfs; R. Brescia; S. Marras; L. Ceseracciu; R. Cingolani; R. van Roij; M. Dijkstra; L. Manna. Hierarchical Self-Assembly of Suspended Branched Colloidal Nanocrystals into Superlattice Structures. *Nat. Mater.* **2011**, *10*, 872–876.

25. W. Du; X. Qian; X. Ma; Q. Gong; H. Cao; J. Yin. Shape-Controlled Synthesis and Self-Assembly of Hexagonal Covellite (CuS) Nanoplatelets. *Chemistry* **2007**, *13*, 3241–3247.

26. W. J. Baumgardner; K. Whitham; T. Hanrath. Confined-but-Connected Quantum Solids via Controlled Ligand Displacement. *Nano Lett.* **2013**, *13*, 3225–3231.

27. X. Ye; J. Chen; M. Engel; J. A. Millan; W. Li; L. Qi; G. Xing; J. E. Collins; C. R. Kagan; J. Li; S. C. Glotzer; C. B. Murray. Competition of Shape and Interaction Patchiness for Self-Assembling Nanoplates. *Nat. Chem.* **2013**, *5*, 466–473.

28. A. Dong; J. Chen; P. M. Vora; J. M. Kikkawa; C. B. Murray. Binary Nanocrystal Superlattice Membranes Self-Assembled at the Liquid-Air Interface. *Nature* **2010**, *466*, 474–477.

29. J. de Graaf; M. Dijkstra; R. van Roij. Adsorption Trajectories and Free-Energy Separatrices for Colloidal Particles in Contact with a Liquid-Liquid Interface. *J. Chem. Phys.* **2010**, *132*, 164902.

30. P. Pieranski. Two-Dimensional Interfacial Colloidal Crystals. *Phys. Rev. Lett.* **1980**, *45*, 569–572.

31. J. de Graaf; L. Filion; M. Marechal; R. van Roij; M. Dijkstra. Crystal-Structure Prediction via the Floppy-Box Monte Carlo Algorithm: Method and Application to Hard (non)convex Particles. *J. Chem. Phys.* **2012**, *137*, 214101.

32. L. Filion; M. Marechal; B. van Oorschot; D. Pelt; F. Smallenburg; M. Dijkstra. Efficient Method for Predicting Crystal Structures at Finite Temperature: Variable Box Shape Simulations. *Phys. Rev. Lett.* **2009**, *103*, 188302.

33. D. Eberly. Intersection of Convex Objects : The Method of Separating Axes. *http://www.geometrictools.com/*

34. C. de Mello Donegá. Synthesis and Properties of Colloidal Heteronanocrystals. *Chem. Soc. Rev.* **2011**, *40*, 1512–1546.

35. X. Ye; J. a Millan; M. Engel; J. Chen; B. T. Diroll; S. C. Glotzer; C. B. Murray. Shape Alloys of Nanorods and Nanospheres from Self-Assembly. *Nano Lett.* **2013**, *13*, 4980–4988.

# 7. Acknowledgments

As all good things come to an end, so has my time as a masterstudent at the Condensed Matter and Interfaces group in Utrecht. The past one and a half year has been a great year and I've learned a lot. For this, I would like to thank some people. Most of all, I would like to thank Ward van der Stam (Captain Kesterite). Over time, Ward has been become more than just my daily supervisor. You taught me a lot of new science skills, but also became a good friend. I also would like to specially thank Celso de Mello Donegá for sharing his knowledge and time with me (even the meetings on Friday from 4 till 7 pm!). I could not image a better supervisor! For the synthesis of the 1-dodecanethiol I'd like to thanks Joost van der Lit for his organic chemistry knowledge and Vera Kats for the NMR analyses. A part of this thesis has been published in Nanoletters and therefor I would like to thank Anjan P. Gantapara, Giuseppe Soligno, Renévan Roij and Marjolein Dijkstra for their collaboration. Another thanks goes to Hans Meeldijk, for performing all the "special" TEM measurements at Utrecht. Hans Ligthart of course also gets a big thanks for helping me around the lab. Furthermore, I would like to thank Xiaoxing Ke and Sara Bals: not only for the HRTEM measurements in Antwerp, but also for the great hospitality when Ward and I visited EMAT. I would also like to thank Freddy for helping me with the optical measurements on the Eddy's.

Finally, I would like to thank my fellow (master) students with whom I spend my time at CMI for the great and 'awesome' year including; my fellow 'Borrelcommissie' members (Tim and Robin, the 'borrels' and playing 'Sinterklaas' with you has been an honor), my two desk neighbors (Jantina and Jasper, my 'sogging' partners in crime), the other members of Team Kestire (Josine and Anne, the meetings and the final Pizza diner were always good times) and all the other people who came and went. It has been an awesome one and a half year!


**Keywords: Team Kesterite, super promising, "chocoblerf", the dreamteam**

# Appendices

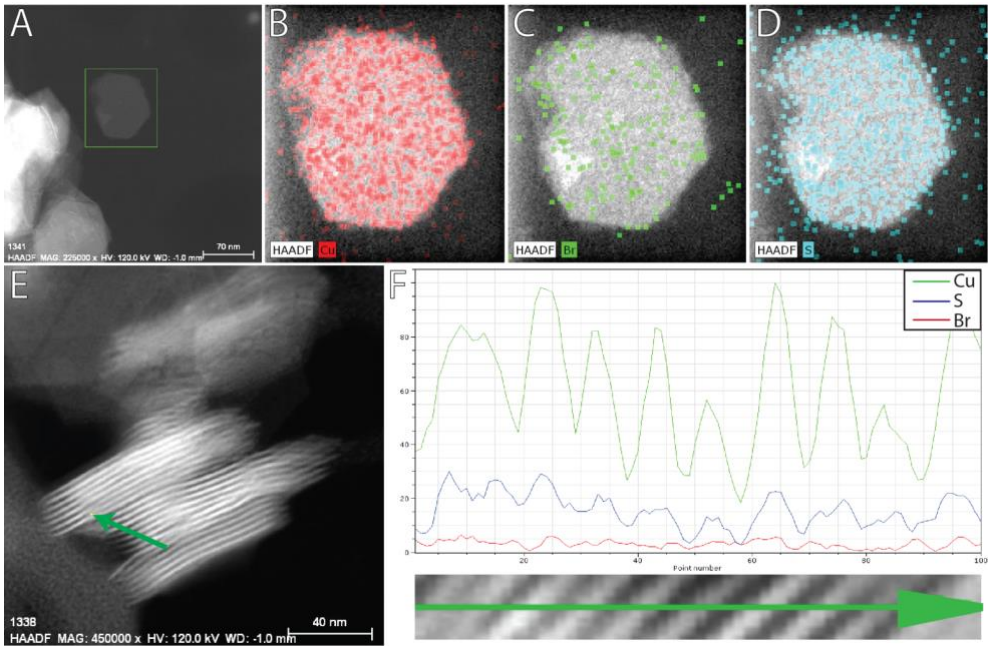


Figure A3.1; Further investigation in the distribution of the Br. (A-D) STEM-HAADF chemical mapping experiments and (E and F) STEM-EDS

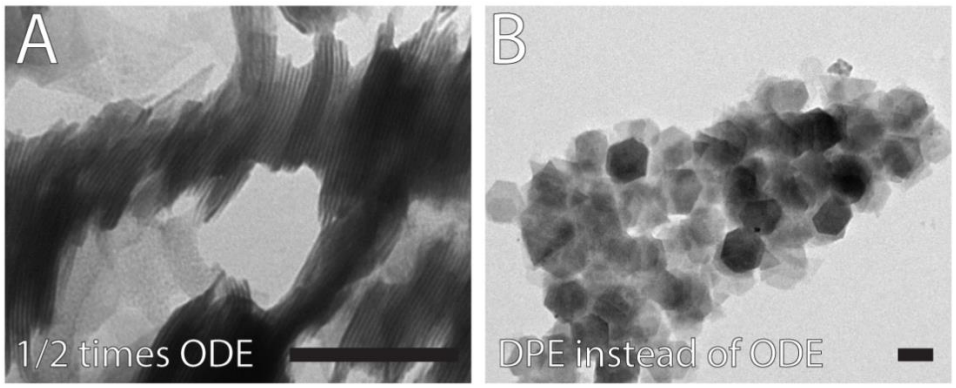


Figure A3.2; TEM images of the Cu2-xS nanosheets with different solvent conditions with (A) twice as concentrated (1/2 times ODE) and (B) a DPE as solvent (1:0.04 DPE:ODE). Scale bars correspond to 100 nm.

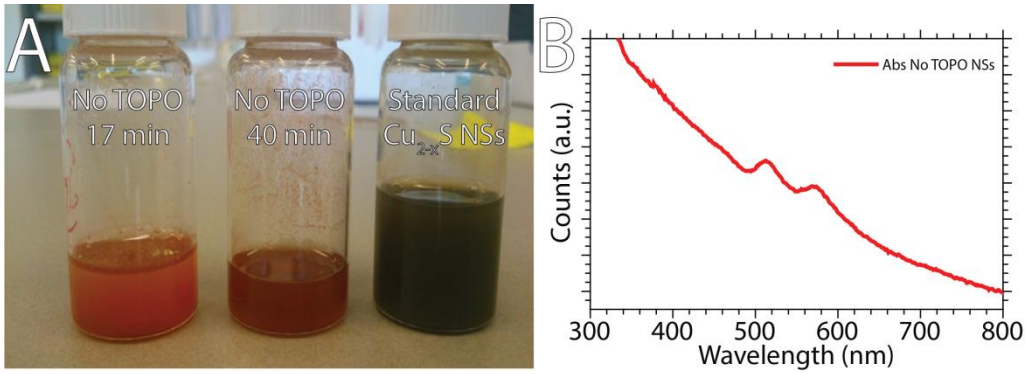


Figure A3.3: (A) photo of the different samples containing $Cu_{2-x}S$ nanosheets. (B) Absorption spectroscopy of the µm sized NSs

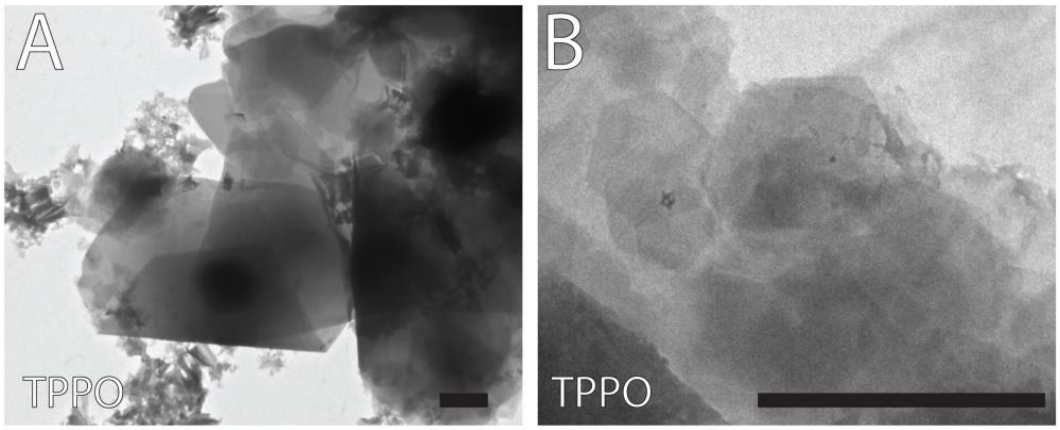


Figure A3.4: TEM images of the $Cu_{2-x}S$ nanosheets synthesis with TPPO instead of TOPO. Both (A) large irregular as (B) smaller sized nanosheets materials were found. Scale bars correspond to 1 µm.

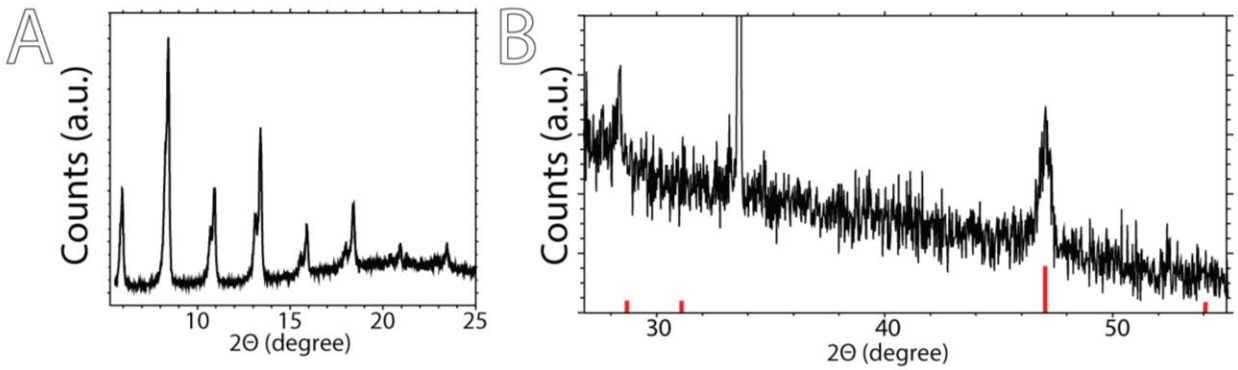


Figure A3. 5: XRD measurement of synthesis with triangular nanosheets showing (A) at low angles and (B) at higher angles. Red bars are from JCPDS card no. [47-1748] for hexagonal digenite.

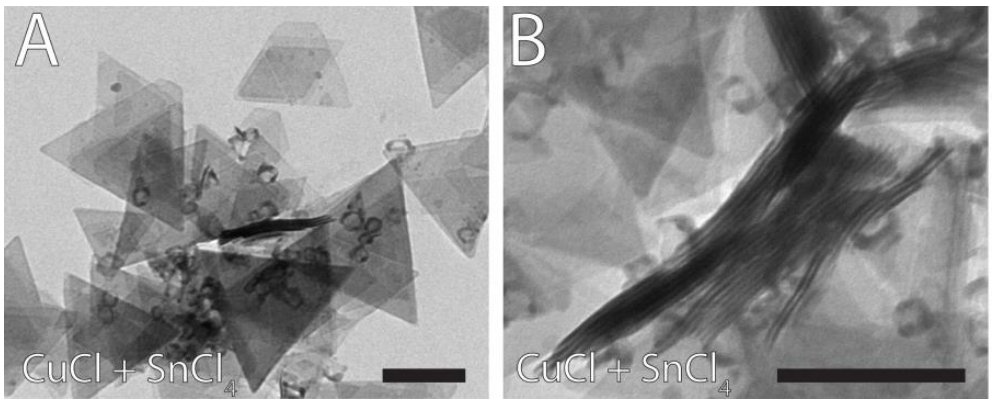


Figure A3,6: TEM images of a nanosheets synthesis performed where CuOAc and $SnBr_4$ were replaced by CuCl and NaCl. Scale bars correspond to 100 nm.

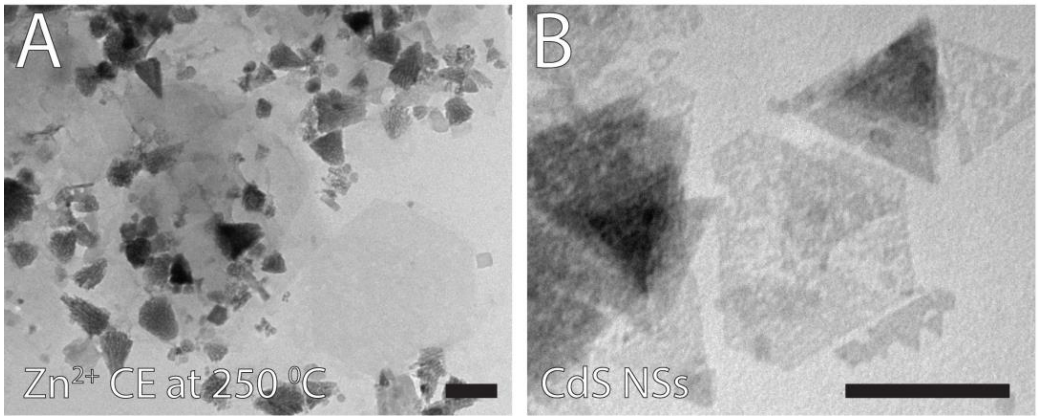


Figure A3,7: (A) TEM images unsuccessful cation exchange reactions of ZnS. (B) Sample after cation exchange to CdS. Scale bars correspond to 100 nm.

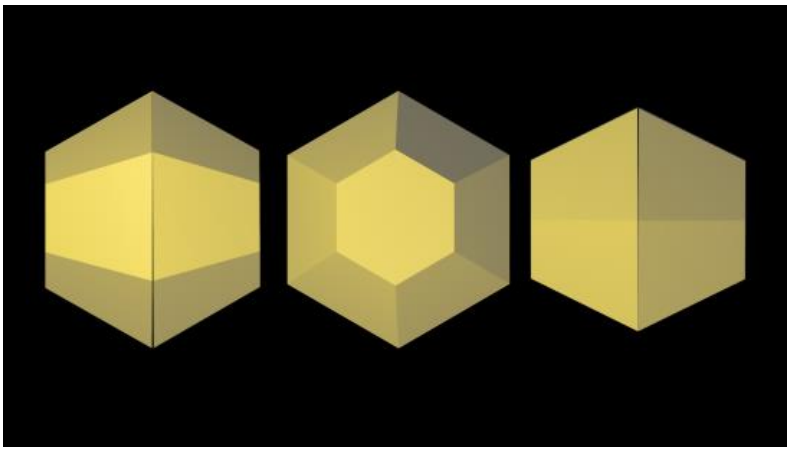

Figure A4.1: three different oriented hexagonal bifrustums al resulting in a hexagonal 2D projection.

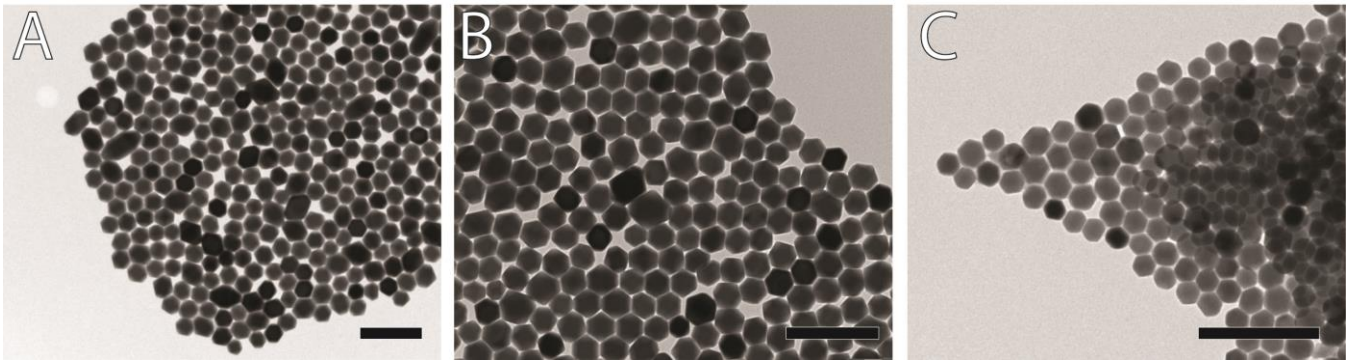


Fig A4.2: TEM images of samples with small changes in the synthesis conditions. (A) Lowering the injection temperature to 180 °C, (B) using non-degassed ODE instead of degassed ODE and (C) the correct conditions described in ref 14 for hexagonal BFs instead of BPs. Scale bars correspond to 200 nm.

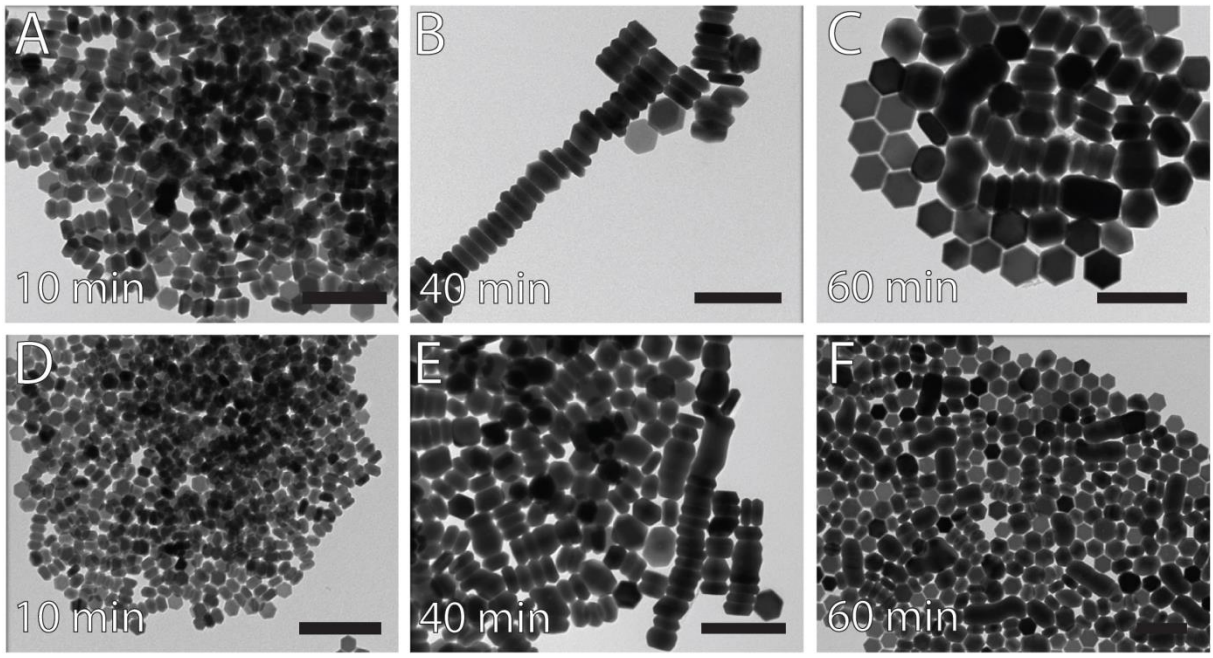


Figure A4.3: TEM images of two attempts for synthesizing hexagonal BPs. (A)-(C) 1½ times more Cu(I)Cl. Intermediate samples after (A) 10 min, (B) 40 min and (D) 60 min. (D)-(E) 1½ times less OLAM. Intermediate samples after (D) 10 min, (E) 40 min and (F) 60 min. Scale bars correspond to 200 nm.

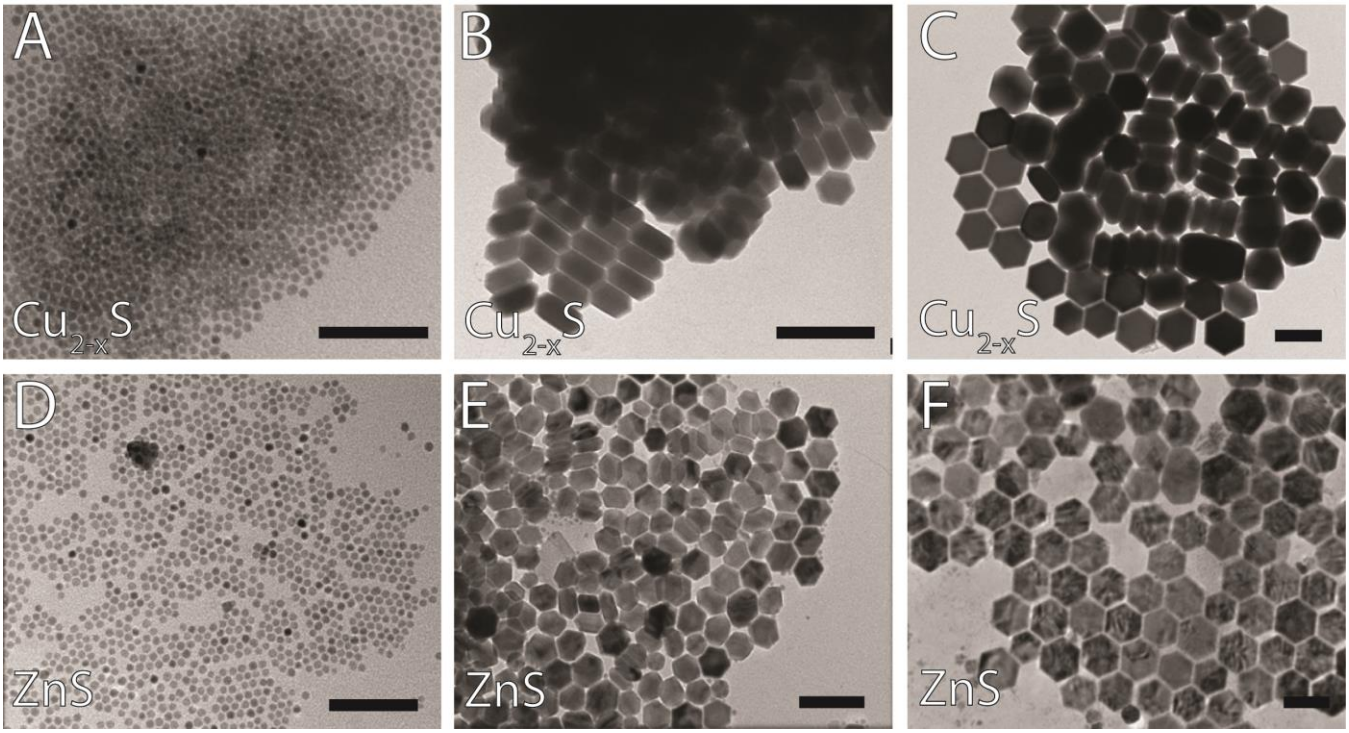


Figure A4.4: (A) Spherical NCs from the double injection and two (B and C) different sized $Cu_{2-x}S$ platelets and their ZnS equivalents (D)-(F) obtained via cation exchange. Scale bars correspond to 100 nm.

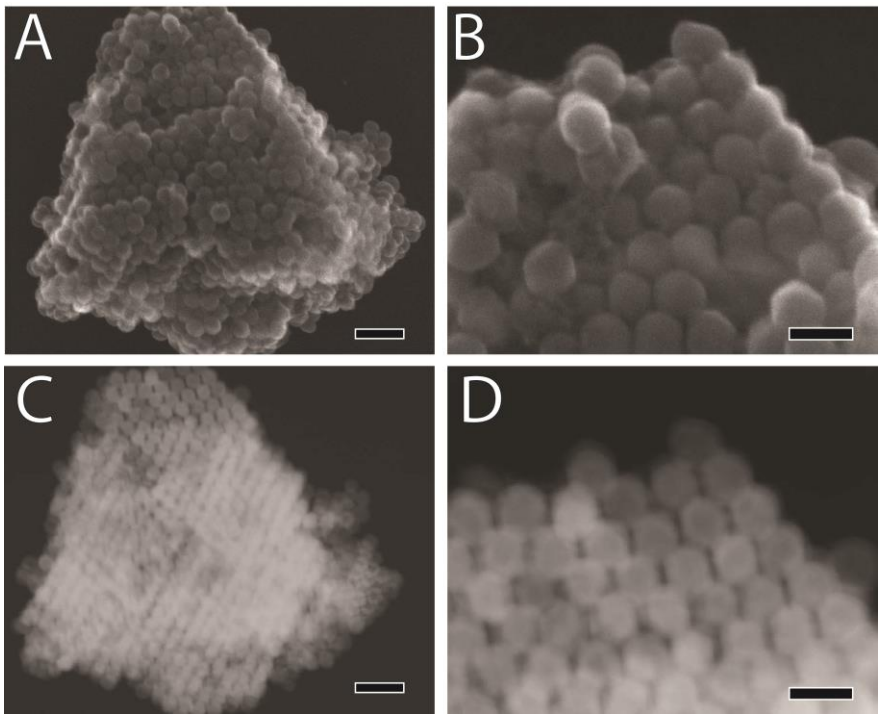


Figure A4.5: (A and B) SEM and STEM (C and D) images of obtained PbS 3D self-assembled superstructures.

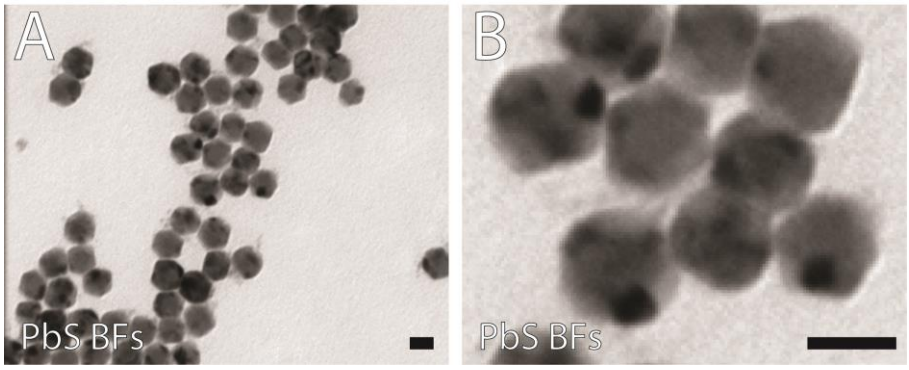


Figure A4.6: (A and B) TEM images of PbS BF obtained by cation exchange (A). . Scale bars correspond to 50 nm.

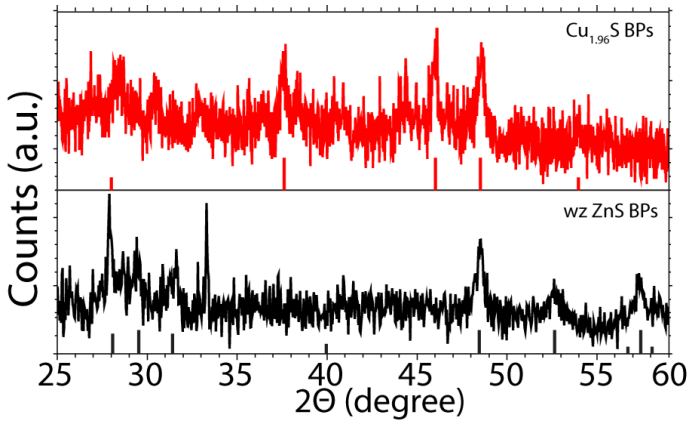


Figure A4.7: XRD measurements of the CE hexagonal. Reference bars are from JCPDS card no. [05-0492] and [20-0365] for wurtzite ZnS and djurleite $Cu_{1.96}S$ respectively.

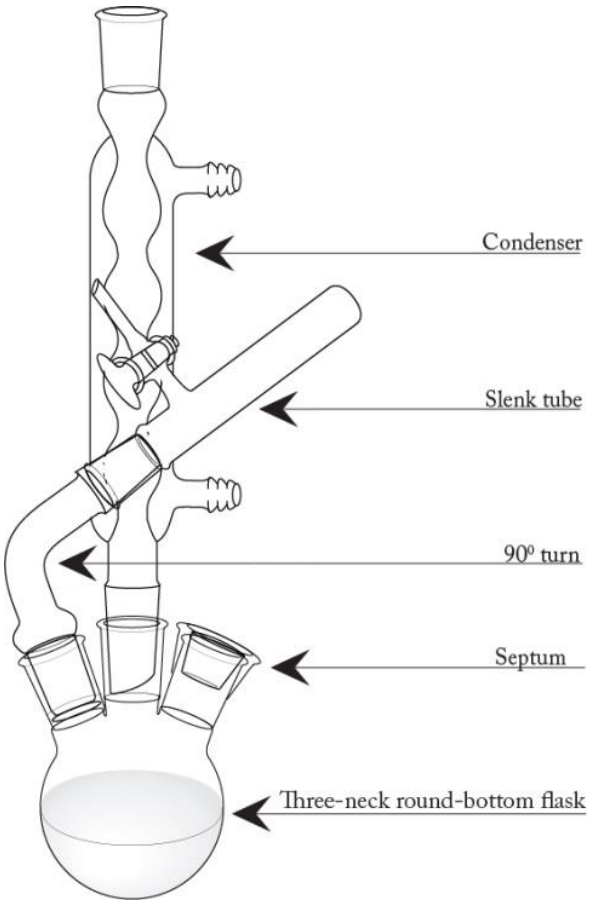


Figure A5.1: Set-up used for the synthesis of DDSe.

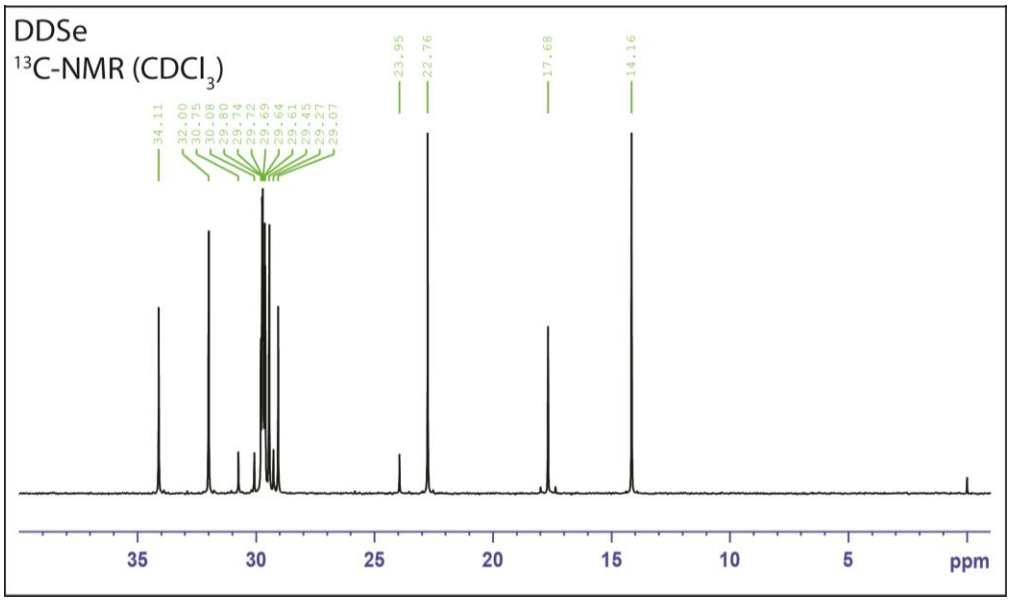


Figure A5.2: $^{13}$C-NMR spectrum of the synthesized DDSe.

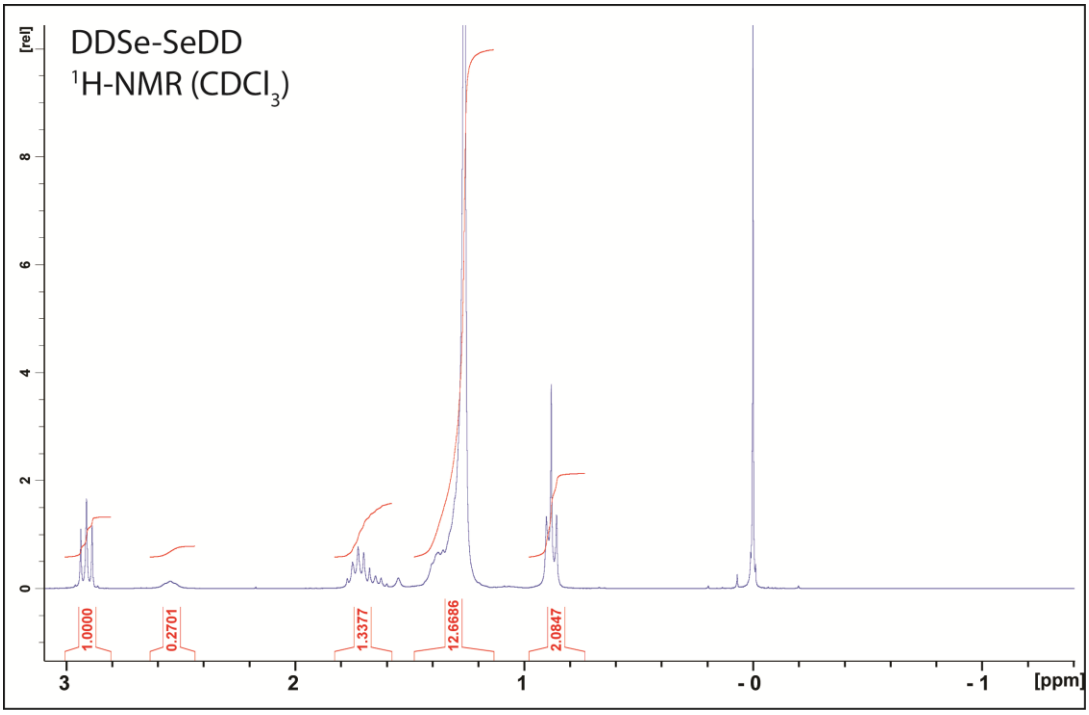


Figure A5.3: $^1$H-NMR spectrum of the synthesized DDSe-SeDD.

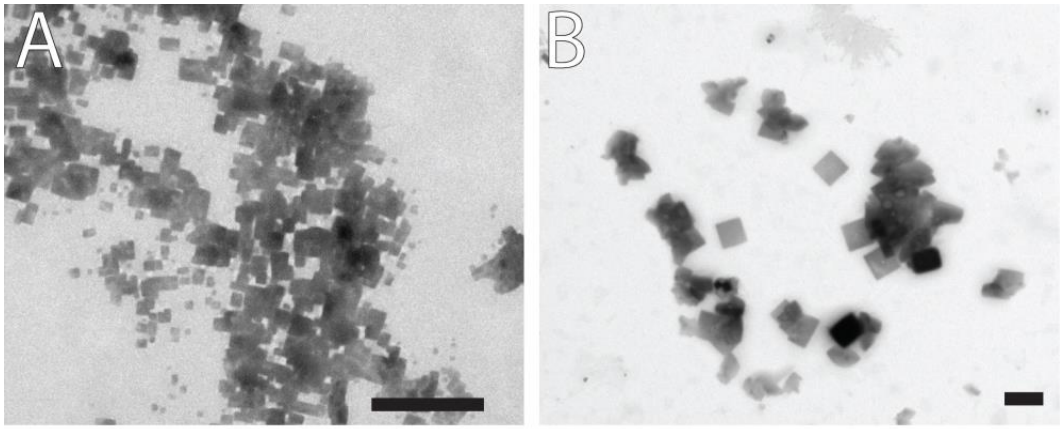


Figure A5.4: Two TEM image (A and B) of highly symmetric thin materials found 1 minute after the injection of DDSe. Scale bars correspond to 1 μm.

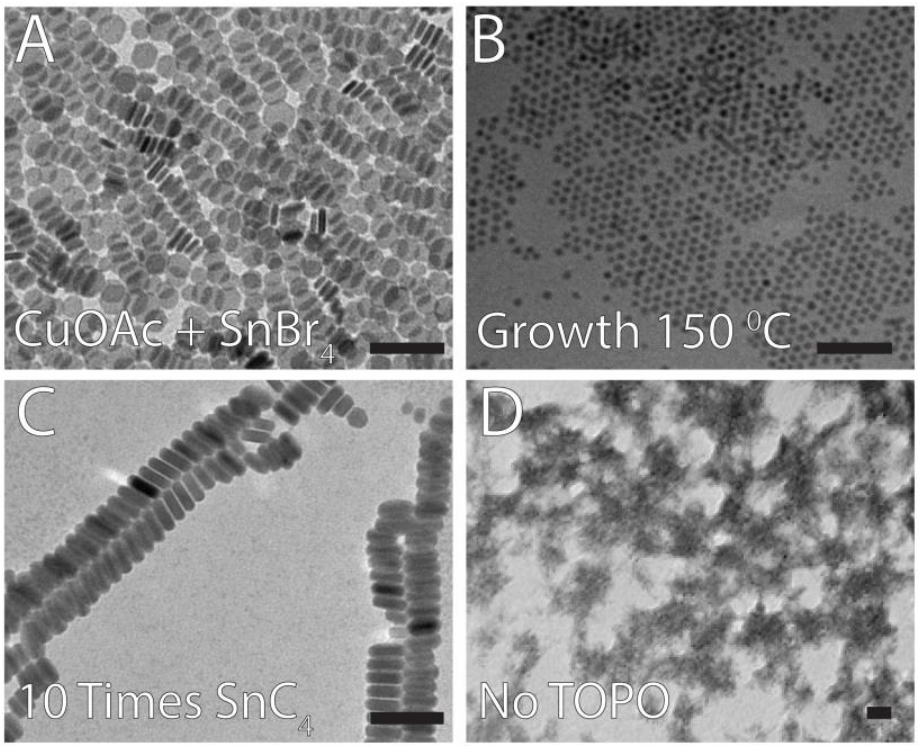


Figure A5.5: TEM images of different changes to the $Cu_{2-x}Se$ platelet synthesis with the aim of increasing the aspect ratio. (A) CuOAc and $SnBr_4$ instead of CuBr and NaBr, (B) lowering the growth temperature to 150 $^0$C instead of 170 $^0$C, (C) using 10 times the amount $SnCl_4$ instead of $SnBr_4$ and (D) removing the TOPO ligand. Scale bars correspond to 100 nm.

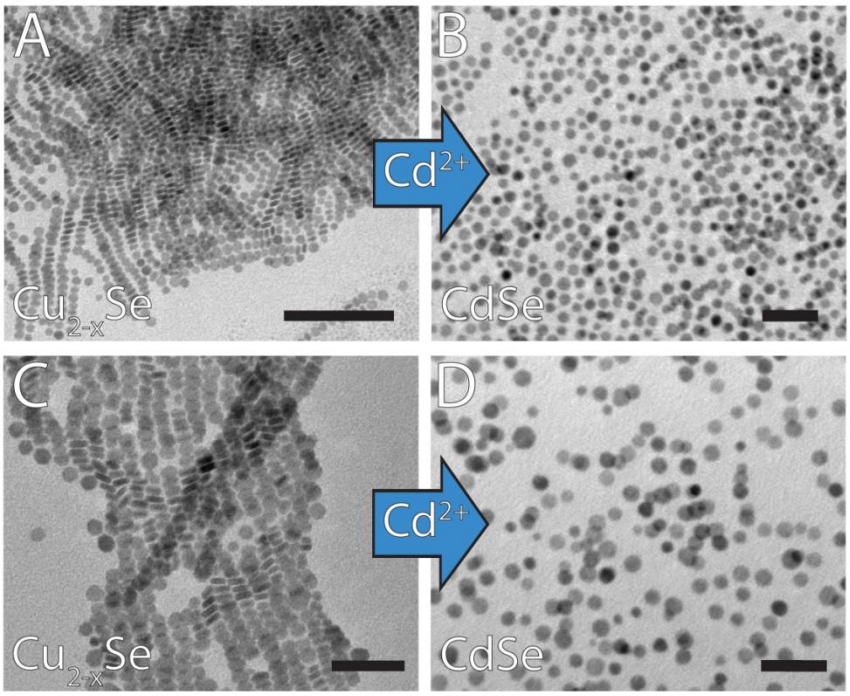


Figure A5.6: TEM images of the (A+C) $Cu_{2-x}Se$ platelets before and (B+D) CdSe platelets after the CE reaction of $Cu^+$ for $Cd^{2+}$. Furthermore, clustering is only observed for the $Cu_{2-x}Se$ platelets, whereas the CdSe platelets only lay flat on the substrate form monolayers. Scale bars correspond to 50 nm.

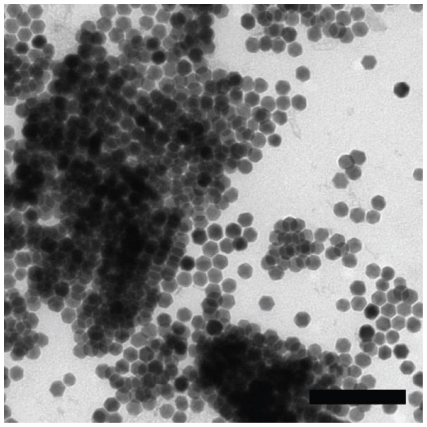

**Figure A6.1: Self-assembled superstructures obtained from hexagonal bifrustum-shaped $Cu_{1.96}S$ NCs, capped with alkylthiols. Scale bar corresponds to 200 nm. Reproduced with permission from ref [1]. Copyright (2014) American Chemical Society.***

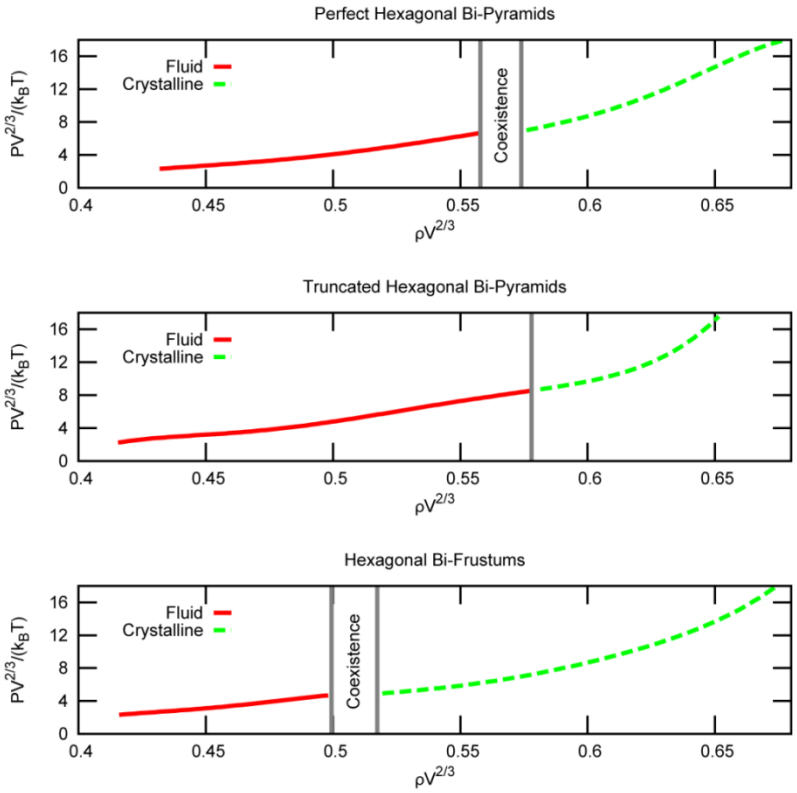


**Figure A6.2: Equation of States (EOS), reduced pressure $P^* = \beta P v^{2/3}$ versus number density $\rho^* = \rho v^{2/}$, obtained using floppy-box Monte Carlo (FBMC) simulations with $\beta = 1/k_BT$ as the inverse temperature. Perfect hexagonal bipyramids (BPs) undergo a first-order transition around $\rho^* = 0.56$ from a liquid phase to a hexagonal lattice, while truncated BPs show a weak first order transition around $\rho^* = 0.57$ from isotropic phase to tetragonal lattice. Bifrustums (BFs) form a hexagonal lattice after a first order transition from isotropic phase around $\rho^* = 0.51$. Reproduced with permission from ref [1]. Copyright (2014) American Chemical Society.***

* Copyright @ 2014 American Chemical Society.[1]

Ward van der Stam, Anjan P. Gantapara, Quinten A. Akkerman, Giuseppe Soligno, Johannes D. Meeldijk, René van Roij, Marjolein Dijkstra, and Celso de Mello Donega.

Self-Assembly of Colloidal Hexagonal Bipyramid- and Bifrustum-Shaped ZnS Nanocrystals into Two-Dimensional Superstructures.

*Nano Lett.*, **2014**, *14* (2), pp 1032–1037.